Improved Control of Superconducting Qubits with Static and Parametric Couplings

by

Tongyu Zhao

B.S., Nanjing University, 2018

A thesis submitted to the

Faculty of the Graduate School of the

University of Colorado in partial fulfillment

of the requirements for the degree of

Doctor of Philosophy

Department of Physics

2025

Committee Members:

Raymond W. Simmonds, Chair

Adam Kaufman

András Gyenis

Xun Gao

Cody Scarborough

Zhao, Tongyu (Ph.D., Physics)

Improved Control of Superconducting Qubits with Static and Parametric Couplings

Thesis directed by Dr. Raymond W. Simmonds

This thesis explores novel strategies for advancing superconducting quantum computing through a series of experimental investigations and device innovations. Grounded in the development of circuit quantum electrodynamics, the work addresses the challenges posed by the limitations of coherent control, coherence time and scaling of superconducting qubits. Focusing on transmon qubits, the thesis first reviews the foundational principles of circuit quantum electrodynamics and the critical role of the transmon in achieving robust qubit performance.

Three experimental studies form the core of this work. The first study demonstrates a universal quantum gate set for strongly coupled transmons. By exploiting the residual ZZ interaction, the work introduces a novel two-axis gate protocol for single-qubit operations and implements both CZ and CNOT gates with high fidelities, highlighting the potential for fast, low-error quantum operations in the strong coupling regime. The second study investigates a dual-rail qubit architecture using parametrically coupled transmons, showcasing a hardware-efficient approach to quantum error correction. This experiment converts single-photon loss errors into detectable erasures and leverages mid-circuit detection to enhance qubit coherence, thereby advancing fault-tolerant quantum computing schemes in the NISQ era. The final study focuses on the development of merged-element transmons (MET) and their FinMET variants. By integrating the Josephson junction and shunt capacitor into a single trilayer device, these innovations achieve a dramatic reduction in device footprint while addressing loss channels through advanced materials engineering, ultimately paving the way for scalable, high-coherence quantum circuits.

Collectively, these contributions demonstrate significant progress in quantum gate design, error mitigation, and qubit architecture, offering promising routes toward the realization of large-scale, fault-tolerant quantum computers.

Dedication

To my parents, Lin and Zhongshu, and all the good souls that I came across.

Acknowledgements

This dissertation marks the culmination of several years of work and growth, made possible by the unwavering support, mentorship, and encouragement of many individuals to whom I am deeply grateful.

First and foremost, I would like to express my heartfelt thanks to Dr. Raymond Simmonds for welcoming me into the Advanced Microwave Photonics group during a pivotal transition in my academic journey. His scientific insight, intuitive understanding, and constant support have profoundly shaped my development as a physicist. I am especially grateful for the many enlightening discussions and for his exemplary approach to doing science at the highest level.

I extend my sincere appreciation to Dr. David Pappas, who first introduced me to the field of circuit quantum electrodynamics and the Quantum Information Processing group. His mentorship during the formative stages of my graduate career provided me with the tools and confidence to evolve into an independent researcher.

I am thankful to Dr. John Teufel and Dr. Joe Aumentado, whose roles as co-PIs in the Advanced Microwave Photonics group provided both technical guidance and invaluable personal support. Their mentorship has been integral to the success of my research.

I am indebted to Dr. Junling Long, who played a crucial role during my transition into graduate research. As a senior student in Dr. Pappas' group, his patient, hands-on guidance in the lab laid the foundation for my future work. His consistent readiness to answer questions and offer direction greatly accelerated my learning process.

To my colleagues in the Quantum Information Processing group—Dustin Hite, Joel Howard, Sungoh Park, Mustafa Bal, Ruichen Zhao, Haozhi Wang, Jae Park, and Corey Rae McRae—thank you for the camaraderie, engaging discussions, and daily support throughout our time together.

I am also grateful to the senior scientists in the Advanced Microwave Photonics group—Katarina Cicak, Florent Lecocq, Maxime Malnou, Anthony McFadden, Bradley Hauer, and Xiaoyue Jin—for their instrumental help in setting up experimental systems, deepening my understanding of the physics involved, and assisting with device fabrication.

I would like to acknowledge Kaixuan Ji, Akash Dixit, Zachary Parrott, Jose Estrada Gonzalez, Trevyn Larson, Benton Miller, Sudhir Sahu, and Anastasia Simonova for the many collaborative discussions, teamwork, and support, which made our group both intellectually stimulating and personally enjoyable.

I am especially appreciative of the theoretical collaborators at NIST, including Shawn Geller, Alex Kwiatkowski, Scott Glancy, and Emanuel Knill, whose insights greatly enhanced my understanding of the experimental data and contributed to the interpretation of key results.

My thanks also go to Manuel Castellanos-Beltran and Adam Sirois, who generously allowed me to complete measurements using their dilution refrigerator and provided essential advice and support in maintaining and troubleshooting the measurement systems.

I am also grateful for the contributions of external collaborators, including Prof. Sophia Economou, Prof. Edwin Barnes, and Prof. Chris Palmstrøm, for their support in joint research projects that broadened the scope and impact of my work.

Finally, I wish to express my deepest gratitude to my parents, friends, and my partner Yueying Wang, for their constant love, encouragement, and support. Their belief in me sustained me through the many challenges of this journey.

To all of you, thank you.

Contents

Chapter

Tables

Table

Figures

Figure

Chapter 1

Introduction

Since the dawn of civilization, the pursuit of more efficient methods for counting, calculating, and processing information has driven technological progress. However, it was not until the mid-20th century that a true revolution occurred with the invention of the transistor in 1947 by John Bardeen, William Shockley, and Walter Brattain at Bell Laboratories [1]. This innovation, which enabled the creation of compact, reliable electronic switches, paved the way for the modern computer age. As transistors became smaller and more powerful, the number of transistors integrated on a single chip grew exponentially, following Moore's law [2], which predicted that the number of transistors on a chip would double approximately every 18 months.

For decades, this exponential growth fueled rapid improvements in computing power, enabling the development of everything from personal computers to global communications networks. However, the relentless miniaturization of transistors has faced fundamental physical limits [3]. As transistors shrink to the scale of individual atoms, quantum mechanical effects, such as tunneling and leakage currents, begin to dominate [4], making further progress increasingly difficult. Around 2006, Dennard scaling, which had previously allowed transistors to operate at lower voltages and higher speeds as they were reduced in size, also began to break down [5]. This marked the beginning of the end for the steady increases in clock speed and single-thread performance that had driven much of the computing revolution. The failure of Moore's law has prompted the search for new paradigms of computing [6], and it is here that quantum computing offers an exciting alternative, utilizing the principles of quantum mechanics to transcend the limitations of classical transistor-based devices [7].

At the dawn of the 20th century, many believed that the major questions of physics had been resolved [8]. Classical theories appeared to explain the workings of thermodynamics, electromagnetism, and mechanics with great precision, reflecting the technological triumphs of the industrial revolution. Yet, several experimental anomalies—such as the ultraviolet catastrophe—revealed gaps in the existing scientific framework [9]. These inconsistencies would ultimately lead to the birth of quantum mechanics. Introduced through Max Planck's idea of energy quantization [10, 11] and later expanded by Werner Heisenberg [12] and Erwin Schrödinger [13], quantum mechanics overturned the classical worldview, introducing concepts like superposition and entanglement, which defy common intuition [14].

Initially met with skepticism, quantum mechanics gradually gained acceptance through theoretical breakthroughs and experimental validation. For instance, John Bell's theorem [15] and the experimental work of Alain Aspect in the 1980s [16] provided irrefutable evidence of quantum non-locality, validating the strange but accurate predictions of quantum theory. This laid the groundwork for further exploration of quantum mechanics beyond fundamental physics, leading to the possibility of harnessing quantum phenomena for computation.

The idea of quantum computing was first proposed in 1982 by Richard Feynman, who recognized that simulating quantum systems on classical computers is computationally inefficient due to the sheer complexity of quantum interactions [17]. Peter Shor's development of a quantum algorithm for factoring large numbers in 1994 marked a significant milestone, as it demonstrated the potential of quantum computers to outperform classical ones in solving specific, computationally hard problems like integer factorization [18]. Shor's algorithm also raised alarms regarding the security of modern cryptography, which relies on the difficulty of factoring large numbers to secure data [19].

Over the past two decades, researchers have explored various physical platforms for quantum computing, each with its unique advantages and challenges [20]. Trapped ions represent one of the earliest successful quantum computing architectures [21], where individual ions are confined with electromagnetic fields and manipulated with lasers, offering long coherence times and high gate fidelity [22]. Photonic systems, in which quantum information is carried by photons, are attractive due to their natural resistance to decoherence [23], but they face difficulties in implementing two-qubit gates [24]. Spin-based qubits, such as those in quantum dots or nitrogen-vacancy centers in diamond [25], leverage the quantum properties of individual electrons, providing another promising approach with strong potential for integration [26]. The subject of this thesis, superconducting circuits, has seen rapid advancements in scalability and coherence, making them a leading candidate for large-scale quantum computing [27].

In particular, the development of the transmon qubit [28], a specific type of superconducting qubit, has been a critical milestone in the evolution of quantum computing. Traditional superconducting qubits, such as the Cooper-pair box, were prone to high sensitivity to charge noise, which limited their coherence times. The transmon, introduced by Robert Schoelkopf and Michel Devoret in 2007, solved this issue by reducing the qubit's sensitivity to charge fluctuations, significantly improving coherence times without sacrificing control over quantum operations [28]. This breakthrough has positioned superconducting circuits as one of the most viable platforms for quantum computing, leading to their widespread adoption in industry and academia alike [29].

However, the current landscape of quantum computing exists in what is known as the Noisy Intermediate-Scale Quantum (NISQ) era [30]. NISQ devices, which typically consist of tens to hundreds of qubits, operate in a regime where noise and errors are unavoidable but manageable for specific tasks [31]. Although these devices lack the ability to implement large-scale quantum error correction, they still hold considerable potential for solving problems that remain intractable for classical computers [32]. Researchers have begun developing NISQ algorithms, such as the Variational Quantum Eigensolver (VQE) [33] and Quantum Approximate Optimization Algorithm (QAOA) [34], which are designed to leverage the computational power of these noisy systems. While NISQ devices cannot yet achieve fault-tolerant computation, they represent an important transitional phase, bridging the gap between classical computing and fully developed quantum machines.

One of the major challenges in quantum computing is the issue of error correction. Unlike classical bits, quantum bits (qubits) are vulnerable to errors from environmental noise and inaccuracies in control [35]. These errors can accumulate over time, making long computations prone to failure. In 1995, Peter Shor introduced the first quantum error correction code [36], which allowed a logical qubit to be redundantly encoded using multiple physical qubits. This breakthrough paved the way for more sophisticated error-correcting codes [37], and today, error correction remains central to the pursuit of large-scale, reliable quantum computation [38].

Despite these challenges, rapid progress in quantum information science is undeniable. From Shor's algorithm to the development of quantum error correction and the growing capabilities of superconducting qubits, the field has made significant strides. However, much work remains before fully fault-tolerant, large-scale quantum computers can be realized [39].

1.1 Overview of thesis

This thesis reports recent experiment results aiming to either explore new strategies that can improve current superconducting devices or utilize these devices to explore hardware-efficient quantum error correction codes.

Chapter 2 gives a brief summary of circuit quantum electrodynamics (circuit-QED). Starting from a simple LC oscillator, the most basic component that can be found on a superconducting quantum processor, incrementally complex components are further introduced.

The technical details of experiment setups and device fabrication are discussed in chapter 3. The experiments involving superconducting devices in this thesis are performed with fabricated chips cooled down to $\sim 10\,\mathrm{mK}$ in a dilution refrigerator. To probe and control these devices, microwave pulses generated by delicate electronics at room temperature are routed through various stages of attenuation at different temperatures sequentially before reaching the device. These details should help readers to better understand the experiments described in this thesis.

In chapter 4, an experiment aiming to realize a universal gate set with two strongly coupled transmons is discussed. It is shown that with a finite amount of ZZ coupling between transmons, which is normally viewed as a challenge of realizing high-fidelity single-qubit gates, unconditional single-qubit gate can still be realized via pulse-shape engineering. Combined with numerically shaped two-qubit gates, we can prepare the two-qubit system into any desired state. Detailed characterizations of the gates are also discussed.

Chapter 5 introduces an experiment that investigates encoding a dual-rail logical qubit with two parametrically coupled transmons to explore hardware-efficient quantum error correction schemes. We also demonstrated the possibility of further improving the logical qubit coherence times by utilizing mid-circuit detection.

Three experiments are covered in chapter 6 where effort towards realizing the merged-element transmon is introduced. By integrating the Josephson junction and shunt capacitor into a single tri-layer device, the merged-element transmon scheme has the potential of benefiting next-generation quantum processors by both dramatically reducing the qubit footprint and improving qubit coherence times.

The last chapter 7 sums up the dissertation with a summary of our research results and possible improvements.

Chapter 2

Circuit Quantum Electrodynamics

The advent of circuit quantum electrodynamics (circuit-QED) represents a major milestone in the field of quantum information science, as it enables the realization of strong interactions between quantum bits (qubits) and electromagnetic modes within superconducting circuits [40, 41]. Drawing from the principles of cavity quantum electrodynamics (cavity-QED), where atoms interact with photons confined in cavities [42], circuit-QED adapts this framework to the solid-state realm. This shift to superconducting circuits provides a highly scalable and versatile platform for building quantum processors [39].

A key element of circuit-QED is the transmon qubit, a type of superconducting qubit that has become the standard in many quantum computing architectures [28]. The transmon is derived from the Cooper pair box [43, 44], a charge qubit, but with design modifications that significantly reduce its sensitivity to charge noise, one of the primary sources of decoherence. This is achieved by increasing the ratio of the Josephson energy to the charging energy, thus making the energy levels less dependent on small fluctuations in charge. As a result, the transmon qubit exhibits greater coherence times compared to earlier charge qubits, making it a robust candidate for scalable quantum computing [45].

The transmon operates by confining quantum information in the quantized energy levels of a non-linear resonant circuit, typically consisting of a Josephson junction shunted by a large capacitance. Its anharmonic energy level structure ensures that the lowest two levels (representing the $|0\rangle$ and $|1\rangle$ states) can be isolated for quantum operations. This anharmonicity is essential for avoiding unwanted transitions to higher energy levels during qubit manipulations.

In the context of circuit-QED, transmon qubits are coupled to microwave cavities, which can serve different roles: they can be utilized to store quantum information [46, 47, 48], measure adjacent qubit non-destructively [49, 50], filter the electromagnetic environment seen by the qubit [51, 52], or mediate interactions between qubits [53, 54]. The combination of qubits and cavities, governed by the principles of quantum mechanics and circuit theory, creates a powerful platform for exploring fundamental quantum phenomena and advancing quantum computation [55].

This chapter starts from the one of the basic building blocks of circuit-QED, a simple LC oscillator, followed by several discussions, incrementally moving towards more complex systems. Through these topics, we aim to build a solid foundation for understanding how circuit-QED contributes to modern quantum technology.

2.1 The Quantum LC Oscillator

2.1.1 Simple LC Oscillator

A capacitor (C) and an inductor (L) form an LC oscillator when connected in parallel or in series. In one such system, energy oscillates between electrical energy stored in the C and magnetic energy stored in L as shown in Fig. (2.1).

Energy stored in a capacitor or an inductor can be derived from the instantaneous voltage $V(t)$ and current $I(t)$ in each individual element,

$$E(t) = \int_{-\infty}^{t} V(t')I(t')\,\mathrm{d}t'. \tag{2.1.1}$$

Combine Eq. (2.1.1) with the current-voltage relation of a capacitor $I = C\,\mathrm{d}V/\mathrm{d}t$ or an inductor $V = L\,\mathrm{d}I/\mathrm{d}t$, we can derive

$$U_C = \frac{1}{2}CV^2 \tag{2.1.2}$$

$$U_L = \frac{1}{2}LI^2. \tag{2.1.3}$$

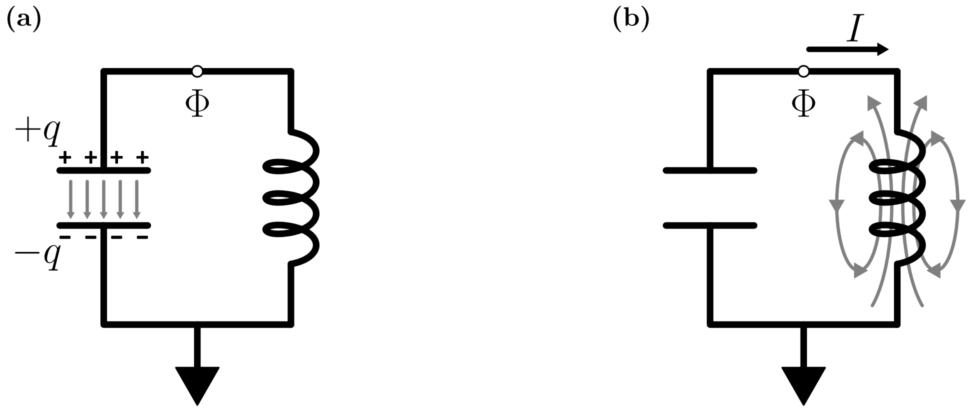

Figure 2.1: Circuit diagram of a simple lumped-element parallel LC oscillator. (a) and (b) show two different mechanisms for energy storage during an oscillation period. Sign of the capacitor charge q and direction of the current I are chosen to be consistent with the Hamilton's equations of motion Eq. (2.1.13) and Eq. (2.1.14).

It is convenient when analyzing Josephson junctions, which are effectively nonlinear inductors, to modify Eq. (2.1.2) and Eq. (2.1.3) in terms of the node flux Φ [56, 57] defined as

$$\Phi(t) = \int_{-\infty}^{t} V(t')\,\mathrm{d}t', \tag{2.1.4}$$

where $V(t)$ is the node voltage at the point shown in Fig. (2.1). Since $V(t) = \dot{\Phi}(t)$,

$$U_C = \frac{1}{2}C\dot{\Phi}^2. \tag{2.1.5}$$

Examine the inductor current-voltage relation, we can derive

$$\begin{aligned} I &= \int_{-\infty}^{t} \frac{V(t')}{L}\,\mathrm{d}t' \\ &= \frac{\Phi}{L}. \end{aligned} \tag{2.1.6}$$

Then

$$U_L = \frac{1}{2L}\Phi^2. \tag{2.1.7}$$

The energy oscillation of LC oscillators can then be described by the Lagrangian,

$$\mathcal{L} = \frac{1}{2}C\dot{\Phi}^2 - \frac{1}{2L}\Phi^2. \tag{2.1.8}$$

In an analog to a harmonic oscillator formed by attaching a mass m to a spring with constant k described by the Lagrangian $\mathcal{L} = m\dot{x}^2/2 - kx^2/2$, the electrical energy resembles the "kinetic energy" term, while the magnetic energy resembling the "potential energy" term. From the Euler-Lagrange equation of motion

$$\frac{\partial \mathcal{L}}{\partial \Phi} - \frac{\mathrm{d}}{\mathrm{d}t}\frac{\partial \mathcal{L}}{\partial \dot{\Phi}} = -\frac{\Phi}{L} - C\ddot{\Phi} = 0 \tag{2.1.9}$$

we can see that the natural frequency ω_r of one such LC oscillator is given by

$$\omega_r = \frac{1}{\sqrt{LC}}. \tag{2.1.10}$$

The conjugate momentum can be derived by

$$\frac{\partial \mathcal{L}}{\partial \dot{\Phi}} = C\dot{\Phi} = CV = q, \tag{2.1.11}$$

which turns out to be the charge q. The Hamiltonian can then be derived as

$$\mathcal{H} = q\dot{\Phi} - \mathcal{L} = \frac{1}{2C}q^2 + \frac{1}{2L}\Phi^2. \tag{2.1.12}$$

The Hamilton's equations of motion can be written

$$-\dot{q} = \frac{\partial \mathcal{H}}{\partial \Phi} = \frac{\Phi}{L} = I \tag{2.1.13}$$

$$\dot{\Phi} = \frac{\partial \mathcal{H}}{\partial q} = \frac{q}{C} = V \tag{2.1.14}$$

The fact that Eq. (2.1.13) agrees with the law of conservation of charge and Eq. (2.1.14) agrees with previous definition Eq. (2.1.4) serves as a sanity check to ensure that above analysis of the system is physically intact.

Similar to the treatment of a spring-mass mechanical oscillator, we can promote the charge q and node flux Φ to quantum operators which obey the canonical commutation relation

$$[\hat{\Phi}, \hat{q}] = i\hbar. \tag{2.1.15}$$

To better describe the superconducting systems under consideration, we define the reduced flux $\hat{\phi} \equiv 2\pi\hat{\Phi}/\Phi_0$ with $\Phi_0 = h/(2e)$ being the superconducting magnetic flux quantum and charge number $\hat{n} \equiv \hat{q}/(2e)$. Now the Hamiltonian can be rewritten as

$$\begin{aligned}\hat{\mathcal{H}} &= \frac{2e^2}{C}\hat{n}^2 + \frac{1}{2L}\left(\frac{\Phi_0}{2\pi}\right)^2\hat{\phi}^2 \\ &\equiv 4E_C\hat{n}^2 + \frac{1}{2}E_L\hat{\phi}^2,\end{aligned} \tag{2.1.16}$$

where $E_C \equiv e^2/(2C)$ is the charging energy required to add one electron [58] to the capacitor and $E_L \equiv \Phi_0^2/(4\pi^2 L)$ is the inductive energy. $\hat{\phi}$ and $\hat{n}$ now obey the canonical commutation relation

$$[\hat{\phi}, \hat{n}] = i. \tag{2.1.17}$$

We can write Eq. (2.1.16) in a second quantization form by defining a creation operator $\hat{a}$ and an annihilation operator $\hat{a}^\dagger$ as

$$\hat{a} = +i\left(\frac{2E_C}{E_L}\right)^{\frac{1}{4}}\hat{n} + \left(\frac{E_L}{32E_C}\right)^{\frac{1}{4}}\hat{\phi} \tag{2.1.18}$$

$$\hat{a}^\dagger = -i\left(\frac{2E_C}{E_L}\right)^{\frac{1}{4}}\hat{n} + \left(\frac{E_L}{32E_C}\right)^{\frac{1}{4}}\hat{\phi}, \tag{2.1.19}$$

such that

$$[\hat{a}, \hat{a}^\dagger] = 1 \tag{2.1.20}$$

and

$$\hat{\phi} = \phi_{\text{zpf}} \times (\hat{a}^\dagger + \hat{a}) \tag{2.1.21}$$

$$\hat{n} = n_{\text{zpf}} \times i(\hat{a}^\dagger - \hat{a}), \tag{2.1.22}$$

where $\phi_{\text{zpf}} \equiv (2E_C/E_L)^{1/4}$ and $n_{\text{zpf}} \equiv (E_L/32E_C)^{1/4}$ are magnitudes of zero-point fluctuations of the reduced phase and the charge number respectively. By substituting $\hat{\phi}$ and $\hat{n}$ in Eq. (2.1.16), we can get

$$\hat{\mathcal{H}} = \hbar\omega_r\left(\hat{a}^\dagger\hat{a} + \frac{1}{2}\right), \tag{2.1.23}$$

where $\omega_r = \sqrt{8E_L E_C}/\hbar = 1/\sqrt{LC}$.

The eigenstates of Eq. (2.1.23) can be labeled as $|k\rangle$ with $k = 0, 1, 2, \cdots$, also known as Fock states. The eigenenergies $E_k = \hbar\omega_r(k + 1/2)$ form an equally spaced infinite set of levels as shown

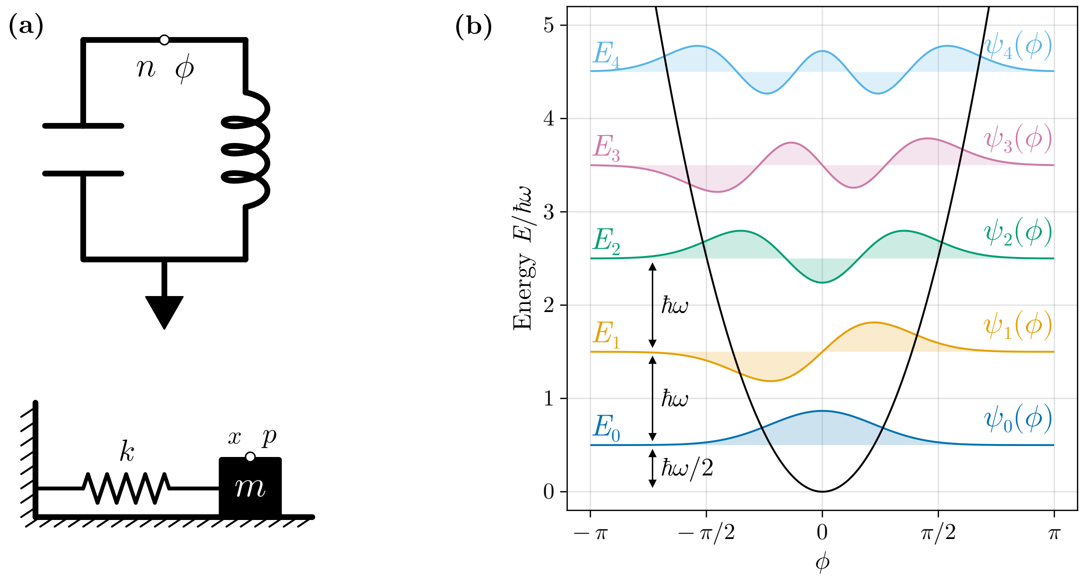

Figure 2.2: (a) An analogy we can draw between the LC oscillator and a spring-mass mechanical oscillator. (b) Energies of the first five eigenstates of a quantum harmonic oscillator. The wavefunctions $\psi_k(\phi)$ illustrate how the distributions are confined by the quadratic potential well $V(\phi) = E_L\phi^2/2$.

in Fig. (2.2(b)). The wavefunction of state $|k\rangle$ in the flux basis is

$$\psi_k(\phi) = \frac{1}{\sqrt{2^k k!}}\left(\frac{1}{2\pi\phi_{\text{zpf}}^2}\right)^{\frac{1}{4}} e^{-\frac{\phi^2}{4\phi_{\text{zpf}}^2}} H_k\left(\frac{\phi}{\sqrt{2}\phi_{\text{zpf}}}\right), \tag{2.1.24}$$

where H_k are the physicist's Hermite polynomials,

$$H_k(x) = (-1)^k e^{x^2}\frac{\mathrm{d}^k}{\mathrm{d}x^k}e^{-x^2}. \tag{2.1.25}$$

When the harmonic oscillator is at its lowest-energy state $|0\rangle$, we can calculate the variance of $\hat{\phi}$ and $\hat{n}$ via

$$\langle 0|\,\hat{\phi}^2\,|0\rangle = \phi_{\text{zpf}}^2\,\langle 0|\,(\hat{a}^\dagger + \hat{a})^2\,|0\rangle = \phi_{\text{zpf}}^2 \tag{2.1.26}$$

$$\langle 0|\,\hat{n}^2\,|0\rangle = -n_{\text{zpf}}^2\,\langle 0|\,(\hat{a}^\dagger - \hat{a})^2\,|0\rangle = n_{\text{zpf}}^2. \tag{2.1.27}$$

These non-zero fluctuations enable the harmonic oscillators to interact with other degrees of freedom even at their ground state and mark a major difference between a quantum harmonic oscillator and its classical counterpart.

Properties of lumped-element LC oscillators found in circuit-QED experiments can vary depending on the specific application and goal. An example set of properties $L \sim 5\,\mathrm{nH}$ and $C \sim 200\,\mathrm{fF}$ is reported in Ref. [59], which yields $\omega_r/2\pi \sim 5\,\mathrm{GHz}$. We can link the vacuum fluctuation of voltage ΔV to n_{zpf} through $\Delta V = 2e/C \cdot \Delta n = 2e/C \cdot \sqrt{\langle \hat{n}^2 \rangle - \langle \hat{n} \rangle^2} = 2e/C \cdot n_{\mathrm{zpf}} = \sqrt{\hbar\omega_r/(2C)} \sim 3\,\mu\mathrm{V}$. When the harmonic oscillator is at a finite temperature T, there will be thermal fluctuation added to the zero-point fluctuation. To ensure that the quantum behavior won't be cloaked by the thermal effects, we require that $k_B T \ll \hbar\omega_r$. A harmonic oscillator with $\omega_r/2\pi \sim 5\,\mathrm{GHz}$ requires $T \ll 240\,\mathrm{mK}$, which calls for use of dilution refrigerators that can stably cool macroscopic devices to $\sim 10\,\mathrm{mK}$.

The ground state $|0\rangle$ is also a special case of the so-called coherent states. A coherent state $|\alpha\rangle$ is a specific quantum state of the harmonic oscillator that most closely resembles classical behavior [42, 60], and can be written as the superposition of Fock states

$$|\alpha\rangle = e^{-\frac{|\alpha|^2}{2}} \sum_{n=0}^{\infty} \frac{\alpha^n}{\sqrt{n!}} |n\rangle \,. \tag{2.1.28}$$

We'll see in the next part that $|\alpha\rangle$ is a state that is created when a harmonic oscillator at its ground state is subject to a classical drive.

2.1.2 Driven Harmonic Oscillator

Since $\langle k| \hat{\mathcal{H}} |l\rangle = 0$ when $k \neq l$, when the harmonic oscillator is left on its own, transitions between different Fock states are prohibited. Time evolution of a harmonic oscillator is described by the Schrödinger's equation, in which case the Fock states are stationary. We can add more dynamics to the system by introducing a time-dependent classical current source $I_d(t)$ to the ϕ node as shown in Fig. (2.3). Kirchhoff's current law dictates that

$$\dot{q} + I - I_d(t) = 0. \tag{2.1.29}$$

We can model the system by adding a driving term $V(q, \Phi)$ to Eq. (2.1.12),

$$\mathcal{H}_{\mathrm{driven}} = \frac{1}{2C} q^2 + \frac{1}{2L} \Phi^2 + V(q, \Phi). \tag{2.1.30}$$

Compare the Hamilton's equation of motion $-\dot{q} = \partial\mathcal{H}_{\text{driven}}/\partial\Phi = \Phi/L + \partial V(q,\Phi)/\partial\Phi$ with Eq. (2.1.29), we can find that $V(q,\Phi) = -I_d(t)\Phi$ and therefore

$$\mathcal{H}_{\text{driven}} = \frac{1}{2C}q^2 + \frac{1}{2L}\Phi^2 - I_d(t)\Phi. \tag{2.1.31}$$

Then the second quantization Hamiltonian is found to be

$$\hat{\mathcal{H}}_{\text{driven}} = \hbar\omega_r\left(\hat{a}^\dagger\hat{a} + \frac{1}{2}\right) - \hbar\varepsilon(t)(\hat{a}^\dagger + \hat{a}), \tag{2.1.32}$$

where $\varepsilon(t) \equiv I_d(t)\cdot\phi_{\text{zpf}}/(2e)$.

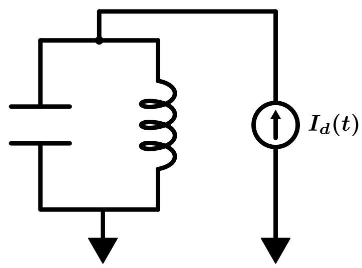

Figure 2.3: An LC oscillator driven by a classical current source $I_d(t)$

It is often desirable to separate the effect of the driving term from the harmonic oscillator's own oscillation. This can be achieved by switching to the interaction picture [61] and transforming the Hamiltonian with the unitary operator $U(t) = \exp(i\omega_r t\hat{a}^\dagger\hat{a})$ such that

$$\begin{aligned}\hat{\mathcal{H}}^{\text{I}}_{\text{driven}} &= U\hat{\mathcal{H}}_{\text{driven}}U^\dagger + i\hbar\dot{U}U^\dagger \\ &= -\hbar\varepsilon(t)(e^{i\omega_r t}\hat{a}^\dagger + e^{-i\omega_r t}\hat{a}).\end{aligned} \tag{2.1.33}$$

As pointed out in Ref. [61], time evolution over time t with Eq. (2.1.33) brings a harmonic oscillator prepared in a coherent state $|\alpha(0)\rangle$ to $|\alpha(t)\rangle$ such that

$$\alpha(t) = \alpha(0) + i\int_0^t \varepsilon(t')e^{i\omega_r t'}\,\mathrm{d}t' \tag{2.1.34}$$

If we consider the case where the initial state is the vacuum state $|0\rangle$, then the time evolution can be modeled with a unitary operator $\hat{D}(\alpha)$ where

$$\begin{aligned}|\alpha\rangle &= e^{\alpha a^\dagger - \alpha^* a}|0\rangle \\ &\equiv \hat{D}(\alpha)|0\rangle,\end{aligned} \tag{2.1.35}$$

with $\alpha \equiv i \int_0^t \varepsilon(t')e^{i\omega_r t'}\,\mathrm{d}t'$. $\hat{D}(\alpha)$ is named the displacement operator that reflects the effect of a classical drive on a coherent state.

2.1.3 Coupled Harmonic Oscillators

The above analysis shows how we can treat an isolated lumped-element LC oscillator as a quantum harmonic oscillator. In real circuit-QED devices, however, these oscillators are often embedded in complex environments, interacting with other circuit components. We'll first examine a simple case where two LC oscillators are coupled through a capacitor C_c as shown in Fig. (2.4).

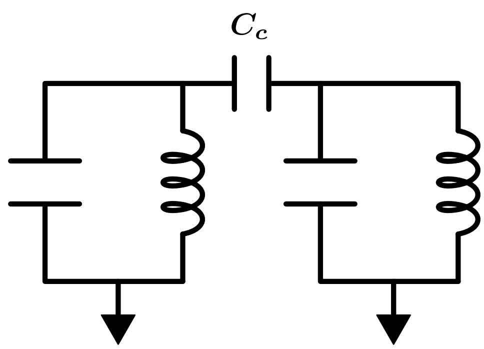

Figure 2.4: Two LC oscillators coupled through a capacitor C_c.

By adding the energy of C_c to the oscillators' Lagrangian, we can find the system Lagrangian to be

$$\mathcal{L}_{\text{coupled}} = \sum_{i=1,2}\left(\frac{1}{2}C_i\dot{\Phi}_i^2 - \frac{1}{2L_i}\Phi_i^2\right) + \frac{1}{2}C_c\big(\dot{\Phi}_1 - \dot{\Phi}_2\big)^2. \tag{2.1.36}$$

It is a common practice to write Eq. (2.1.36) in a matrix form

$$\mathcal{L}_{\text{coupled}} = \frac{1}{2}\dot{\boldsymbol{\Phi}}^\intercal \boldsymbol{C}\dot{\boldsymbol{\Phi}} - \frac{1}{2}\boldsymbol{\Phi}^\intercal \boldsymbol{L}^{-1}\boldsymbol{\Phi}, \tag{2.1.37}$$

where

$$\boldsymbol{\Phi} = \begin{pmatrix}\Phi_1\\ \Phi_2\end{pmatrix}, \tag{2.1.38}$$

$$\boldsymbol{C} = \begin{pmatrix}C_1 + C_c & -C_c\\ -C_c & C_2 + C_c\end{pmatrix}, \tag{2.1.39}$$

$$\boldsymbol{L} = \begin{pmatrix}L_1 & 0\\ 0 & L_2\end{pmatrix}. \tag{2.1.40}$$

The charge $\boldsymbol{q}$ is now

$$\boldsymbol{q} = \boldsymbol{C}\dot{\boldsymbol{\Phi}}. \tag{2.1.41}$$

Then we can derive the Hamiltonian of the system

$$\begin{aligned}\mathcal{H}_{\text{coupled}} &= \boldsymbol{q}^{\intercal}\dot{\boldsymbol{\Phi}} - \mathcal{L}_{\text{coupled}} \\ &= \frac{1}{2}\boldsymbol{q}^{\intercal}\boldsymbol{C}^{-1}\boldsymbol{q} + \frac{1}{2}\boldsymbol{\Phi}^{\intercal}\boldsymbol{L}^{-1}\boldsymbol{\Phi}.\end{aligned} \tag{2.1.42}$$

Define $\omega_i \equiv \sqrt{(\boldsymbol{C}^{-1})_{ii}/L_{ii}}$ and $\beta \equiv C_c/\sqrt{(C_1 + C_c)(C_2 + C_c)}$, we can derive the second quantization Hamiltonian following the procedure of Eqs. (2.1.12)–(2.1.23),

$$\hat{\mathcal{H}}_{\text{coupled}} = \sum_{i=1,2} \hbar\omega_i\left(\hat{a}_i^{\dagger}\hat{a}_i + \frac{1}{2}\right) - \frac{1}{2}\hbar\beta\sqrt{\omega_1\omega_2}(\hat{a}_1^{\dagger} - \hat{a}_1)(\hat{a}_2^{\dagger} - \hat{a}_2), \tag{2.1.43}$$

with the ladder operators $\hat{a}_i$ and $\hat{a}_i^{\dagger}$ now obeying the canonical commutation relation

$$[\hat{a}_i, \hat{a}_j^{\dagger}] = \delta_{ij}. \tag{2.1.44}$$

We can see from Eq. (2.1.43) that the system reduces to two individual harmonic oscillators with an additional term that governs the interaction between them. The Hamiltonian can be further diagonalized using Bogoliubov transformation [62] which could turn into a tedious process. Here we will instead seek to simplify Eq. (2.1.43) with rotating-wave approximation (RWA).

A unitary transformation $U = \exp[-i(\omega_1\hat{a}_1^{\dagger}\hat{a}_1 + \omega_2\hat{a}_2^{\dagger}\hat{a}_2)t]$ brings the Hamiltonian into the interaction picture as

$$\begin{aligned}\hat{\mathcal{H}}_{\text{coupled}}^{\text{I}} &= -\frac{1}{2}\hbar\beta\sqrt{\omega_1\omega_2}(\hat{a}_1^{\dagger}e^{-i\omega_1 t} - \hat{a}_1 e^{i\omega_1 t})(\hat{a}_2^{\dagger}e^{-i\omega_2 t} - \hat{a}_2 e^{i\omega_2 t}) \\ &= -\frac{1}{2}\hbar\beta\sqrt{\omega_1\omega_2}\big[\hat{a}_1^{\dagger}\hat{a}_2^{\dagger}e^{-i(\omega_1+\omega_2)t} - \hat{a}_1^{\dagger}\hat{a}_2 e^{-i(\omega_1-\omega_2)t} + \text{h.c.}\big].\end{aligned} \tag{2.1.45}$$

Applying RWA, terms oscillating at frequency $\omega_1 + \omega_2$ can be neglected when $|\omega_1 - \omega_2| \ll \omega_1 + \omega_2$. Then

$$\hat{\mathcal{H}}_{\text{coupled}}^{\text{I, RWA}} = \frac{1}{2}\hbar\beta\sqrt{\omega_1\omega_2}\big[\hat{a}_1^{\dagger}\hat{a}_2 e^{-i(\omega_1-\omega_2)t} + \hat{a}_1\hat{a}_2^{\dagger}e^{i(\omega_1-\omega_2)t}\big]. \tag{2.1.46}$$

Transform back into the Schrödinger picture,

$$\hat{\mathcal{H}}_{\text{coupled}} \approx \sum_{i=1,2} \hbar\omega_i\left(\hat{a}_i^{\dagger}\hat{a}_i + \frac{1}{2}\right) + \frac{1}{2}\hbar\beta\sqrt{\omega_1\omega_2}(\hat{a}_1^{\dagger}\hat{a}_2 + \hat{a}_1\hat{a}_2^{\dagger}). \tag{2.1.47}$$

The interaction term in Eq. (2.1.47) is often called transverse coupling since it only populates the off-diagonal elements in the Hamiltonian matrix.

2.2 Transmission Line

Discussion in the previous sections involves mainly lumped-element circuits where it is assumed that the dimension d of any circuit element is far smaller than the wavelength λ of the electromagnetic wave under study. This requirement is not always achievable in the microwave regime where we may have to deal with λ in the millimeter range while $d \sim 100\,\mu\mathrm{m}$ [63]. Thus distributed circuits such as transmission lines are frequently employed in circuit-QED devices. We will now investigate both finite-length and semi-infinite transmission lines.

2.2.1 Transmission Line Resonator

A finite-length transmission line can be formed with a coaxial cable or a segment of coplanar waveguide (CPW) on a dielectric substrate, e.g. sapphire or silicon. A loss-less transmission line of total length d can be modeled by a series of lumped-element LC segments of unit length Δx as shown in Fig. (2.5(c)). The terminations on both ends ($x = 0$ and $x = d$) can be either open or short. By assuming all segments have the same unit capacitance C_0 and inductance L_0, we can treat the transmission line as many coupled harmonic oscillators and write its Lagrangian $\mathcal{L}_{\mathrm{TL}}$ in terms of flux $\Phi_0, \Phi_1, \cdots, \Phi_{n-1}$ at each node,

$$\mathcal{L}_{\mathrm{TL}} = \sum_{n=0}^{N-1} \left[\frac{1}{2} C_0 \dot{\Phi}_n^2 - \frac{1}{2L_0} (\Phi_{n+1} - \Phi_n)^2 \right], \tag{2.2.1}$$

where $N = d/\Delta x$. The charge q_n at each node is then given by

$$q_n = \frac{\partial \mathcal{L}_{\mathrm{TL}}}{\partial \dot{\Phi}_n} = C_0 \dot{\Phi}_n. \tag{2.2.2}$$

Therefore the Hamiltonian of the transmission line is

$$\mathcal{H}_{\mathrm{TL}} = \sum_{n=0}^{N-1} q_n \dot{\Phi}_n - \mathcal{L}_{\mathrm{TL}} = \sum_{n=0}^{N-1} \left[\frac{1}{2C_0} q_n^2 + \frac{1}{2L_0} (\Phi_{n+1} - \Phi_n)^2 \right], \tag{2.2.3}$$

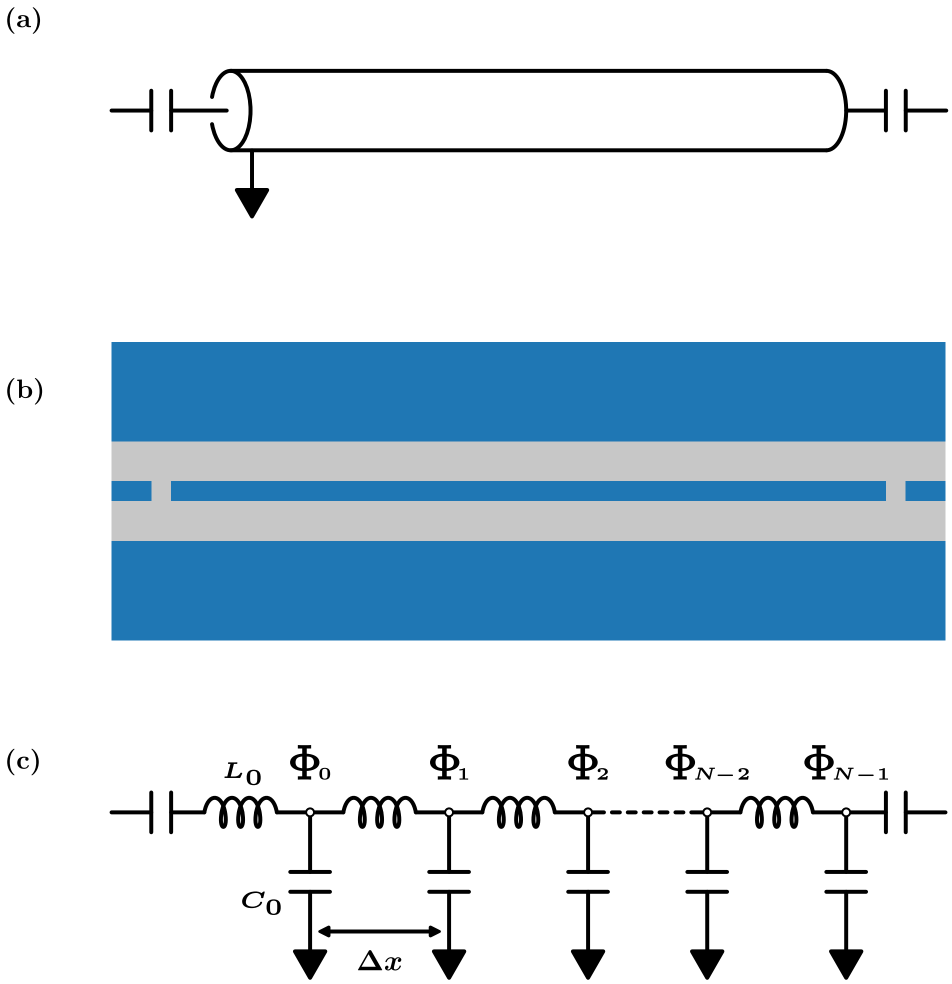

Figure 2.5: Schematics of the transmission line model. (a) A coaxial cable is an example of transmission line. It consists of a metal center trace surrounded by ground plane with insulation in between. (b) The top view of a CPW resonator. It's formed by depositing metal (blue) on a dielectric substrate (gray). The top and bottom are ground planes. The gaps in the center trace are coupling capacitors. (c) Both coaxial cable and CPW can be modeled with a transmission line model where the distributed system is broken down into a series of lumped-element LC segments.

In the limit of $\Delta x \to 0$, we can treat q_n and Φ_n as continuous fields $q(x,t)$ and $\Phi(x,t)$ dependent on both $x \in [0,d]$ and $t \in [-\infty, +\infty]$ such that $q(n\Delta x, t) = q_n/\Delta x$ and $\lim_{\Delta x \to 0}(\Phi_{n+1} - \Phi_n) = \mathrm{d}x \cdot \partial\Phi(x,t)/\partial x$. Then Eq. (2.2.3) can be rewritten as

$$\mathcal{H}_{\mathrm{TL}} = \int_0^d \mathrm{d}x \left[\frac{1}{2c_0} q^2 + \frac{1}{2l_0}\left(\frac{\partial \Phi}{\partial x}\right)^2\right], \tag{2.2.4}$$

where $c_0 \equiv C_0/\,\mathrm{d}x$ and $l_0 \equiv L_0/\,\mathrm{d}x$ are capacitance and inductance per unit length respectively. The Hamilton's equations of motions are

$$-\frac{\partial q}{\partial t} = \frac{\delta \mathcal{H}_{\mathrm{TL}}}{\delta \Phi} = -\frac{1}{l_0}\frac{\partial^2 \Phi}{\partial x^2} \tag{2.2.5}$$

$$\frac{\partial \Phi}{\partial t} = \frac{\delta \mathcal{H}_{\mathrm{TL}}}{\delta q} = -\frac{1}{c_0} q. \tag{2.2.6}$$

From Eq. (2.2.5) and Eq. (2.2.6) we can derive the wave equation for $\Phi(x,t)$

$$v_{\mathrm{p}}^2 \frac{\partial^2 \Phi}{\partial x^2} - \frac{\partial^2 \Phi}{\partial t^2} = 0, \tag{2.2.7}$$

with $v_{\mathrm{p}} = 1/\sqrt{l_0 c_0}$ being the phase velocity of the transmission line.

The solution to Eq. (2.2.7) can be decomposed into normal modes each oscillating at a frequency ω_m

$$\Phi(x,t) = \sum_{m=0}^{\infty} \phi_m(x) X_m(t), \tag{2.2.8}$$

with $\ddot{X}_m = -\omega_m^2 X_m$. Then for each mode $\phi_m(x)$ can be decided by solving the boundary-value problem

$$\frac{\mathrm{d}^2}{\mathrm{d}x^2}\phi_m(x) + k_m^2 \phi_m(x) = 0, \tag{2.2.9}$$

where the wave vector $k_m = \omega_m / v_{\mathrm{p}}$. The general solution to Eq. (2.2.9) is

$$\phi_m(x) = A_m \cos(k_m x + \varphi_m). \tag{2.2.10}$$

For the circuit shown in Fig. (2.5(c)), the transmission line is terminated with opens at both ends and form a half-wave resonator, which requires the derivative of $\phi_m(x)$ to vanish at $x = 0$ and $x = d$. In this case $\varphi_m = 0$ and $k_m d$ must be integer multiple of π. This condition constraints all possible ω_m to form an infinite set of discrete values such that

$$\omega_m = (m+1)\frac{\pi v_{\mathrm{p}}}{d}. \tag{2.2.11}$$

The zero-frequency term has been dropped since it corresponds to a trivial mode where flux along the whole transmission line uniformly offsets from zero. The standing-wave modes $\phi_m(x)$'s form an orthogonal basis when

$$\frac{1}{d}\int_0^d \phi_m(x)\phi_{m'}(x)\,\mathrm{d}x = \delta_{mm'}, \tag{2.2.12}$$

which yields $A_m = \sqrt{2}$. Then we can substitute

$$\Phi(x,t) = \sum_{m=0}^{\infty} \sqrt{2} X_m(t) \cos(k_m x) \tag{2.2.13}$$

$$q(x,t) = c_0 \dot{\Phi} = \sum_{m=0}^{\infty} c_0 \sqrt{2} \dot{X}_m(t) \cos(k_m x) \tag{2.2.14}$$

back into Eq. (2.2.4) with the orthogonal property Eq. (2.2.12) to get

$$\mathcal{H}_{\mathrm{TL}} = \sum_{m=0}^{\infty} \left(\frac{1}{2C} P_m^2 + \frac{1}{2} C \omega_m^2 X_m^2 \right), \tag{2.2.15}$$

where $C = c_0 d$ is the total capacitance of the half-wave transmission line resonator and $P_m = C\dot{X}_m$. The Hamiltonian Eq. (2.2.15) appears to be a sum of familiar harmonic oscillator Hamiltonian at different frequencies. We can then follow the second quantization procedure again to get

$$\hat{\mathcal{H}}_{\mathrm{TL}} = \sum_{m=0}^{\infty} \hbar \omega_m \hat{b}_m^\dagger \hat{b}_m, \tag{2.2.16}$$

where $\hat{a}_m$ and $\hat{a}_m^\dagger$ are ladder operators of mode m defined as

$$\hat{b}_m = \sqrt{\frac{C\omega_m}{2\hbar}} \left(\hat{X}_m + \frac{i}{C\omega_m} \hat{P}_m \right) \tag{2.2.17}$$

$$\hat{b}_m^\dagger = \sqrt{\frac{C\omega_m}{2\hbar}} \left(\hat{X}_m - \frac{i}{C\omega_m} \hat{P}_m \right). \tag{2.2.18}$$

Eq. (2.2.16) shows the transmission line resonator can be modeled as an infinite series of independent harmonic oscillators. The mode with the lowest frequency $\omega_0/(2\pi) = v_{\mathrm{p}}/(2d) = 1/(2d\sqrt{l_0 c_0})$ is often called the fundamental mode. The other modes are called higher harmonics with mode frequencies being integer multiples of the fundamental frequency.

2.2.2 Semi-infinite Transmission Line

In the limit of $d \to +\infty$, the half-wave resonator transitions to a semi-infinite transmission line. With the mode separation $\Delta\omega/(2\pi) = v_{\mathrm{p}}/(2d) \to 0$, the discrete mode frequencies ω_m turn into a continuous spectrum and give rise to the Hamiltonian

$$\hat{\mathcal{H}}_{\mathrm{si\text{-}TL}} = \int_0^{\infty} \hbar\omega \hat{b}^\dagger(\omega) \hat{b}(\omega)\, \mathrm{d}\omega, \tag{2.2.19}$$

with $[\hat{b}(\omega), \hat{b}^\dagger(\omega')] = \delta(\omega - \omega')$. Eq. (2.2.19) suggests that a semi-infinite transmission line can be viewed as a heat bath with flat spectrum [64].

In circuit-QED applications, semi-infinite transmission lines often serve as feedlines delivering microwave drives to resonators or qubits. Here we will study a scenario where an LC oscillator is capacitively coupled to a semi-infinite transmission line. The added coupling allows for driving the oscillator with external forces while opening dissipate channels at the same time. The goal is to follow the input-output formalism [64, 65] and derive the quantum Langevin equation [66] which describes the scattering process involving the oscillator.

The system Hamiltonian can be written as a sum of three terms

$$\hat{\mathcal{H}}_{\text{LC–TL}} = \hat{\mathcal{H}}_{\text{LC}} + \hat{\mathcal{H}}_{\text{si–TL}} + \hat{\mathcal{H}}_{\text{int}}. \tag{2.2.20}$$

$\hat{\mathcal{H}}_{\text{int}}$ accounts for the interaction between the harmonic oscillator and the heat bath and takes the form of

$$\hat{\mathcal{H}}_{\text{int}} = i\hbar \int_{-\infty}^{\infty} \mathrm{d}\omega \gamma(\omega)[\hat{b}^\dagger(\omega)\hat{a} - \hat{b}(\omega)\hat{a}^\dagger]. \tag{2.2.21}$$

Then the Heisenberg equation of motion for $\hat{b}(\omega)$ is

$$\begin{aligned}\dot{\hat{b}}(\omega) &= \frac{i}{\hbar}[\hat{\mathcal{H}}_{\text{LC–TL}}, \hat{b}(\omega)] \\ &= -i\omega\hat{b}(\omega) + \gamma(\omega)\hat{a}.\end{aligned} \tag{2.2.22}$$

We can solve Eq. (2.2.22) for $\hat{b}(\omega)$ such that

$$\hat{b}(\omega) = e^{-i\omega(t-t_0)}\hat{b}_0(\omega) + \gamma(\omega)\int_{t_0}^{t} e^{-i\omega(t-t')}\hat{a}(t')\,\mathrm{d}t'. \tag{2.2.23}$$

Then the quantum Langevin equation can be derived by substituting Eq. (2.2.23) into the Heisenberg equation of motion for $\hat{a}$,

$$\begin{aligned}\dot{\hat{a}} &= \frac{i}{\hbar}[\hat{\mathcal{H}}_{\text{LC–TL}}, \hat{a}] \\ &= -i\omega_r\hat{a} - \int_{-\infty}^{\infty} \mathrm{d}\omega\gamma(\omega)e^{-i\omega(t-t_0)}\hat{b}_0(\omega) - \int_{-\infty}^{\infty} \mathrm{d}\omega\gamma^2(\omega)\int_{t_0}^{t} e^{-i\omega(t-t')}\hat{a}(t')\,\mathrm{d}t'.\end{aligned} \tag{2.2.24}$$

To simplify Eq. (2.2.24), we can assume that the coupling strength γ is independent of frequency and define $\gamma(\omega) = \sqrt{\kappa/(2\pi)}$. An input field $\hat{b}_{\mathrm{in}}(t)$ can be defined as

$$\hat{b}_{\mathrm{in}}(t) = \frac{1}{\sqrt{2\pi}} \int_{-\infty}^{\infty} \mathrm{d}\omega e^{-i\omega(t-t_0)} \hat{b}_0(\omega), \tag{2.2.25}$$

with $\hat{b}_0(\omega)$ being the value of $\hat{b}(\omega)$ at $t = t_0$. Also notice two useful properties

$$\int_{-\infty}^{\infty} \mathrm{d}\omega e^{-i\omega(t-t')} = 2\pi\delta(t-t') \tag{2.2.26}$$

$$\int_{t_0}^{t} c(t')\delta(t-t')\,\mathrm{d}t' = \frac{1}{2}c(t). \tag{2.2.27}$$

Now we can rewrite Eq. (2.2.24) as

$$\dot{\hat{a}} = -i\omega_r \hat{a} - \frac{\kappa}{2}\hat{a} - \sqrt{\kappa}\hat{b}_{\mathrm{in}}(t). \tag{2.2.28}$$

Eq. (2.2.28) describes how the harmonic oscillator evolves in time when placed in an open quantum environment. The first term on the RHS is the coherent oscillation at natural frequency ω_r. The second term corresponds to damping of the oscillator when energy leaks out into the semi-infinite transmission line at a rate κ. Even though all elements in the system are non-dissipative, energy propagating along the semi-infinite line never comes back and therefore resembles loss. The third term captures the effect from the environment (the transmission line). $\hat{b}_{\mathrm{in}}(t)$ could represent the vacuum state, a coherent drive, thermal field, or some other quantum state entering the harmonic oscillator.

We can also reverse time and solve Eq. (2.2.22) from t to a future time t_1 and get

$$\hat{b}(\omega) = e^{i\omega(t_1-t)}\hat{b}_1(\omega) - \sqrt{\frac{\kappa}{2\pi}} \int_{t}^{t_1} e^{i\omega(t'-t)}\hat{a}(t')\,\mathrm{d}t'. \tag{2.2.29}$$

An output field $\hat{b}_{\mathrm{out}}(t)$ is defined as

$$\hat{b}_{\mathrm{out}}(t) = \frac{1}{\sqrt{2\pi}} \int_{-\infty}^{\infty} \mathrm{d}\omega e^{i\omega(t_1-t)} \hat{b}_1(\omega). \tag{2.2.30}$$

Then if we substitute Eq. (2.2.30) instead of Eq. (2.2.25) into Eq. (2.2.24)

$$\dot{\hat{a}} = -i\omega_r \hat{a} + \frac{\kappa}{2}\hat{a} - \sqrt{\kappa}\hat{b}_{\mathrm{out}}(t). \tag{2.2.31}$$

Compare Eq. (2.2.31) to Eq. (2.2.28) we get

$$\hat{b}_{\mathrm{out}}(t) = \hat{b}_{\mathrm{in}}(t) + \sqrt{\kappa}\hat{a}(t). \tag{2.2.32}$$

This equation highlights how the oscillator modifies the outgoing field relative to the incoming field, enabling reflection/transmission measurements, single-photon detection, etc [64].

We can solve Eq. (2.2.28) by Fourier transforming the equation [57] in the convention of $\hat{a}(\omega) = \int_{-\infty}^{\infty} \exp(i\omega t)\hat{a}(t)\,\mathrm{d}t$ such that

$$-i\omega\hat{a}(\omega) = -i\omega_r\hat{a}(\omega) - \frac{\kappa}{2}\hat{a}(\omega) - \sqrt{\kappa}\hat{b}_{\mathrm{in}}(\omega), \tag{2.2.33}$$

which yields

$$\hat{a}(\omega) = -\frac{i\sqrt{\kappa}}{\omega - \omega_r + \frac{i\kappa}{2}}\hat{b}_{\mathrm{in}}(\omega). \tag{2.2.34}$$

Use Eq. (2.2.32), we can draw connection between $\hat{b}_{\mathrm{in}}(\omega)$ and $\hat{b}_{\mathrm{out}}(\omega)$,

$$\hat{b}_{\mathrm{out}}(\omega) = \frac{\omega - \omega_r - \frac{i\kappa}{2}}{\omega - \omega_r + \frac{i\kappa}{2}}\hat{b}_{\mathrm{in}}(\omega). \tag{2.2.35}$$

This equation demonstrates that the output field will have the same magnitude as the input field. The harmonic oscillator acts like a perfect mirror in this sense. When the input field is on-resonant with the harmonic oscillator($\omega \approx \omega_r$), the output field gains a π phase shift relative to the input field. If the field is far detuned ($|\omega - \omega_r| \gg \kappa$), the phase shift will instead approach zero. This frequency-dependent response allows us to spectroscopically probe the harmonic oscillator through the transmission line and is fundamental to many circuit-QED measurements.

Real-world resonators often come with internal loss due to various mechanisms, e.g. dielectric loss. We can model the loss by including an extra damping term $\kappa_{\mathrm{int}}/2 \cdot \hat{a}$ to the RHS of Eq. (2.2.28). Then we can derive the scattering coefficient $S(\omega) = \hat{b}_{\mathrm{out}}(\omega)/\hat{b}_{\mathrm{in}}(\omega)$ as,

$$S(\omega) = \frac{\omega - \omega_r - i\frac{\kappa - \kappa_{\mathrm{int}}}{2}}{\omega - \omega_r + i\frac{\kappa + \kappa_{\mathrm{int}}}{2}}. \tag{2.2.36}$$

We can also express Eq. (2.2.36) in terms of quality factors which are unit-less and defined as $Q_{\mathrm{int}} \equiv \omega_r/\kappa_{\mathrm{int}}$, $Q_{\mathrm{ext}} \equiv \omega_r/\kappa$ and $Q_{\mathrm{tot}}^{-1} = Q_{\mathrm{int}}^{-1} + Q_{\mathrm{ext}}^{-1}$ such that

$$S(\omega) = 1 - \frac{2Q_{\mathrm{tot}}}{Q_{\mathrm{ext}} - 2iQ_{\mathrm{ext}}Q_{\mathrm{tot}}\frac{\omega - \omega_r}{\omega_r}}. \tag{2.2.37}$$

The reflected power ratio is found to be

$$|S(\omega)|^2 = 1 - \frac{\frac{4}{Q_{\text{ext}}Q_{\text{int}}}}{\frac{1}{Q_{\text{tot}}^2} - 4\left(\frac{\omega-\omega_r}{\omega_r}\right)^2}, \tag{2.2.38}$$

which is a Lorentzian. Different relative relationships between Q_{int} and Q_{ext} can lead to different characteristics in the resonator response as shown in Fig. (2.6). In experiments, making S-parameter measurements on a resonator not only gives us information about ω_r but also allows us to gain information about Q_{int} and Q_{ext}, which is essential to understanding the loss mechanisms and improving the devices.

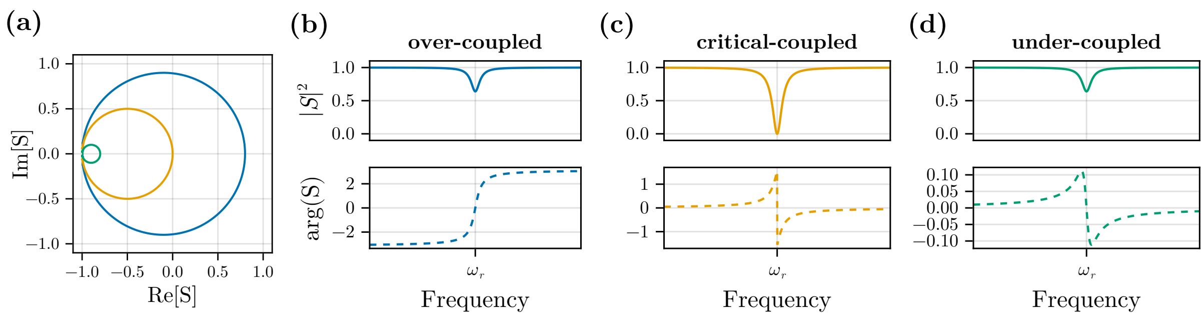

Figure 2.6: S-parameter of a resonator. (a) The real and imaginary part of $S(\omega)$ when sweeping ω across ω_r. The blue, orange and green circles correspond to over-coupled ($Q_{\text{int}} \gg Q_{\text{ext}}$), critical-coupled ($Q_{\text{int}} \approx Q_{\text{ext}}$) and under-coupeld ($Q_{\text{int}} \ll Q_{\text{ext}}$) cases respectively. (b)(c)(d) Magnitude and phase response when the resonator is at different coupling regimes.

For superconducting resonators commonly found in circuit-QED experiments, κ_{int} is affected by multiple factors such as dielectric losses [67, 68], surface and interface losses [69, 70] as well as material and fabrication treatment [71, 72, 73, 59]. In general, it is desirable to pursue more coherent resonators through improving the listed factors. κ_{ext} is mostly determined by device geometry design. Large κ_{ext} is preferred for faster information extraction from the resonator while small κ_{ext} favors the lifetime of information stored within the resonator.

2.3 Superconductivity and Josephson Effect

In previous section, we start from a classical circuit description of the LC oscillator and jump into the quantum world by promoting charge and flux variables to quantum operators. Modeling the system with just two non-commuting operators may seem to be oversimplification considering that even micro-fabricated circuits may contain millions of atoms and electrons. As it turns out, in ordinary superconductors, this simplification is justified due to the emergence of macroscopic quantum coherence. Superconductivity effectively gaps out single-particle excitations, and the long-range Coulomb force suppresses plasmon excitations at GHz range [57]. As a result, the relevant quantum degrees of freedom in a superconducting circuit are limited to those describing the collective motion of the electron fluid.

Even though being a significant element, the LC oscillator is quite limited in quantum information processing applications due to the equidistant spacing between energy levels, which renders selective control over quantum transitions impossible [56]. The inclusion of a nonlinear element–the Josephson junction–could introduce anharmonicity into the system and lift this degeneracy.

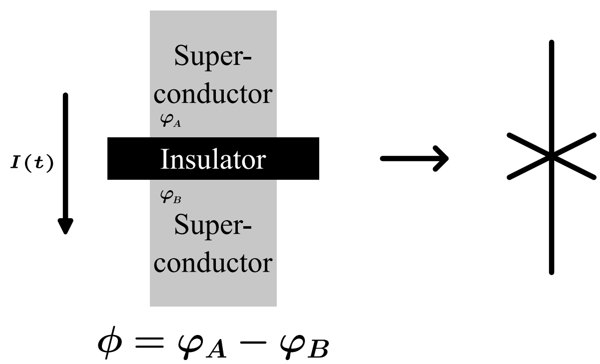

Figure 2.7: A schematic of the superconductor-insulator-superconductor type Josephson junction. The order parameter ϕ is defined as the phase difference $\varphi_A - \varphi_B$ of the two superconductors. In circuit diagrams a Josephson junction is often represented by a cross symbol shown on the right.

A Josephson junction can be formed by placing two superconductors in proximity with some barrier or restriction in between [74]. A common type of Josephson junction is a superconductor-insulator-superconductor structure as shown in Fig. (2.7). The Josephson junction can be described by the Josephson relations [75]:

$$I(t) = I_c \sin[\phi(t)] \tag{2.3.1}$$

$$V(t) = \frac{\hbar}{2e}\frac{\mathrm{d}\phi}{\mathrm{d}t}, \tag{2.3.2}$$

where $I(t)$ and $V(t)$ are the current through and the voltage across the Josephson junction, ϕ is the phase difference of Ginzburg—Landau order parameters across the junction, and critical current I_c is a characteristic of the junction.

We can view the Josephson junction as a nonlinear inductor, then

$$\frac{\mathrm{d}I}{\mathrm{d}t} = \frac{\mathrm{d}I}{\mathrm{d}\phi}\cdot\frac{\mathrm{d}\phi}{\mathrm{d}t} = I_c\cos\phi\cdot\frac{2e}{\hbar}V(t). \tag{2.3.3}$$

Recall that for a regular inductor $V = L\dot{I}$, we can find the Josephson junction inductance to be

$$L = \frac{\hbar}{2eI_c\cos\phi} = \frac{\Phi_0}{2\pi I_c\cos\phi} = \frac{L_J}{\cos\phi}, \tag{2.3.4}$$

where $L_J \equiv \Phi_0/(2\pi I_c)$ is named the Josephson inductance.

The energy stored in the Josephson junction can be calculated with

$$E(t) = \int_{-\infty}^{t} I(t')V(t')\,\mathrm{d}t' = -\frac{I_c\Phi_0}{2\pi}\cos\phi = -E_J\cos\phi, \tag{2.3.5}$$

where $E_J \equiv I_c\Phi_0/(2\pi)$ is named the Josephson energy. A trivial constant E_J is often added to $E(t)$ such that $E(t) = E_J(1-\cos\phi)$.

Now we can go back to the LC oscillator model, replace the inductor with a Josephson junction as shown in Fig. (2.8) and modify Eq. (2.1.16) such that

$$\hat{\mathcal{H}} = 4E_C\hat{n}^2 + E_J(1-\cos\hat{\phi}). \tag{2.3.6}$$

Taylor expand Eq. (2.3.6) around $\hat{\phi} = 0$,

$$\begin{aligned}\hat{\mathcal{H}} &= 4E_C\hat{n}^2 + E_J\left(\frac{\hat{\phi}^2}{2!} - \frac{\hat{\phi}^4}{4!} + \cdots\right)\\ &= 4E_C\hat{n}^2 + E_J\left(\frac{\hat{\phi}^2}{2!} - \frac{\hat{\phi}^4}{4!}\right).\end{aligned} \tag{2.3.7}$$

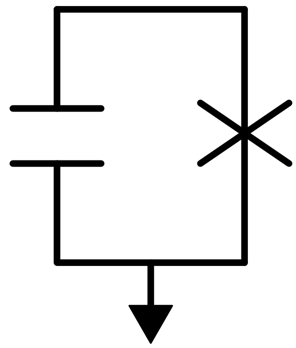

Figure 2.8: A non-linear harmonic oscillator can be formed by replacing the inductor in a harmonic oscillator with a Josephson junction.

We can then proceed with the same definitions for create and annihilation operators in the simple harmonic oscillator case and get

$$\begin{aligned}\hat{\mathcal{H}} &= \sqrt{8E_J E_C}\left(\hat{a}^\dagger\hat{a} + \frac{1}{2}\right) - \frac{E_C}{12}(\hat{a}^\dagger + \hat{a})^4 \\ &= \hbar\omega_q\left(\hat{a}^\dagger\hat{a} + \frac{1}{2}\right) - \frac{E_C}{2}\hat{a}^\dagger\hat{a}(\hat{a}^\dagger\hat{a} - 1) + \begin{pmatrix}\text{non-diagonal}\\ \text{terms}\end{pmatrix}.\end{aligned} \tag{2.3.8}$$

The first term of Eq. (2.3.8) comes out as the familiar quantum harmonic oscillator Hamiltonian with $\omega_q = (\sqrt{8E_J E_C} - E_C)/\hbar$. The second term originates from the non-linear nature of the Josephson junction and can be viewed as an energy shift added to ω_q that depends on the energy level. The anharmonicity α is defined as [28]

$$\alpha = \frac{E_{12} - E_{01}}{\hbar}, \tag{2.3.9}$$

with E_{ij} being the energy difference between the ith and the jth level. We can easily find that $\alpha = -E_C/\hbar$ in this case. In experiments, when we want to address the transition $|0\rangle \leftrightarrow |1\rangle$ with a microwave tone on-resonant with $E_{01}/\hbar$, the tone will be detuned from driving $|1\rangle \leftrightarrow |2\rangle$ by $E_C/\hbar$. This enables us to selectively address individual transitions and approximately treat one particular transition out of the infinite ladder as a qubit.

Built upon the non-linearity property of Josephson junctions, different species of superconducting qubit have been developed over the past several decades including charge qubit, flux qubit, phase qubit and quasicharge qubit [76]. These species differ mostly in choice and arrangement of capacitor, inductor and Josephson junction aiming to explore different regime of the parameter space spanned by the relative strengths of capacitive charging energy E_C, the inductive energy E_L and the Josephson energy E_J [29]. Among these species, the transmon [28], derived from the Cooper-pair box [77, 44, 43], stands out as a charge-insensitive charge qubit.

2.4 Transmon

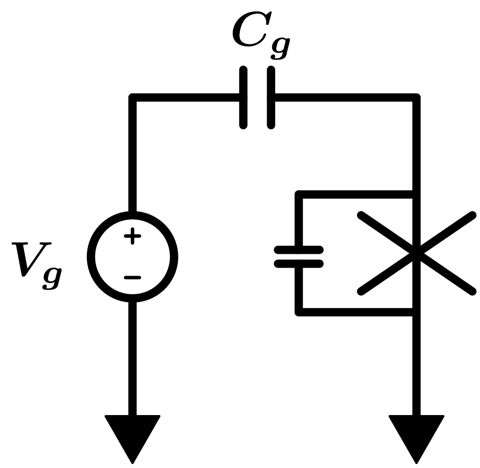

Figure 2.9: The circuit schematic of a Cooper-pair box (CPB).

We'll start the discussion about transmon with its predecessor, the Cooper-pair box as shown in Fig. (2.9) which is a charge qubit and can be modeled by adding a gate voltage V_g to the circuit in Fig. (2.8). The gate capacitance C_g allows for transferring Cooper pairs between the superconducting island and the reservoir. To include the effect of V_g and C_g, we have to modify Eq. (2.1.16) as

$$\hat{\mathcal{H}}_{\mathrm{CPB}} = 4E_C(\hat{n} - n_g)^2 + E_J(1 - \cos\hat{\phi}), \tag{2.4.1}$$

where the offset charge $n_g = C_g V_g/(2e)$ and $E_C = e^2/2(C + C_g)$.

To find the eigenstates and eigenenergies of the system, we need to solve the Schrödinger's equation for Eq. (2.4.1) in the phase basis,

$$\left[4E_C\left(-i\frac{\mathrm{d}}{\mathrm{d}\phi}-n_g\right)^2+E_J(1-\cos\phi)\right]\Psi(\phi)=E\Psi(\phi). \tag{2.4.2}$$

It is possible to solve Eq. (2.4.2) analytically by noticing that the equation differs from a Mathieu's equation by a transformation [28]. Then wavefunctions of the eigenstates can be expressed in terms of the Mathieu functions. The periodic boundary condition $\Psi(\phi+2\pi)=\Psi(\phi)$ also leads to eigenenergies which can be expressed in terms of the characteristic numbers of the Mathieu equation.

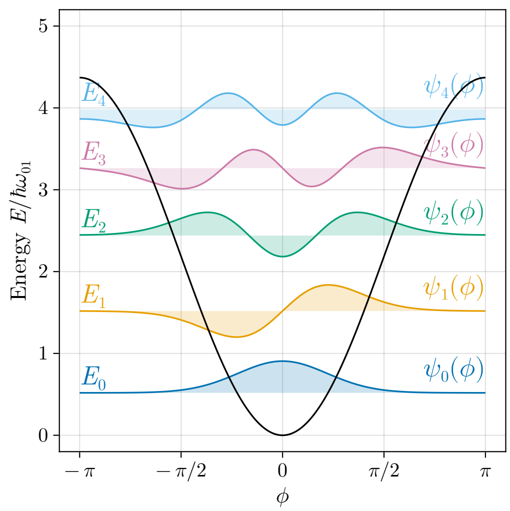

Figure 2.10: Energies of the first five eigenstates of a Cooper-pair box with $n_g = 0.3$ and $E_J/E_C = 33.3$. The wavefunctions $\psi_k(\phi)$ illustrate how the distributions are confined by the cosine potential well $V(\phi) = E_J(1-\cos\phi)$.

An alternative approach is to rewrite Eq. (2.4.1) in the charge basis spanned by vectors $|n\rangle$ such that $\hat{n}\,|n\rangle = n\,|n\rangle$. Then the first term of the Hamiltonian becomes

$$4E_C\sum_{m,n}|m\rangle\langle m|\,(\hat{n}-n_g)^2\,|n\rangle\langle n| = 4E_C\sum_{n=-\infty}^{\infty}(n-n_g)^2\,|n\rangle\langle n|\,. \tag{2.4.3}$$

Using the Fourier transforms

$$|n\rangle = \frac{1}{\sqrt{2\pi}}\int_0^{2\pi}\mathrm{d}\phi e^{in\phi}\,|\phi\rangle \tag{2.4.4}$$

$$|\phi\rangle = \frac{1}{\sqrt{2\pi}}\sum_{n=-\infty}^{\infty}e^{-in\phi}\,|n\rangle\,, \tag{2.4.5}$$

To transform the Josephson energy term, we first investigate

$$\begin{aligned} e^{i\hat{\phi}}\,|n\rangle &= \frac{1}{\sqrt{2\pi}}\int_0^{2\pi}\mathrm{d}\phi e^{in\phi}e^{i\hat{\phi}}\,|\phi\rangle \\ &= \frac{1}{\sqrt{2\pi}}\int_0^{2\pi}\mathrm{d}\phi e^{i(n+1)\phi}\,|\phi\rangle \\ &= |n+1\rangle\,, \end{aligned} \tag{2.4.6}$$

and similarly $\exp(-i\hat{\phi})\,|n\rangle = |n-1\rangle$. Then the Josephson energy term can be transformed as

$$\begin{aligned} -E_J\sum_{m,n}|m\rangle\langle m|\cos\hat{\phi}\,|n\rangle\langle n| &= -\frac{E_J}{2}\sum_{m,n}|m\rangle\langle m|\,(e^{i\hat{\phi}}+e^{-i\hat{\phi}})\,|n\rangle\langle n| \\ &= -\frac{E_J}{2}\sum_{m,n}\big(|m\rangle\langle m|\,e^{i\hat{\phi}}\,|n\rangle\langle n| + |m\rangle\langle m|\,e^{-i\hat{\phi}}\,|n\rangle\langle n|\big) \\ &= -\frac{E_J}{2}\sum_{n}\big(|n+1\rangle\langle n| + |n\rangle\langle n+1|\big). \end{aligned} \tag{2.4.7}$$

Therefore

$$\hat{\mathcal{H}}_{\mathrm{CPB}} = 4E_C\sum_{n=-\infty}^{\infty}(n-n_g)^2\,|n\rangle\langle n| - \frac{E_J}{2}\sum_{n=-\infty}^{\infty}\big(|n+1\rangle\langle n| + |n\rangle\langle n+1|\big). \tag{2.4.8}$$

To numerically find the eigenenergies of Eq. (2.4.8), we can truncate the charge basis to a closed range $[-n_{\mathrm{cut}}, n_{\mathrm{cut}}]$. Then the Hamiltonian becomes a square matrix of dimension $2n_{\mathrm{cut}}+1$, eigenvalues and eigenvectors of which can be found with diagonalizing algorithms. Wavefunctions in the phase basis can be derived by Fourier transforming the charge basis eigenvectors. The first few states are shown in Fig. (2.10).

Due to the offset charge n_g dependence in the capacitive energy term of the Hamiltonian, the Cooper-pair box is very sensitive to charge fluctuations. Fig. (2.11(a)) shows the energies of the lowest levels for a device investigated in Ref. [43]. In devices like this, the capacitance C comes from the parasitic capacitor included in the Josephson junction and is usually very small, resulting in $E_J/E_C \ll 1$. Even operated at the sweet spots at half-integer n_g where E_{01} is protected from Δn_g up to first order, Cooper-pair boxes still have difficulty demonstrating long-term stability [28].

To mitigate the charge sensitivity, an option is to increase the ratio E_J/E_C to lower the effect of the capacitive energy fluctuation on the total energy. This leads to the invention of the

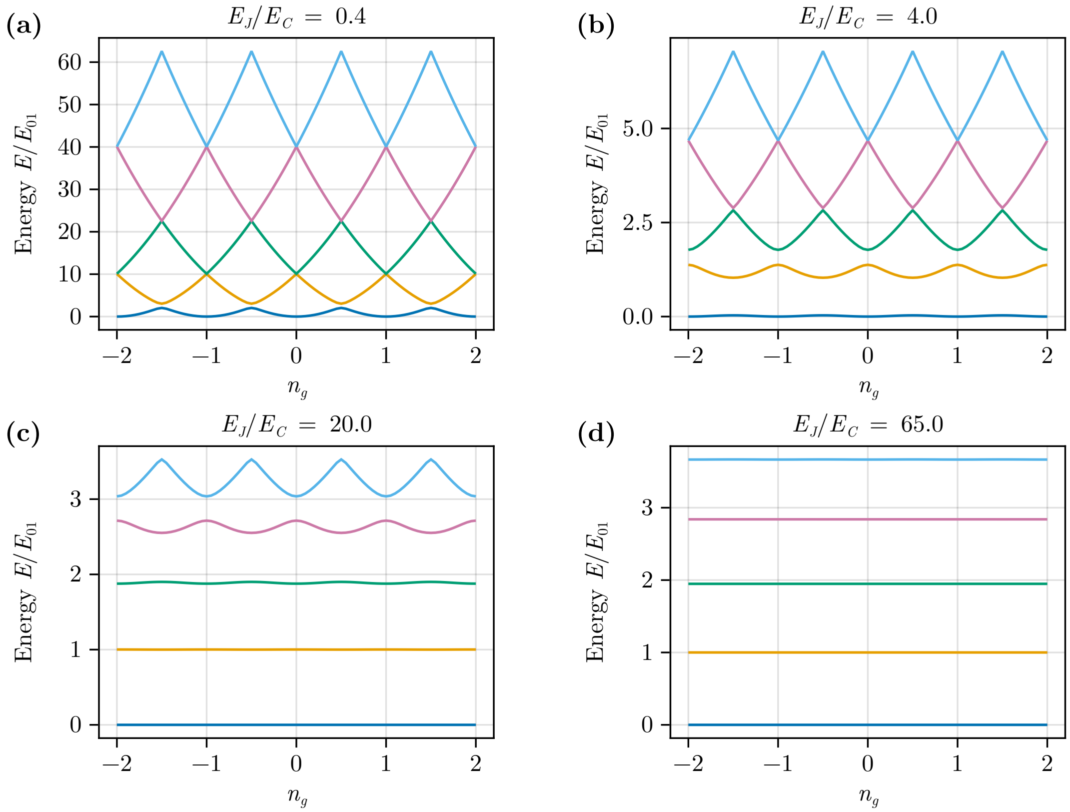

Figure 2.11: The energies of the first few levels of the Cooper-pair box as a function of n_g. All levels are normalized by E_{01} defined as the energy difference between the first two states when $n_g = 0.5$. We can clearly observe from the trend a decrease of offset charge dependence.

transmon where the Josephson junction is shunted by a large capacitor with smaller E_C. As it turns out, charge dispersion, defined as $\max(E_m) - \min(E_m)$, depends exponentially on the quantity $\sqrt{E_J/E_C}$ [28]. If we compare the energy levels of a transmon with $E_J/E_C = 65$ shown in Fig. (2.11(d)) to Fig. (2.11(a)), we can observe that dependence on the offset charge is almost completely lifted. Meanwhile, the ironed out energies leave us with smaller anharmonicity. We can define a relative anharmonicity α_r as

$$\alpha_r = \frac{\alpha}{\omega_{01}} \approx -\frac{E_C}{\sqrt{8E_J E_C}} = -\sqrt{\frac{E_C}{8E_J}}. \tag{2.4.9}$$

As a result, the transmon benefits exponentially from the increasing ratio E_J/E_C at the cost of slowly losing its anharmonicity. E_J/E_C of most transmons fall in the range $[30, 100]$.

2.5 The Jaynes–Cummings Hamiltonian

In this last section, we will investigate the model where we couple a transmon to an LC oscillator for readout purpose with the tools we developed so far. The model can be modified from Fig. (2.4) by replacing one LC oscillator with a transmon as shown in Fig. (2.12).

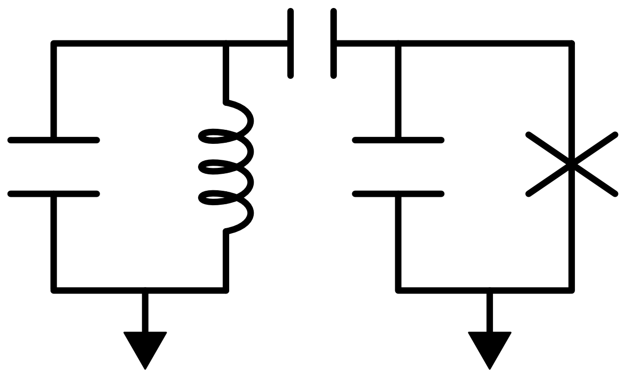

Figure 2.12: A transmon qubit capacitively coupled to a linear resonator. This architecture sits at the core of circuit-QED in that it allows for probing the qubit state non-destructively through the reasonator.

We can then substitute one harmonic oscillator energy term in Eq. (2.1.43) with Eq. (2.3.8) and get the system Hamiltonian

$$\begin{aligned}\hat{\mathcal{H}}_{\rm JC} &= \hat{\mathcal{H}}_{\rm LC} + \hat{\mathcal{H}}_{\rm transmon} + \hat{\mathcal{H}}_{\rm int} \\ &= \hbar\omega_r \hat{a}^\dagger \hat{a} + \frac{1}{2}\hbar\omega_q \hat{\sigma}^z + g(\hat{a}^\dagger \hat{\sigma}^- + \hat{a}\hat{\sigma}^+). \end{aligned} \tag{2.5.1}$$

Eq. (2.5.1) is known as the Jaynes–Cummings Hamiltonian [78].

We are interested in studying Eq. (2.5.1) in the dispersive limit [79] where the frequency detuning between the resonator and the qubit $|\Delta| = |\omega_q - \omega_r|$ is much greater than the coupling strength g as well as the decay rates of them. In this limit direct photon exchange between the qubit and the resonator is not allowed to happen. Instead, the coupling can only dispersively push and pull their frequencies.

To derive an approximate form of Eq. (2.5.1) in the dispersive limit $\Delta \gg g$, we can make a Schrieffer–Wolff transformation by transforming the Hamiltonian with the unitary $\exp(\hat{S})$ where

$\hat{S} = \lambda(\hat{a}\hat{\sigma}^+ - \hat{a}^\dagger\hat{\sigma}^-)$ with $\lambda = g/\Delta \ll 1$. Then

$$\begin{aligned}\hat{\mathcal{H}}_{\text{dispersive}} &= e^{\hat{S}}\hat{\mathcal{H}}_{\text{JC}}e^{-\hat{S}} \\ &\approx \hat{\mathcal{H}}_{\text{JC}} + [\hat{S}, \hat{\mathcal{H}}_{\text{JC}}] + \frac{1}{2}[\hat{S}, [\hat{S}, \hat{\mathcal{H}}_{\text{JC}}]] \\ &= \hbar\omega_r\hat{a}^\dagger\hat{a} + \frac{1}{2}\hbar\tilde{\omega}_q\hat{\sigma}^z + \hbar\chi\hat{\sigma}^z\hat{a}^\dagger\hat{a}, \end{aligned} \tag{2.5.2}$$

where the dispersive shift $\chi = g^2/\Delta$ and the Lamb-shifted qubit frequency $\tilde{\omega}_q = \omega_q + \chi$. If we go beyond the reduced spin-1/2 model and include the second excited state of the transmon, the dispersive shift is modified into [28]

$$\chi = \frac{g^2\alpha}{\Delta(\Delta + \alpha)}. \tag{2.5.3}$$

There are two alternative perspectives to interpret the third term in Eq. (2.5.2). We can let the resonator energy term to absorb it and become $\hbar(\omega_r + \chi\hat{\sigma}^z)\hat{a}^\dagger\hat{a}$. In this interpretation, the resonator's frequency depends on the state of the qubit $\langle\hat{\sigma}^z\rangle$. The resonator frequency undergoes a 2χ shift when we flip the qubit state. This means that we can measure the qubit state in a quantum non-demolition (QND) manner by measuring the resonator frequency. In experiments, this is often realized by probing the resonator at ω_r and monitoring change in the magnitude or phase of the transmitted signal. In general, larger dispersive shift makes it easier to distinguish different states. However, to achieve so we have to either decrease the detuning Δ or increasing the coupling strength g. In either cases we may break the condition required for both RWA and Eq. (2.5.2). A critical photon number [41, 55] is defined as $n_{\text{crit}} = (\Delta/2g)^2$ for transmon-resonator systems. This quantity regulates the amount of photons we can put into the resonator before the dispersive approximation fails and higher-order physics starts to play a role. Apparently n_{crit} decrease when we increase 2χ. This essentially puts a higher bound on the values of dispersive shift we can achieve. For common transmon devices, 2χ ranges from $\sim 100\,\text{kHz}$ to $\sim 10\,\text{MHz}$. In order to resolve the dispersive shift in experiment, we require the dispersive shift to be not smaller than the resonator's full width at half maximum (FWHM). This can be achieved by working with resonators with large quality factors Q.

A second way to interpret Eq. (2.5.2) is to bundle the third term with the qubit energy as $\hbar/2(\tilde{\omega}_q + 2\chi\hat{a}^\dagger\hat{a})\hat{\sigma}^z$. In this view, the qubit frequency now sees an extra ac Stark shift [80, 81] proportional to the number of photons in the resonator $\langle\hat{a}^\dagger\hat{a}\rangle$. In some cases, this ac Stark shift can serve as a tool and allow people to learn and manipulate the quantum state within the resonator [81, 82, 83]. However, the ac Stark shift also causes unwanted qubit frequency fluctuations due to thermal population of the resonator, which will cause qubit to lose its phase information. To suppress this type of error, it is desirable to keep the temperature of the resonator as well as the qubit low.

There are more factors than the ac Stark shift that can cause transmon qubits to undergo errors such as uncontrolled degrees of freedom or coupling to the environment. In general, these errors fall into one of two categorizes: relaxation (energy decay) and dephasing (phase randomization).

Relaxation error, or longitudinal error, involves the transition of a qubit from its excited state $|1\rangle$ to its ground state $|0\rangle$ or vice versa, accompanied by the exchange of energy with the environment. It can be modeled by a relaxation rate $\Gamma_1 = 1/T_1 = \Gamma_+ + \Gamma_-$, with T_1 being the relaxation time. Since the circuit-QED devices are mostly operated at $\sim 10\,\mathrm{mK}$ as discussed in section 2.1.1, we can derive from Boltzmann statistics that

$$\frac{\Gamma_+}{\Gamma_-} = e^{-\frac{\hbar\omega_q}{k_B T}} \ll 1, \tag{2.5.4}$$

which means we often only refer to the energy decay when reporting the transmon's T_1.

Several mechanisms contribute to relaxation in transmon qubits, including dielectric loss, quasiparticle tunneling, the Purcell effect, and material defects. Dielectric loss originates from the absorption of electromagnetic energy by insulating materials in the qubit structure, such as the Josephson junction barrier or substrate interfaces. This loss is characterized by the dielectric loss tangent $\tan\delta$, with the relaxation rate expressed as

$$\Gamma_1^{\text{dielectric}} = \omega_q \sum_i p_i \tan\delta_i, \tag{2.5.5}$$

where p_i stands for the ratio of stored electromagnetic energy for each different material or surface with corresponding loss tangent $\tan\delta_i$. Quasiparticle tunneling constitutes another relaxation pathway, in which non-equilibrium quasiparticles in the superconducting film dissipate energy as they traverse the Josephson junction. The corresponding relaxation rate is proportional to the quasiparticle density n_{qp}, underscoring the importance of suppressing quasiparticle generation[84]. The Purcell effect, a phenomenon intrinsic to circuit-QED systems, results from the emission of qubit energy mediated by a coupled resonator. This can be understood by going back to Eq. (2.5.1) where we derived the Jaynes–Cummings Hamiltonian for a qubit-resonator system. Due to the presence of the coupling term, the 'bare' qubit states got hybridized with the 'bare' resonator states. We can express the dressed state in terms of the bare states as $\widetilde{|e,0\rangle} = |e,0\rangle + (g/\Delta)\,|g,1\rangle$. Then if the resonator loses energy to the environment it couples to, e.g. a semi-infinite transmission line, at a rate κ, the dressed qubit state will decay accordingly at a rate of

$$\Gamma_1^{\mathrm{Purcell}} = \left(\frac{g}{\Delta}\right)^2 \kappa. \tag{2.5.6}$$

Finally, relaxation can also arise from material defects, particularly two-level systems (TLS) at interfaces or within insulating materials [85, 86, 87].

Experimental determination of T_1 typically involves time-domain measurements, such as excitation and decay protocols, in which the qubit is initialized in the $|1\rangle$ state and the population decay is monitored as a function of time. Recent advances have extended T_1 values for transmon qubits to beyond 100 µs [88, 89, 90], though further improvements remain necessary for the implementation of fault-tolerant quantum computing.

Dephasing error, or transversal error, refers to the loss of phase coherence and can be quantified with a dephasing rate of $\Gamma_2 = 1/T_1 = \Gamma_1/2 + \Gamma_\phi$. The first term accounts for loss of phase information solely due to relaxation. The second term is the pure dephasing rate and arises primarily from fluctuations in the qubit's transition frequency.

We already discussed about how photon number fluctuation in the readout resonator can ac Stark shift the qubit frequency and thus cause dephasing. The remaining causes that can dephase a transmon include residual sensitivity to charge noise, low-frequency $1/f$ magnetic flux noise [91] and interactions with TLS's.

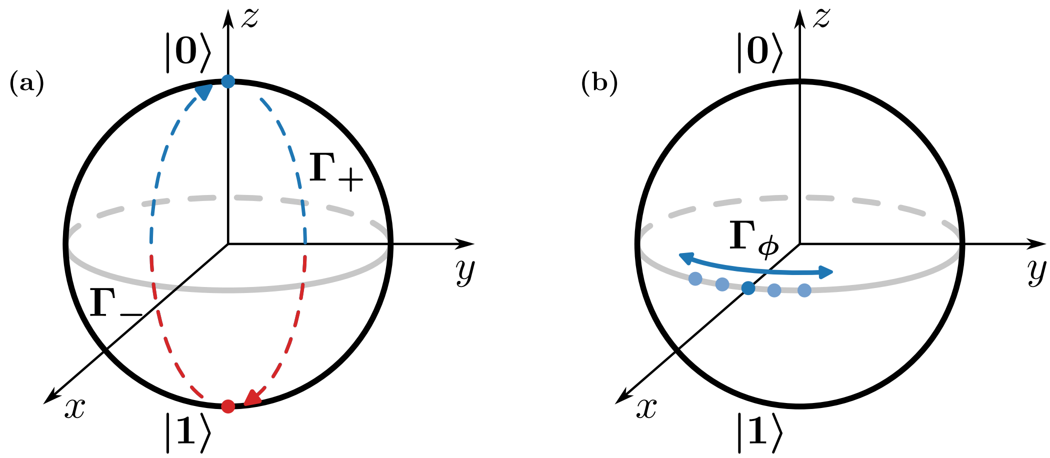

Figure 2.13: Effect of noise shown on the Bloch sphere. (a) Relaxation error can either flip $|0\rangle$ to $|1\rangle$ or $|1\rangle$ to $|0\rangle$. (b) A superposition state will precess randomly on the equator due to dephasing error. Adapted from [76].

The Bloch-Redfield formalism [92, 93, 94] is helpful in providing both quantitative and visual insights into a qubit undergoing error processes. The density matrix ρ of a qubit prepared at arbitrary pure state $|\psi\rangle = \alpha|0\rangle + \beta|1\rangle$ is

$$\rho = |\psi\rangle\langle\psi| = \begin{bmatrix} |\alpha|^2 & \alpha\beta^* \\ \alpha^*\beta & |\beta|^2 \end{bmatrix}. \tag{2.5.7}$$

The Bloch sphere is a geometric representation of a qubit's state, where the state is depicted as a point on or inside a unit sphere. The north and south poles represent the $|0\rangle$ and $|1\rangle$, respectively, while points on the equator correspond to superpositions of these states with equal probabilities but varying relative phases. In the presence of both relaxation and dephasing error, the density matrix evolves in time such that [76]

$$\rho(t) = \begin{bmatrix} 1 + (|\alpha|^2 - 1)e^{-\Gamma_1 t} & \alpha\beta^* e^{-\Gamma_2 t} \\ \alpha^*\beta e^{-\Gamma_2 t} & |\beta|^2 e^{-\Gamma_1 t} \end{bmatrix}. \tag{2.5.8}$$

Fig. (2.13) shows how the qubit state are affected by the noise terms on the Bloch sphere.

2.6 Summary

In summary, this chapter has provided a detailed journey through the theoretical framework underlying circuit-QED. Beginning with the classical LC oscillator and progressing to its quantum description via canonical quantization, we developed the tools necessary to analyze both isolated and driven harmonic oscillators, as well as coupled oscillator systems. The treatment was extended to distributed circuits through the modeling of finite and semi-infinite transmission lines, leading to the derivation of the quantum Langevin equation and the input–output formalism crucial for understanding measurement and dissipation in these systems. Building on these foundations, we introduced superconductivity and the Josephson effect as mechanisms to impart nonlinearity, culminating in the design of the transmon qubit that overcomes charge noise challenges. Finally, the chapter culminated with the Jaynes–Cummings Hamiltonian and its dispersive limit, offering insight into the qubit–resonator interactions that are pivotal for readout and coherent quantum control in superconducting quantum computing architectures.

Chapter 3

Experiment Setup

This chapter provides an overview of the experimental infrastructure where our experiments take place. As mentioned in the previous chapter, the quantum phenomena we want to observe and manipulate require non-ambient conditions. It takes effort to create the suitable environment, tailor the signals to be seen by the device, route the signal to the device as well as pick up and analyze the signals coming back from the device. By interweaving these elements, the chapter elucidates how careful integration and engineering of cryogenic and ambient components collectively make the experiments feasible.

3.1 Dilution Refrigerator

At the core of the setup is the dilution refrigerator, or "fridge". Dilution refrigerators achieve continuous cooling to temperatures in the millikelvin range by exploiting the unique thermodynamic properties of helium-3 (^{3}He)–helium-4 (^{4}He) mixtures. Below approximately $870\,\mathrm{mK}$, the mixture spontaneously phase-separates into a ^{3}He-rich (concentrated) phase and a ^{3}He-poor (dilute) phase—with the dilute phase retaining about 6.6% ^{3}He even as $T \to 0\,\mathrm{K}$. The cooling effect is generated in the mixing chamber, where ^{3}He atoms continuously cross the phase boundary from the concentrated phase into the dilute phase. This process is endothermic, meaning that it absorbs heat from the environment, thereby lowering the temperature of the mixing chamber. The refrigerator's operation relies on a closed-loop circulation of ^{3}He, maintained by vacuum pumps at room temperature and a series of highly efficient heat exchangers that pre-cool the incoming ^{3}He to near the mixing chamber temperature. The overall cooling power of the refrigerator depends on both the molar circulation rate of ^{3}He and the temperature of the mixing chamber.

Key components of the dilution refrigerator include the mixing chamber (where phase separation and dilution occur), the still (which facilitates the removal of ^{3}He from the dilute phase), and multiple heat exchangers (which minimize the temperature difference between the circulating helium streams). Modern designs often incorporate cryogen-free precooling via pulse tube coolers, reducing operational complexity and reliance on liquid cryogens. Fig. (3.1) shows a peek into the Bluefors XLD dilution refrigerator.

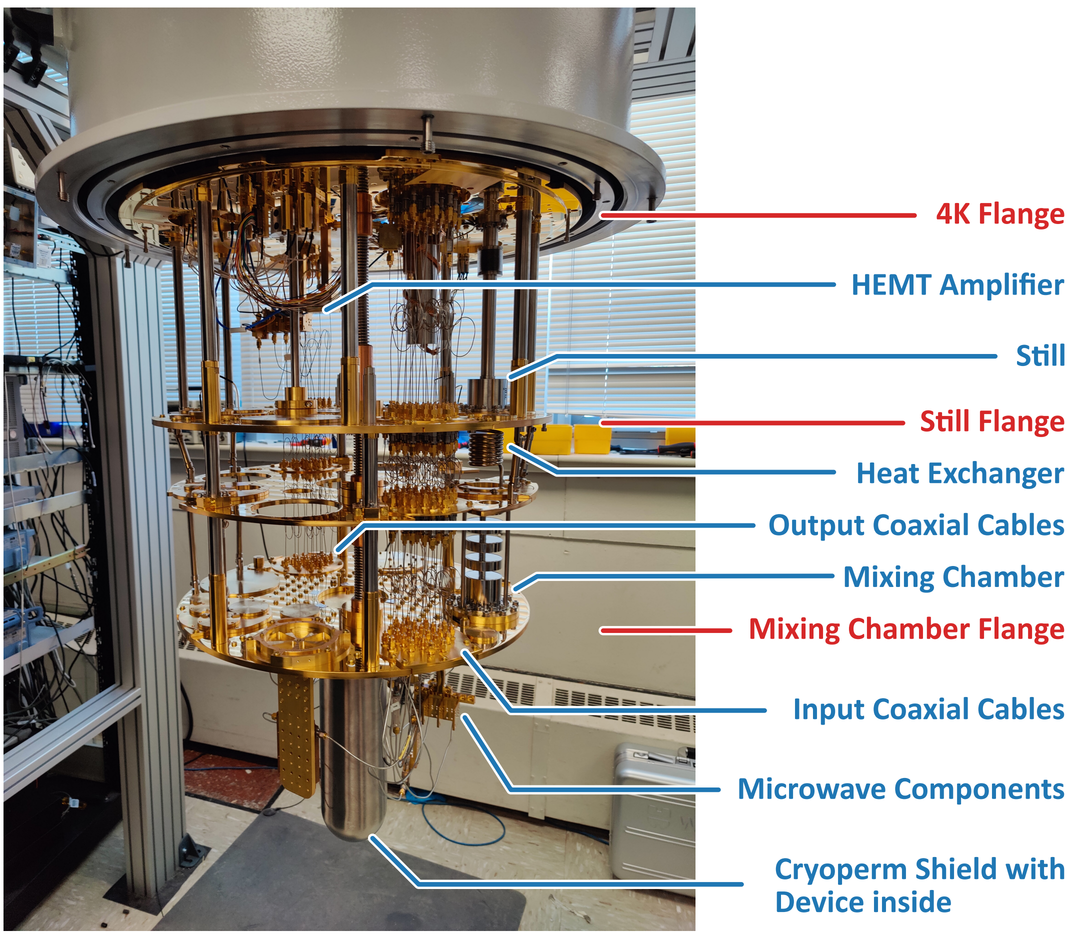

Figure 3.1: Inside of a dilution refrigerator. The different stages are separated by flanges at different temperatures when the fridge operation is stable. Shields that block thermal radiation from stages at higher temperature are removed. Devices are mounted to the bottom flange which is cooled by the mixing chamber. The input and output wires have to thread through the stages, getting thermalized along the way. The device is mounted to metal brackets in the silver Cryoperm shield.

3.2 Control and Measure the Qubit

An example of a circuit-QED experiment setup is shown in Fig. (3.2), which includes signal synthesis, signal routing inside the fridge and signal acquisition and digital signal processing at room temperature. This section aims to provide general discussions about the different parts of this measurement system.

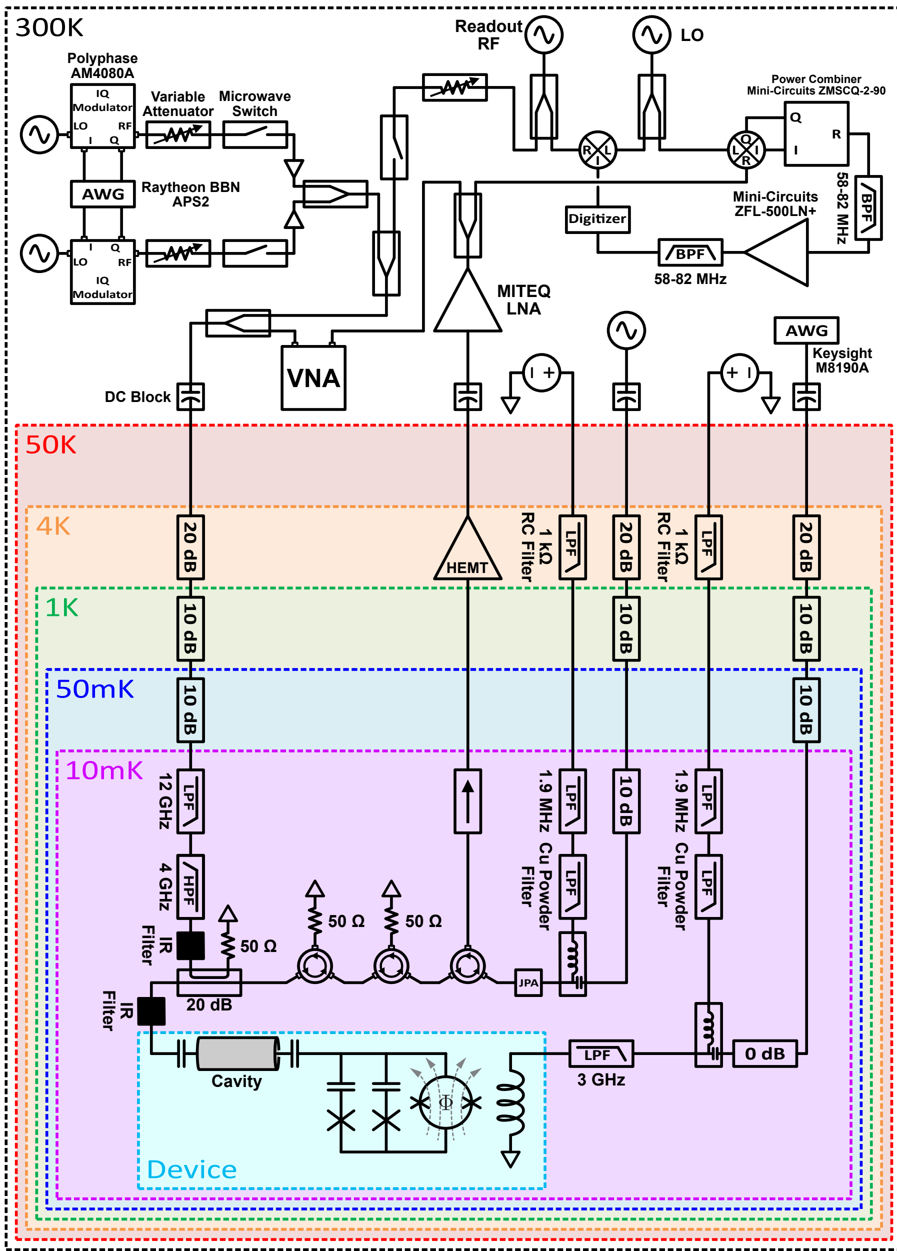

Figure 3.2: Fridge wiring schematic.

3.2.1 Qubit Control Pulse with Single-sideband Modulation

Our anatomy of the measurement system will start with the room temperature electronics shown in the top left corner of Fig. (3.2).

High-fidelity quantum control in superconducting circuits critically depends on the precise generation of shaped microwave pulses. These pulses drive coherent transitions between qubit states, implementing single- and multi-qubit gates. In the dispersive regime of circuit quantum electrodynamics (cQED), the typical control paradigm involves addressing the transition between the ground $|g\rangle$ and first excited state $|e\rangle$ of a transmon qubit. To achieve spectrally selective and phase-programmable control while minimizing leakage to higher levels, shaped pulses are synthesized via in-phase and quadrature (IQ) modulation of a local oscillator (LO) tone using arbitrary waveform generators (AWG) and microwave mixers.

The backbone of qubit drive pulse generation is an IQ modulator (Polyphase AM4080A), a four-port nonlinear device that modulates a continuous wave (CW) microwave LO with two low-frequency analog signals: the in-phase component I(t) and the quadrature component Q(t). These baseband waveforms are produced by an AWG (Raytheon BBN APS2), and encode both the amplitude and phase of the desired drive envelope.

Assuming the LO provides a carrier at frequency ω_d, the output at the IQ modulator RF port is ideally given by:

$$V(t) = I(t)\cos(\omega_d t) - Q(t)\sin(\omega_d t). \tag{3.2.1}$$

This expression can be equivalently recast in polar form as:

$$V(t) = A(t)\cos[\omega_d t + \phi(t)], \tag{3.2.2}$$

where the instantaneous amplitude and phase are:

$$A(t) = \sqrt{I(t)^2 + Q(t)^2} \tag{3.2.3}$$

$$\phi(t) = \arctan\left[\frac{Q(t)}{I(t)}\right]. \tag{3.2.4}$$

This formalism enables the implementation of arbitrary qubit rotation gates by modulating $A(t)$ and $\phi(t)$. For example, Gaussian or DRAG-shaped envelopes [95, 96, 97] can be applied to minimize spectral leakage and leakage to non-computational states.

To minimize the impact of carrier leakage–residual LO power that appears even when $I(t) = Q(t) = 0$–single-sideband (SSB) modulation is often employed. In this scheme, $I(t)$ and $Q(t)$ are themselves modulated by an intermediate frequency (IF) tone at ω_{IF} typically tens of MHz:

$$I(t) = A_I(t)\cos(\omega_{\mathrm{IF}} t) \tag{3.2.5}$$

$$Q(t) = A_Q(t)\sin(\omega_{\mathrm{IF}} t). \tag{3.2.6}$$

Substituting into the IQ modulator output yields:

$$V(t) = \frac{A_I(t) + A_Q(t)}{2}\cos[(\omega_d + \omega_{\mathrm{IF}})t] + \frac{A_I(t) - A_Q(t)}{2}\cos[(\omega_d - \omega_{\mathrm{IF}})t]. \tag{3.2.7}$$

The result contains two spectral sidebands centered at $\omega_d \pm \omega_{\mathrm{IF}}$. By setting $A_I(t) = A_Q(t)$, one can suppress the lower sideband at $\omega_d - \omega_{\mathrm{IF}}$, retaining only the upper sideband at $\omega_d + \omega_{\mathrm{IF}}$. This allows the effective qubit drive frequency to be set as $\omega_q = \omega_d + \omega_{\mathrm{IF}}$, while the carrier tone at ω_d remains far detuned from the qubit. This significantly mitigates residual excitation and spurious Stark shifts from LO leakage.

3.2.2 Heterodyne Measurement

As discussed in section 2.5, in the dispersive circuit-QED regime, qubit state can be readout by measuring the frequency of the readout cavity that is coupled to the qubit. Such readout cavities have typical frequencies ranging from 4 GHz to 10 GHz, where direct digitization of readout signals is technically challenging due to the demand of high-speed analog-to-digital converters (ADCs). Heterodyne detection addresses this by down-converting high-frequency signals to intermediate frequencies (IF) compatible with commercially available ADCs.

In the setup shown in Fig. (3.2), we use a Keysight N5183M signal generator as the readout RF to generate microwave signal near the readout cavity frequency $f_{\mathrm{RO}} = 8.715\,\mathrm{GHz}$. A power combiner (Mini-Circuits ZX10-2-183-S+) divides the readout signal into two copies, one of which is sent into the fridge while the other is reserved at room temperature as a reference signal. Another Keysight N5183M signal generator takes on the role of a local oscillator (LO), generating microwave signal at a frequency that is lower than f_{RO} by an amount of $f_{\mathrm{IF}} = 62.5\,\mathrm{MHz}$. The output signal coming from the fridge will be filtered and amplified through several stages before being down-converted with the LO signal at an IQ mixer. Then, the IF output from the mixer will carry the information of the readout cavity at a frequency of 62.5 MHz and can be acquired as a time trace of the voltage $V(t)$ by the digitizer (AlazarTech ATS9373).

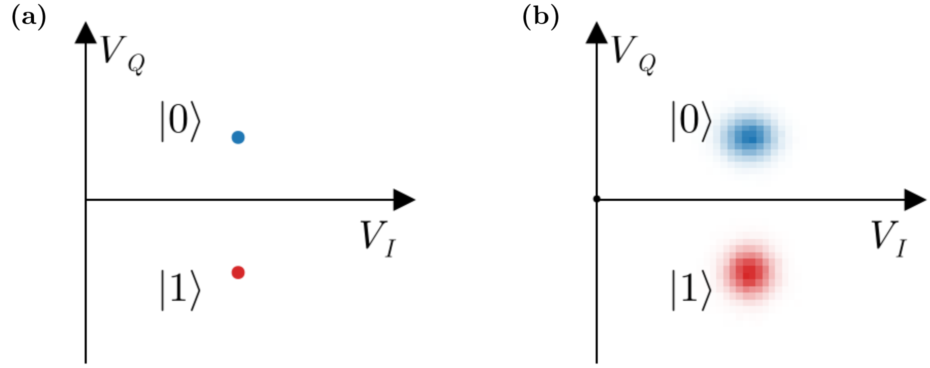

Figure 3.3: The measurement outcomes when qubit is at different states in a (a) noise-less case (b) noisy case.

To extract the quadrature components V_I and V_Q from the signal, we first consider a noise-less case where $V(t) = A\cos(\omega_{\mathrm{IF}}t + \phi) = I\cos(\omega_{\mathrm{IF}}t) - Q\sin(\omega_{\mathrm{IF}}t)$ with

$$A = \sqrt{I^2 + Q^2} \tag{3.2.8}$$

$$\phi = \arctan\left[\frac{Q}{I}\right]. \tag{3.2.9}$$

Then the V_I and V_Q can be extracted by calculating the integrals

$$\frac{2}{\tau}\int_0^\tau V(t)\cos(\omega_{\mathrm{IF}}t)\,\mathrm{d}t = \frac{2}{\tau}V_I\int_0^\tau \cos^2(\omega_{\mathrm{IF}}t)\,\mathrm{d}t - \frac{2}{\tau}V_Q\int_0^\tau \cos(\omega_{\mathrm{IF}}t)\sin(\omega_{\mathrm{IF}}t)\,\mathrm{d}t$$
$$= V_I \quad \text{when } \tau \text{ is integer multiples of } T_{\mathrm{IF}} = 1/f_{IF} \tag{3.2.10}$$
$$-\frac{2}{\tau}\int_0^\tau V(t)\sin(\omega_{\mathrm{IF}}t)\,\mathrm{d}t = \frac{2}{\tau}V_Q\int_0^\tau \sin^2(\omega_{\mathrm{IF}}t)\,\mathrm{d}t - \frac{2}{\tau}V_I\int_0^\tau \cos(\omega_{\mathrm{IF}}t)\sin(\omega_{\mathrm{IF}}t)\,\mathrm{d}t$$
$$= V_Q \quad \text{when } \tau \text{ is integer multiples of } T_{\mathrm{IF}} = 1/f_{IF}. \tag{3.2.11}$$

If we plot (V_I, V_Q) on a plane, the readout cavity frequency shift due to qubit being at different state will appear as a phase rotation shown in Fig. (3.3(a)).

However, in real experiments, system noise fluctuates both the amplitude A and the phase ϕ of the acquired signal. As a result, when we build up statistics by repeating the same measurement many times (i.e. single-shot measurement), the (V_I, V_Q) pair will fluctuate and form two bivariate normal distributions on the IQ plane as shown in Fig. (3.3(b)). By drawing boundaries between these two distributions using algorithms such as Gaussian Mixture Model (GMM) or Support Vector Machine (SVM), we are able to distinguish the qubit state from each individual measurement outcome.

Chapter 4

Experiment: A Universal Quantum Gate Set for Strongly Coupled Transmons

High-fidelity single- and two-qubit gates are essential building blocks for a fault-tolerant quantum computer. While there has been much progress in suppressing single-qubit gate errors in superconducting qubit systems, two-qubit gates still suffer from error rates that are orders of magnitude higher. One limiting factor is the residual ZZ-interaction, which originates from a coupling between computational states and higher-energy states. While this interaction is usually viewed as a nuisance, here we experimentally demonstrate that it can be exploited to produce a universal set of fast single- and two-qubit entangling gates in a coupled transmon qubit system. To implement arbitrary single-qubit rotations, we design a new protocol called the two-axis gate that is based on a three-part composite pulse. It rotates a single qubit independently of the state of the other qubit despite the strong ZZ-coupling. We achieve single-qubit gate fidelities as high as 99.1% (for $\widetilde{|01\rangle} \leftrightarrow \widetilde{|11\rangle}$ transition) from randomized benchmarking measurements. We then demonstrate both a CZ gate and a CNOT gate. Because the system has a strong ZZ-interaction, a CZ gate can be achieved by letting the system freely evolve for a gate time $t_g = 53.8\,\mathrm{ns}$. To design the CNOT gate, we utilize an analytical microwave pulse shape based on the SWIPHT protocol for realizing fast, low-leakage gates. We obtain fidelities of 94.6% and 97.8% for the CNOT and CZ gates respectively from quantum progress tomography.

The content of this chapter is based on the following work:

- Junling Long et al. **A Universal Quantum Gate Set for Transmon Qubits with Strong ZZ Interactions**. Mar. 2021. DOI: 10.48550/arXiv.2103.12305. arXiv:

2103.12305 [quant-ph]

4.1 Introduction

Superconducting qubits hold promise as the main building blocks of a future fault-tolerant quantum computer [99, 100, 39]. In recent years, advances in both coherence times [29] and quantum gate fidelities [101, 102, 103], together with the inherent scalability of superconducting circuit architectures, have enabled demonstrations of superconducting quantum computers comprised of tens of qubits [104, 31, 105]. While single-qubit gate errors are routinely on the order of 0.01% [95, 106, 107], two-qubit gates across different qubit architectures have exhibited higher error rates, ranging from 0.1% up to the few-percent level [29, 108, 101, 109, 99, 102, 110, 111, 112, 113]. Thus, two-qubit gates remain a bottleneck in the performance of existing devices.

One significant source of two-qubit gate errors is the residual ZZ interaction between coupled qubits [102]. The ZZ interaction, also known as ZZ coupling or crosstalk, originates from a mixing between computational states and higher-energy states of the coupled qubits. It shifts the resonance frequency of one qubit conditionally on the state of another qubit. As a result, spurious phases are accumulated during gates, reducing fidelities. Some efforts have been devoted to suppressing the ZZ coupling using tunable couplers [114, 115] or hybrid superconducting qubits [116].

With the recent progress in tunable couplers [114, 115, 112], new opportunities open up for scalable architectures. In this context, it has been realized and demonstrated that the ZZ interaction can in fact be exploited for the implementation of a maximally entangling CZ gate [112]. This approach is very promising for scalability, as the qubits can be brought into the strong ZZ coupling regime to generate fast gates, while in the idling regime crosstalk is suppressed. Since tuning can be costly in terms of time and possibly coherence, it would be beneficial for the performance of the device to maximize the use of this strongly coupled regime by developing additional quantum gates that can be implemented within it. For example, a CNOT gate, despite being locally equivalent to a CZ, can be directly implemented using microwave fields [117, 118], eliminating the need for additional single-qubit rotations. The development of a broader toolset of gates applicable in the nonzero ZZ coupling regime is also important for cases where this coupling cannot be completely switched off, which is the generic situation in superconducting circuits.

In this work, we develop and demonstrate a universal set of fast gates that operate in the regime of strong ZZ interactions between capacitively coupled superconducting transmon qubits. To implement arbitrary single-qubit gates in this regime, we introduce a family of three-part composite pulses that effectively freeze the ZZ coupling so that one qubit is rotated independently of the state of another. We call these two-axis gates (TAGs). Randomized benchmarking is performed on each qubit to characterize the TAG fidelity, which we find to be 99.1%. We also demonstrate two types of maximally entangling gates: CZ and CNOT. The CZ gate is implemented via free evolution under the ZZ interaction, yielding a gate time of 53.8 ns. For the CNOT gate, we employ the SWIPHT protocol [117, 118, 119], which amounts to cleverly designing the pulse such that it acts on two transitions (the target and the nearest competing transition) in such a way that the net effect is the implementation of the target gate. This allows for a much faster gate compared to resolving the transitions. We create a maximally entangled state with the CNOT gate and obtain a fidelity of 98.2%, confirmed using quantum state tomography. Finally, we characterize the CZ and CNOT gates using quantum process tomography. The measured average gate fidelity is about 94.6% (97.8%) for the CNOT (CZ) gate.

This chapter is organized as follows. In section 4.2, we provide details about the transmon device and the effective ZZ Hamiltonian. Section 4.3 presents our two-axis gate designs for implementing arbitrary single-qubit rotations in the strong ZZ coupling regime. In section 4.4, we describe how we implement our CZ and CNOT gates, including a review of the SWIPHT protocol we use for the latter. Our randomized benchmarking measurements for the two-axis gates are presented in section 4.5, while our quantum state tomography and process tomography results for our two-qubit entangling gates are shown in section 4.6 and section 4.7, respectively. We conclude in section 4.8.

4.2 Device

The sample chip is shown in Fig. (4.1) (a) and (b), where optical images of the full device and a zoomed-in view of the two qubits (red and blue) are shown, respectively. The device consists of two floating transmon qubits [28] capacitively coupled to each other. Each transmon qubit is coupled to a coplanar waveguide readout resonator. The two readout resonators are coupled to the feedline in a hanger-style. Readout and control signals are all sent through the feedline. The capacitive components of each transmon are comprised of two identical rectangular pads [red (blue) for the first (second) qubit, as shown in Fig. (4.1)(b). Each pair of pads is connected by an $Al/AlO_x/Al$ Josephson junction that is fabricated with an overlap technique [120]. The full chip (except for the Josephson junctions) is made of 100 nm thick Niobium superconducting films. In this particular device, the two transmon qubits have frequencies of $\omega_1/2\pi = 5.075\,\mathrm{GHz}$ and $\omega_2/2\pi = 5.310\,\mathrm{GHz}$, and anharmonicities of $\alpha_1/2\pi = -260\,\mathrm{MHz}$ and $\alpha_2/2\pi = -340\,\mathrm{MHz}$. The relaxation and coherence times of the two qubits are measured to be $T_1^{(1)} = 76.98\,\mathrm{\mu s}$, $T_2^{*(1)} = 50.65\,\mathrm{\mu s}$, $T_1^{(2)} = 79.71\,\mathrm{\mu s}$, and $T_2^{*(2)} = 17.09\,\mathrm{\mu s}$. The equivalent grounded circuit model of the two capacitively coupled transmon qubits is shown in Fig. (4.1)(c). The Gaussian elimination method described in Ref. [121] was applied to convert the full floating circuit model to this simplified grounded circuit model. Note that the circuit of the readout resonators is not shown.

The level diagram of the device is shown in Fig. (4.1)(d). Two-qubit states are labeled as $|mn\rangle$, where m and n in the ket represent the mth state of the first qubit and nth state of the second qubit, respectively. The gray dashed lines in Fig. (4.1)(d) are the uncoupled two-qubit states, while the solid lines are the dressed two-qubit states with the always-on capacitive coupling. We only retain states involving up to two total excitations. The coupling between the $|10\rangle$ and $|01\rangle$ states is given by g_1. This coupling causes the two states to repel each other. As a result, the dressed qubit frequency shifts down (up) compared to the uncoupled qubit frequency of the first (second) qubit.

The couplings in the two-excitation manifold are between the $|20\rangle \leftrightarrow |11\rangle$, and $|11\rangle \leftrightarrow |02\rangle$ states, with the same strength, $g_2 \approx \sqrt{2}g_1$. As a result of the two couplings, the dressed energy

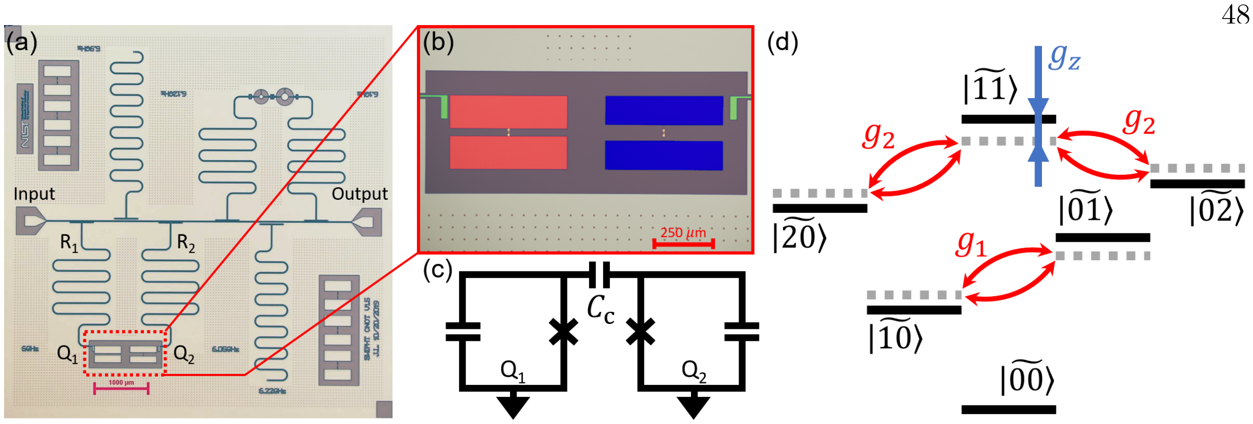

Figure 4.1: (a) Optical micrograph of the full chip including qubits, readout resonators, test Josephson junctions, and test resonators. (b) Zoomed-in view of the two floating qubits used in this experiment. Each qubit consists of two identical pads (red for the left qubit and blue for the right qubit) and a Josephson junction connecting the two pads. Each qubit is coupled to its own readout resonator (green). (c) Grounded circuit model of the capacitively coupled device. See Ref. [121] for how to obtain the equivalent grounded circuit model of floating qubits. (d) Energy level diagram of the two-qubit system. Gray dashed lines are uncoupled two-qubit energy levels. Solid lines represent the diagonalized energy levels of the two-qubit system with the coupling on. The red bidirectional curved arrows denote the swapping couplings between excitation-preserved states, and the coupling strengths are given by g_1 and g_2. g_z denotes the shift of $|11\rangle$ due to the couplings.

level $|\widetilde{11}\rangle$ is shifted up from the uncoupled $|11\rangle$ state. This makes the frequencies of the transitions $|\widetilde{01}\rangle \leftrightarrow |\widetilde{11}\rangle$ and $|\widetilde{10}\rangle \leftrightarrow |\widetilde{11}\rangle$ higher than those of $|\widetilde{00}\rangle \leftrightarrow |\widetilde{10}\rangle$ and $|\widetilde{00}\rangle \leftrightarrow |\widetilde{01}\rangle$, respectively, i.e., this is a state-dependent shift in qubit frequencies. In the computational subspace, defined by the dressed qubit states $|\widetilde{00}\rangle$, $|\widetilde{01}\rangle$, $|\widetilde{10}\rangle$, and $|\widetilde{11}\rangle$, the two-qubit system is described by the following Hamiltonian,

$$H_q/\hbar = \left(\omega_1 + \frac{g_z}{2}\right)\frac{\sigma_z^{(1)}}{2} + \left(\omega_2 + \frac{g_z}{2}\right)\frac{\sigma_z^{(2)}}{2} + g_z\frac{\sigma_z^{(1)}}{2}\frac{\sigma_z^{(2)}}{2}, \tag{4.2.1}$$

where $\sigma_z^{(i)} = (|\widetilde{1}\rangle\langle\widetilde{1}| - |\widetilde{0}\rangle\langle\widetilde{0}|)$ is the atomic inversion operator for the i^{th} qubit; ω_1 (ω_2) is the frequency of the first (second) qubit while the other qubit is in its ground state, i.e., it is the transition frequency of $|\widetilde{00}\rangle \leftrightarrow |\widetilde{10}\rangle$ ($|\widetilde{00}\rangle \leftrightarrow |\widetilde{01}\rangle$); g_z is the effective coupling strength determined by the amount of the up-shift of state $|\widetilde{11}\rangle$. We obtain a value of $g_z/2\pi = 9.29$ MHz from spectroscopy measurements. As shown in Eq. (4.2.1), the coupling between the two qubits in the computational subspace (dressed basis) is ZZ, but it originates from the transverse XX coupling between level $|11\rangle$ and the higher levels $|20\rangle$ and $|02\rangle$.

Measured transition frequencies of the device:

Qubit Transition	Frequency(GHz)
$\widetilde{\|00\rangle} \leftrightarrow \widetilde{\|10\rangle}$	5.075
$\widetilde{\|00\rangle} \leftrightarrow \widetilde{\|01\rangle}$	5.310
$\widetilde{\|01\rangle} \leftrightarrow \widetilde{\|11\rangle}$	5.084
$\widetilde{\|10\rangle} \leftrightarrow \widetilde{\|11\rangle}$	5.319
$\widetilde{\|10\rangle} \leftrightarrow \widetilde{\|20\rangle}$	4.815
$\widetilde{\|10\rangle} \leftrightarrow \widetilde{\|02\rangle}$	4.969

Table 4.1: Spectrum of the two-qubit system.

Average coherence times measured for each qubit:

	T_1(µs)	T_2^*(µs)
Q_1	76.98	50.65
Q_2	79.71	17.09

Table 4.2: Relaxation and Ramsey times of the qubits.

4.3 Arbitrary single-qubit rotations

Performing arbitrary single-qubit rotations is not a trivial task in a two-qubit system with strong ZZ coupling because the frequency of one qubit is conditional on the state of the other qubit. Here, we design a new type of single-qubit gate, called the two-axis gate (TAG), that unconditionally drives arbitrary single-qubit rotations in this ZZ-coupled, two-qubit system.

To explain how TAGs work, we take a $X_{\pi/2}$ rotation on the first qubit as an example. As shown in Fig. (4.2)(a), TAGs are implemented with three-part composite pulses. Note that the TAG protocol can be implemented using any pulse shapes for each of the three pieces. Here, we use square pulses in our experiments to facilitate pulse tune up. The first and third pulses (red) are identical, and we refer to them as Bloch sphere rotation (BR) pulses. The second pulse (blue) is called the qubit rotation (QR) pulse. For our $X_{\pi/2}$ rotation example, the center frequency of the TAG drive is set to be on resonance with the $\widetilde{|00\rangle} \leftrightarrow \widetilde{|10\rangle}$ transition. In the frame rotating at this frequency, the rotation axes for the three pulses of the TAG are all along the x-axis, as shown in Fig. (4.2)(b). The pulse strengths and durations are chosen such that all three pulses combine to rotate the state vector around the x-axis by $\pi/2$ and drive the original state $\widetilde{|00\rangle}$ to the final state $|-y\rangle = (\widetilde{|00\rangle} - i\widetilde{|10\rangle})/\sqrt{2}$.

Since the center frequency is detuned from the $\widetilde{|01\rangle} \leftrightarrow \widetilde{|11\rangle}$ transition by g_z as described by Eq. (4.2.1), the rotation axes of the BR and QR are both tilted from the x-axis in the xz plane by ϕ_{BR} and ϕ_{QR}, respectively, as shown in Fig. (4.2)(c). The BR pulses can be treated as a rotation of the Bloch sphere around the blue axis in the opposite direction. This is the reason why we call it a Bloch sphere rotation. When the first BR pulse is applied, we require it to rotate the Bloch sphere such that the x-axis after the rotation coincides with the QR axis, i.e., the blue axis in Fig. (4.2)(c). To achieve this, two conditions need to be satisfied. First, the red axis needs to be the bisector of the angle formed between the blue- and x-axis, i.e., $\phi_{QR} = 2\phi_{BR}$. Second, the rotation angle of the BR pulse needs to be π or $-\pi$. In the rotated Bloch sphere, since the QR (blue) axis is on the x-axis, we can perform a rotation around the x-axis by $\pi/2$. After the QR pulse, we apply the BR pulse again to rotate the Bloch sphere around the BR (red) axis by another π angle to get back to the original Bloch sphere. Treating a BR pulse as a rotation of the Bloch sphere is a good way to understand the TAG. If we treat all the pulses in the TAG as rotations of a state vector, we can see the trajectories on both Bloch spheres. This is shown in Fig. (4.2)(c). When the first BR pulse is applied, the rotated state vector becomes perpendicular to the blue axis. Then, the QR pulse is applied to rotate the state vector by $\Theta = \pi/2$. Finally, the BR pulse is applied again to bring the state to $|-y\rangle$.

Similarly, we can design TAGs that rotate the state of one qubit around the x-axis by other arbitrary angles. To perform a y-rotation with the TAG, one can just add a 90° global phase shift to the TAG. Arbitrary rotations can be performed by combinations of x and y-rotations.

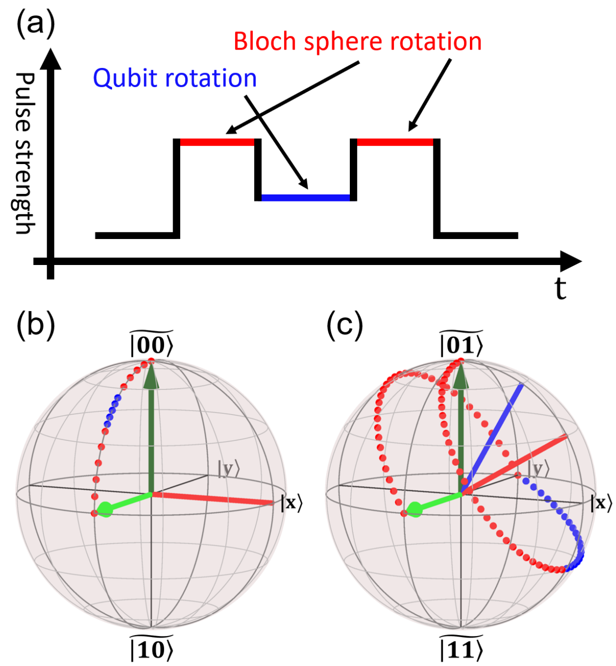

Figure 4.2: (a) A square shaped two-axis gate that implements a $X(\pi/2)$ on the first qubit. (b) and (c) show the trajectories of the state vector for the $\widetilde{|00\rangle} \leftrightarrow \widetilde{|10\rangle}$ and $\widetilde{|01\rangle} \leftrightarrow \widetilde{|11\rangle}$ transitions, respectively. In (b) and (c) the initial state is $\widetilde{|00\rangle}$, as denoted by the dark green arrow, while the final state is $|-y\rangle = (\widetilde{|00\rangle} - i\widetilde{|10\rangle})/\sqrt{2}$, which is denoted by the light green arrow. The red (blue) dots in (a) and (c) denote the trajectories corresponding to the BR (QR) pulses.

4.4 Two-qubit entangling gates

In this section, we describe how we realize two different two-qubit entangling gates, a CZ gate and a generalized CNOT gate, on our device.

4.4.1 A controlled-Z gate by free evolution

With the ZZ coupling, free evolution of the system is, in fact, a controlled-phase gate. By transforming the Hamiltonian in Eq. (4.2.1) to the rotating frame of ω_1 and ω_2 for the first and second qubit, respectively, and adding a constant energy shift $g_z/4$, one obtains

$$H_q^{rot}/\hbar = g_z\widetilde{|11\rangle}\widetilde{\langle 11|}. \tag{4.4.1}$$

Note that we used the fact that $\sigma_z^{(i)}$ is defined in the dressed two-qubit basis to obtain this result. Also note that adding a constant energy shift to the Hamiltonian only produces a global phase; it does not change the dynamics of the two qubits. The time evolution operator of this Hamiltonian above is given by

$$U(t) = e^{-iH_q^{rot}t/\hbar} = e^{-ig_z t\widetilde{|11\rangle}\widetilde{\langle 11|}}$$
$$= \begin{pmatrix} 1 & 0 & 0 & 0 \\ 0 & 1 & 0 & 0 \\ 0 & 0 & 1 & 0 \\ 0 & 0 & 0 & e^{-ig_z t} \end{pmatrix}. \quad (4.4.2)$$

This is a standard controlled-phase gate with the phase given by $-g_z t$. To realize a CZ gate, we can just let the system evolve for time $t = \frac{\pi}{g_z}$, in which case the evolution operator becomes

$$U_{\text{CZ}} = U\left(\frac{\pi}{g_z}\right) = \begin{pmatrix} 1 & 0 & 0 & 0 \\ 0 & 1 & 0 & 0 \\ 0 & 0 & 1 & 0 \\ 0 & 0 & 0 & -1 \end{pmatrix}. \quad (4.4.3)$$

The CZ gate time is given by $\frac{\pi}{g_z} = 53.8$ ns. We analyze the performance of this gate using quantum process tomography in section 4.7. We note that a similar CZ gate based on free evolution in the strong ZZ coupling regime, achieved via a tunable coupler, was recently demonstrated [112].

4.4.2 A generalized controlled-NOT gate based on the SWIPHT protocol

In addition to the free-evolution CZ gate, it is also possible to implement a CNOT gate in the strong ZZ coupling regime using a shaped microwave pulse. A protocol known as SWIPHT (speeding up wave forms by inducing phases to harmful transitions), provides a general framework for designing fast, high-fidelity two-qubit entangling gates [117, 118, 119]. The SWIPHT protocol is based on reverse-engineering analytical pulse shapes that implement two-qubit entangling gates [122]. SWIPHT was first demonstrated experimentally for a two-transmon system in the weak ZZ coupling regime [123]. The SWIPHT protocol was originally proposed for two transmon qubits coupled with a bus resonator, but it applies to any two-qubit system with ZZ coupling in the dressed qubit basis. Here, we employ SWIPHT to implement a generalized CNOT gate for our two-qubit system.

Fig. (4.3)(a) shows the energy levels in the computational subspace of the two-qubit system. A CNOT gate can be viewed as effectively swapping the $\widetilde{|00\rangle}$ and $\widetilde{|01\rangle}$ states while leaving the other logical states alone. A natural way to implement this is to apply a resonant microwave drive to perform a π rotation on the target transition $\widetilde{|00\rangle} \leftrightarrow \widetilde{|01\rangle}$. However, there exists a nearby harmful transition $\widetilde{|10\rangle} \leftrightarrow \widetilde{|11\rangle}$ [red in Fig. (4.3)(a)] that is detuned from the target transition by g_z, so it would be driven off-resonantly. As a result, one would have to make the gate time much longer than $2\pi/g_z$ to selectively drive the target transition. This is not optimal, given the limited coherence times of the qubits. Instead of attempting to avoid the harmful transition, the SWIPHT CNOT gate is designed to purposely drive it through a trivial cyclic evolution while driving a π rotation on the target transition. This is shown in Fig. (4.3)(b). A cyclic evolution on a two-level system can be described by a Z rotation, $e^{-i\varphi\sigma_z^{(2)}/2}$, where φ is the phase accumulated during the cyclic evolution. We can express the SWIPHT CNOT gate in the dressed two-qubit basis as

$$
\begin{aligned}
U_{\text{CNOT}} &= \widetilde{|0\rangle}\widetilde{\langle 0|} \otimes e^{-i\pi\sigma_x^{(2)}/2} + \widetilde{|1\rangle}\widetilde{\langle 1|} \otimes e^{-i\varphi\sigma_z^{(2)}/2} \\
&= \begin{pmatrix} 0 & -i & 0 & 0 \\ -i & 0 & 0 & 0 \\ 0 & 0 & e^{-i\frac{\varphi}{2}} & 0 \\ 0 & 0 & 0 & e^{i\frac{\varphi}{2}} \end{pmatrix}.
\end{aligned}
\tag{4.4.4}
$$

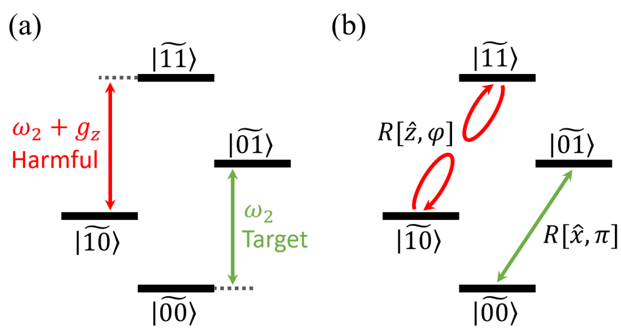

Figure 4.3: (a) The computational subspace of the two transmon qubit system with strong ZZ coupling. The frequency of the target transition (green) $\widetilde{|00\rangle} \leftrightarrow \widetilde{|01\rangle}$ is ω_2. The harmful transition (red) $\widetilde{|10\rangle} \leftrightarrow \widetilde{|11\rangle}$ is detuned from the target transition by g_z. (b) The SWIPHT pulse (see Fig. (4.4)) is on resonance with the target transition and induces a π rotation around the x-axis in the two-level target subspace. At the same time, the harmful transition is off-resonantly driven by the SWIPHT pulse and undergoes cyclic evolution, acquiring trivial phases.

Compared to a standard CNOT gate, the SWIPHT CNOT gate described above has some extra phases, which is why we refer to it as a generalized CNOT gate [117]. This generalized CNOT gate is maximally entangling and is related to the standard CNOT by single-qubit Z rotations and a global phase.

According to the SWIPHT protocol [117], analytical pulse shapes that implement the operation given in Eq. (4.4.4) can be generated from the formula

$$\Omega(t) = \frac{\ddot{\chi}}{\sqrt{\frac{g_z^2}{4} - \dot{\chi}^2}} - 2\sqrt{\frac{g_z^2}{4} - \dot{\chi}^2}\cot(2\chi). \tag{4.4.5}$$

Any real function $\chi(t)$ obeying the constraint $|\dot{\chi}| \leq g_z/2$ and the boundary conditions $\chi(0) = \chi(t_g) = \pi/4$, $\dot{\chi}(0) = \dot{\chi}(t_g) = 0$, where t_g is the gate time, produces a pulse wave form $\Omega(t)$ that performs a generalized CNOT. One may notice a factor of two difference from the original expression in Ref. [117]. This is due to different definitions of the Rabi strength. Here, we choose $\chi(t)$ as in Ref. [117]:

$$\chi(t) = A\left(\frac{t}{t_g}\right)^4\left(1 - \frac{t}{t_g}\right)^4 + \frac{\pi}{4}, \tag{4.4.6}$$

where A and t_g are given by

$$t_g = \frac{5.87}{g_z}, \quad A = 138.9. \tag{4.4.7}$$

Given $g_z = 9.29\,\text{MHz}$ the resulted gate time is $t_g = 100.6\,\text{ns}$. The pulse shape of the SWIPHT gate is plotted in Fig. (4.4). The performance of our CNOT gate is evaluated in section 4.6 and section 4.7 through quantum state and process tomography.

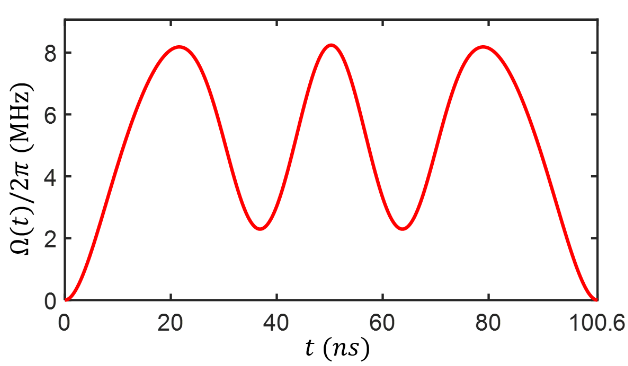

Figure 4.4: Pulse shape that implements the SWIPHT CNOT gate. The gate time is about 100.6 ns.

4.5 Randomized Benchmarking of the two-axis, single-qubit gate

To characterize the TAG, we perform the randomized benchmarking (RB) protocol described in Ref. [124] with assumption that errors are gate independent. The RB experiment starts with the qubit initialized in the ground state. Various $\pi/2$ gates and π gates are randomly chosen and concatenated together to form a sequence. A comparison of the measured result of these operations with what would be expected from an ideal system can then be used to evaluate performance.

The $\pi/2$ gates are Clifford group generators $e^{\pm i\sigma_u \pi/4}$, with $u = x, y$. The π gates are chosen from $e^{\pm i\sigma_b \pi/2}$ with $b = 0, x, y, z$, where we have defined σ_0 to be the identity operator. The RB sequence is truncated at different numbers of $\pi/2 - \pi$ gate pairs and applied to the qubit. Each truncation is followed by a $\pi/2$ or π gate to always bring the qubit to a certain eigenstate of σ_z. For convenience, we typically use the ground state in our experiments. Then, the probability of the ground state, alternatively referred to as the sequence fidelity, is measured for each truncation of the RB sequence. The above process is repeated for many different RB sequences. Finally, the sequence fidelity $\mathcal{F}$ is averaged over all of the sequences, thereby becoming a function of only the truncation, which is quantified by the number of $\pi/2$ gates. $\mathcal{F}$ decays exponentially, and the decay rate is determined by the average gate infidelity [124].

Since the TAG is designed to address two transitions for each qubit (one where the other qubit is in the ground state, and one where it is in the excited state), we run the RB experiment on each transition separately for each qubit. This measures the average fidelity of the TAG as it acts on the corresponding transition. For each RB experiment, we choose 5 random $\pi/2$ gate sequences and 8 random π gate sequences, yielding a total of 40 different RB sequences. Each sequence is truncated at every other pair of π and $\pi/2$ gates. For each truncation, 1000 copies are measured to obtain the sequence fidelity $\mathcal{F}$. The experimental results are plotted in Fig. (4.5) for all four transitions of the two qubits. The average gate fidelities of the TAG are 97.7(5)%, 99.1(1)%, 96.9(7)%, and 98.3(3)% for the transitions $\widetilde{|00\rangle} \leftrightarrow \widetilde{|10\rangle}$, $\widetilde{|01\rangle} \leftrightarrow \widetilde{|11\rangle}$, $\widetilde{|00\rangle} \leftrightarrow \widetilde{|01\rangle}$, and $\widetilde{|10\rangle} \leftrightarrow \widetilde{|11\rangle}$, respectively. Since each TAG has to be calibrated simultaneously for two transitions

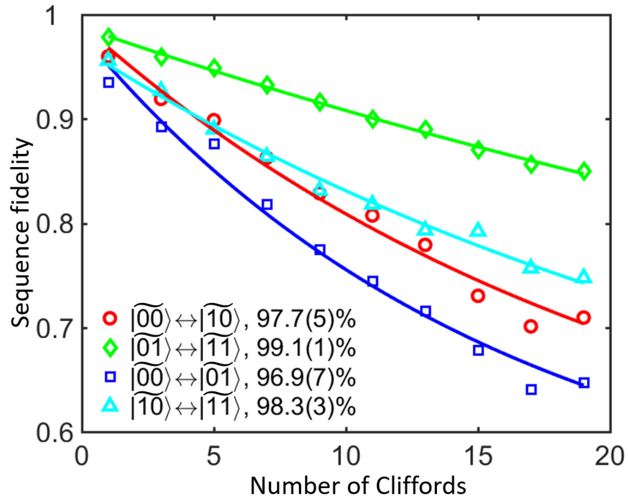

Figure 4.5: Randomized benchmarking of the two-axis, single-qubit gate. Average sequency fidelity vs. the number of Cliffords/$\frac{\pi}{2}$ gates for the transition $\widetilde{|00\rangle} \leftrightarrow \widetilde{|10\rangle}$ (red circle), $\widetilde{|01\rangle} \leftrightarrow \widetilde{|11\rangle}$ (green diamond), $\widetilde{|00\rangle} \leftrightarrow \widetilde{|01\rangle}$ (blue square), and $\widetilde{|10\rangle} \leftrightarrow \widetilde{|11\rangle}$ (cyan triangle). Solid curves are the exponential fittings to the data to extract an average gate fidelity for each transition.

of a qubit, we believe there are some coherence errors in the TAGs due to imperfect calibration. The gate fidelities of the two transitions of the second qubit are lower than those of the first qubit. This is consistent with the fact that T_2^* of the second qubit is only half that of the first qubit.

4.6 Quantum State Tomography of a Maximally Entangled State

The core functionality of two-qubit gates is to entangle two qubits. We first verify this functionality by preparing a maximally entangled state and performing quantum state tomography on it. Since the CNOT gate is more straightforward in terms of generating entangled states, we present experimental results of an entangled state generated with the SWIPHT CNOT gate.

As shown in Fig. (4.6)(a), the experiment starts from a $\pi/2$ rotation around the y-axis of the first qubit, which is the control qubit. This prepares the system in the state $\frac{1}{\sqrt{2}}(|0\rangle + |1\rangle)|0\rangle$. We then apply the SWIPHT CNOT gate, which brings the system to a maximally entangled state $|\psi\rangle = \frac{1}{\sqrt{2}}(e^{-i\frac{\varphi}{2}}|10\rangle - i|01\rangle)$. The extra phase $\varphi/2$ on $|10\rangle$ is due to the fact that the SWIPHT CNOT is a generalized CNOT gate. Finally, tomography rotations are applied, followed by projective measurements on both qubits. Each run consists of $N = 1000$ measurements in order to obtain

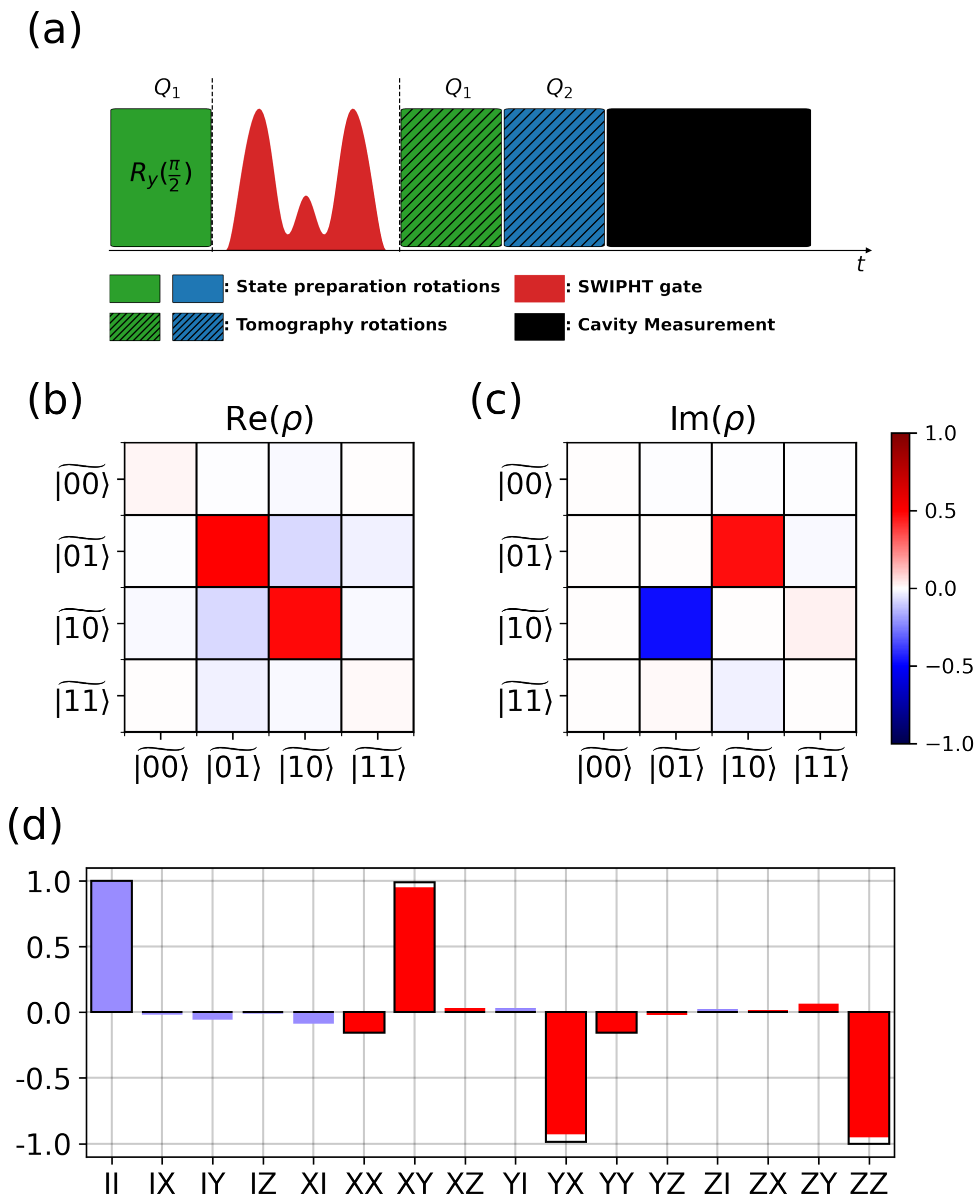

Figure 4.6: Results of quantum state tomography on a maximally entangled state prepared with the SWIPHT CNOT gate. (a) Pulse sequence for the quantum state tomography experiment (not to scale). (b) and (c) are the real and imaginary parts of the reconstructed density matrix. (d) The vector representation of the state in the Pauli basis. The light blue bars are the single-qubit components, and the red bars are the two-qubit components. The outlined bars represent the ideal entangled state $\frac{1}{\sqrt{2}}(e^{-i\frac{\varphi}{2}}\,|10\rangle - i\,|01\rangle)$. By comparing to the ideal entangled state, we obtained an experimental fidelity of 98.2%.

good statistics on the final state populations. Noise and imperfections during the experiment can lead to an unphysical density matrix. To remedy this, a maximum likelihood estimation is applied to search for a physical density matrix such that the predicted probability of obtaining the observed data with the physical density matrix is maximized [125]. In addition, a wide-band, quantum limited Josephson parametric amplifier was used that allowed us to read out both qubits at the same time.

The real and imaginary parts of the reconstructed density matrix are shown in Fig. (4.6)(b) and (c), respectively. As we can see, the largest contributions are all within the $|10\rangle$, $|01\rangle$ subspace, as expected. To compare to the ideal entangled state, the vector representation in the Pauli basis of the entangled state is shown in Fig. (4.6)(d). A fidelity of 98.2 % is obtained using $\mathcal{F} = \langle\rho|\psi\rangle$, where $|\psi\rangle$ and ρ are the ideal entangled state and the reconstructed density matrix from experiment, respectively.

4.7 Quantum Process Tomography of Two-Qubit Gates

Finally, we perform a full characterization of our two-qubit entangling gates using quantum process tomography. The process tomography starts from single-qubit rotations implemented with TAGs on both qubits to prepare the system. There are 36 different possible initial states for the two qubits: $\{|\pm x\rangle, |\pm y\rangle, |\pm z\rangle\}^{\otimes 2}$. A separate run for each initial state is conducted. In each run, a two-qubit entangling gate is applied after the initial state is prepared. For the SWIPHT CNOT gate, the gate time is about 100.6 ns. However, to remove a residual conditional phase due to the ZZ interaction, right after the SWIPHT gate we let the system idle (evolve freely) for a time such that the sum of the SWIPHT gate time and the idle time is equal to a full period of the ZZ interaction, $2\pi/g_z$. For the free-evolution CZ gate, no entangling microwave pulse is applied, and the system instead undergoes free evolution for 53.8 ns. Subsequently, tomography rotations and projective measurements are performed on both qubits. Each run consists of $N = 1000$ measurements in order to obtain good statistics on the final state populations. We apply a maximum likelihood estimation method to reconstruct the Pauli transfer matrix R for the process.

The experimental Pauli transfer matrices, $R^{\text{exp}}_{\text{CNOT}}$ for the SWIPHT CNOT gate and $R^{\text{exp}}_{\text{CZ}}$ for the free-evolution CZ gate, are shown in Fig. (4.8)(a) and (d), respectively. Fig. (4.8)(c) and

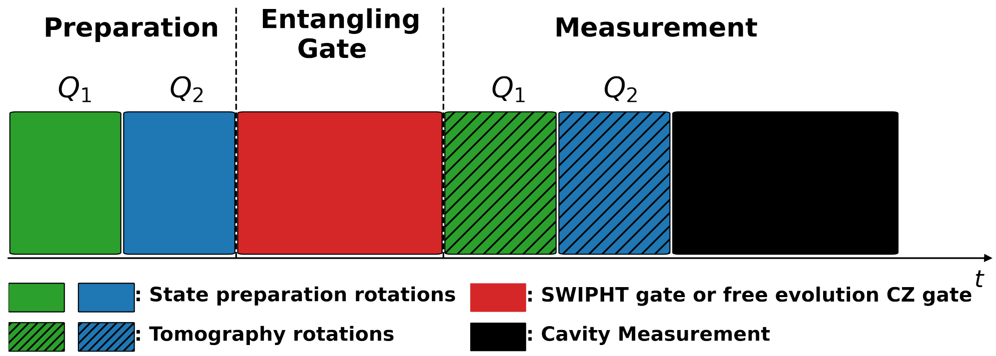

Figure 4.7: Pulse sequence for the quantum process tomography experiment (not to scale).

(f) illustrate the ideal R matrices, $R^{\text{ideal}}_{\text{CNOT}}$ and $R^{\text{ideal}}_{\text{CNOT}}$, for the SWIPHT CNOT and CZ gate, respectively. The average gate fidelity in each case is computed by comparing R^{exp} to R^{ideal},

$$\mathcal{F}_{\text{ave}} = \frac{\text{Tr}[(R^{\text{exp}})^T R^{\text{ideal}}]/4 + 1}{5}. \tag{4.7.1}$$

For the SWIPHT CNOT (CZ), we obtain an average gate fidelity of 94.6% (97.8%). To understand how much the decoherence contributes to the infidelity of the gates, we performed master equation simulations for both the SWIPHT CNOT and CZ gates with state preparation rotations also included, incorporating decoherence at levels consistent with our measured T_1 and T_2^* times. We then run the quantum process tomography on the simulated data to extract the simulated R matrices, shown in Fig. (4.8)(b) and (e) for the SWIPHT CNOT and CZ gates, respectively. The average gate fidelities from the master equation simulations are 98.92% for the SWIPHT CNOT gate and 99.25% for the CZ gate. In another simulation, perfect state preparation is assumed. The outcome gate fidelities are 99.4% for the SWIPHT CNOT gate and 99.7% for the CZ gate. This indicates that the SPAM errors [126] contributes about 0.5% to the infidelity.

The experiments report about 4% lower fidelities compared to the simulations. We attribute this difference to coherent errors [127] and leakage errors [113]. Note that our master equation simulation only includes the computational subspace and therefore does not capture leakage errors. Purity of the SWIPHT CNOT Pauli transfer matrix is measured to be 95.54%, which indicates the presence of leakage errors. Extra nonzero terms in Fig. (4.8)(a) and (d) compared to the

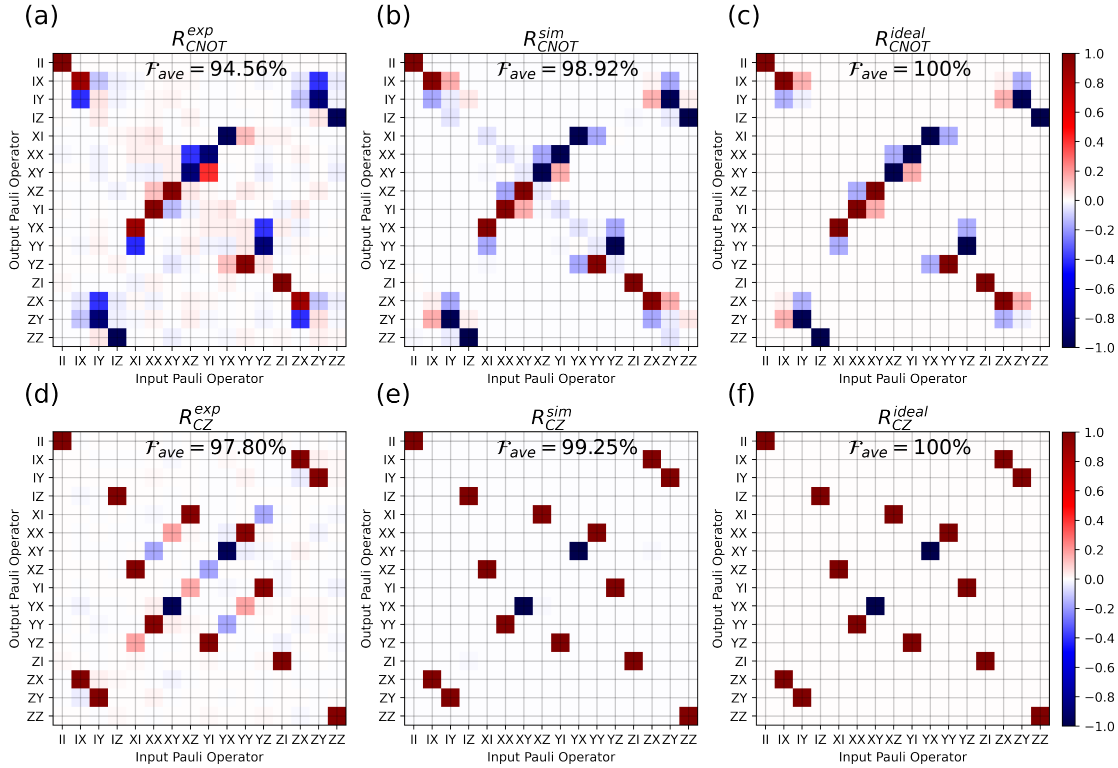

Figure 4.8: (a)-(c) [(d)-(f)] are the experimental, simulated, ideal Pauli transfer matrices for the SWIPHT CNOT gate [free evolution CZ gate]. Note that (e) and (f) are different although no significant difference can be noticed under this color scale.

simulation results in Fig. (4.8)(b) and (e) indicates that there are indeed coherent errors. On the other hand, the maximally entangled state in the quantum state tomography described in the last section reports a fidelity of 98.2%, which is close to the decoherence limit from the master equation simulation. This means that other states in the quantum process tomography would have fidelities lower than the average gate fidelity. The varying state fidelities of different states in the quantum process tomography also indicates that there are coherent errors in the experiment.

4.8 Summary

In this chapter, we experimentally demonstrated a universal quantum gate set for the regime of strong ZZ coupling between superconducting transmon qubits. We introduced the concept of two-axis gates to implement arbitrary single-qubit rotations in this regime, and we tested their performance in a two-qubit system using randomized benchmarking. The average gate fidelity was found to be about 99% for the first qubit and 98%for the second qubit. In addition, we demonstrated two types of two-qubit entangling gates: a SWIPHT CNOT gate implemented with a shaped microwave pulse and a CZ gate based on free evolution under the ZZ interaction. The SWIPHT CNOT was found to produce a maximally entangled state with a measured fidelity of 98.2% from quantum state tomography. We further characterized the performance of both the SWIPHT CNOT and the free-evolution CZ gates using quantum process tomography. We obtained average gate fidelities of 94.6% and 97.8% for the SWIPHT CNOT and the CZ, respectively. We presented evidence that the infidelities are likely due to coherent, SPAM, and leakage errors. Advanced pulse shaping techniques [95] and calibration improvements would likely reduce these errors significantly. The universal gate set demonstrated here offers additional control flexibility that can help to optimize the use of tunable couplers and to mitigate the adverse effects of residual ZZ interactions in superconducting qubit processors.

Chapter 5

Experiment: A dual-rail qubit with parametrically coupled transmons

5.1 Introduction

Quantum error correction (QEC) represents a foundational pillar in the pursuit of fault-tolerant quantum computing, enabling the suppression of logical error rates below practical thresholds through the synergistic integration of redundancy, error detection, and active correction protocols [38]. Over the past decade, significant strides have been made in reducing physical error rates across leading quantum platforms, including superconducting circuits [101], trapped ions [128], and photonic systems [129]. These advancements have brought surface code implementations and other topological QEC schemes closer to realizability [130]. Nevertheless, the stringent resource overheads associated with traditional QEC necessitate further suppression of physical error rates–particularly for measurement, single-qubit gates, and two-qubit entangling operations–to enhance the scalability of quantum processors and extend the utility of noisy intermediate-scale quantum (NISQ) devices [30].

A promising strategy to alleviate these challenges involves tailoring QEC protocols to exploit the intrinsic noise biases of specific physical systems. For instance, bosonic codes, such as the Kerr-cat qubit, leverage the nonlinear dynamics of superconducting cavities to bias errors toward detectable photon loss events, thereby relaxing the threshold requirements for fault tolerance [47, 131]. Similarly, the emerging paradigm of erasure qubits capitalizes on the asymmetry between amplitude damping (T_1) and dephasing (T_2) errors, which are ubiquitous in solid-state and atomic systems [132, 133]. By encoding logical qubits in subspaces where leakage out of the computational basis—termed erasure errors—dominates over stochastic Pauli errors, these protocols enable near-deterministic identification of error locations through syndrome extraction. This intrinsic detectability substantially elevates the tolerable physical error rates for QEC, as demonstrated theoretically in concatenated code architectures [134]. Recent experimental realizations in neutral atoms [135], superconducting cavities [136], and statically coupled transmons [137] have validated the feasibility of erasure conversion, highlighting its potential to streamline fault-tolerant quantum computing.

In this chapter, we demonstrate a superconducting erasure qubit encoded in a dual-rail manner within the single-excitation manifold of two parametrically coupled transmons. We show that single-photon loss errors of the transmons are converted to detectable erasure errors and can be corrected with high fidelity. We also show that with careful engineering of device parameters, coherence of the dual-rail qubit can largely surpass the underlying physical qubits. Finally, we demonstrate continuous mid-circuit erasure detection during dual-rail qubit operations by doing parity readout, and show that this detection ability can further prolong the dual-rail qubit life time.

5.2 Device

Our device consists of two transmons and one common readout cavity as shown in Fig. (5.1). The transmons are coupled through a two-junction SQUID. The readout cavity allows for joint readout of the transmon states. The dc-SQUID loop serves as the only tuning element on the chip. By varying the flux through the SQUID, we can tune the frequencies of both transmons as well as the cavity simultaneously.

The sample was fabricated by Dr. Katarina Cicak at NIST Boulder Microfabrication Facility on 76 mm sapphire wafers. 100 nm-thick sputtered niobium film served as the main wiring layer, patterned by a fluorine-based reactive ion dry gas etch. Josephson junctions were then formed using the established Dolan bridge technique, involving a double-angle ($\pm 14.3^\circ$) aluminum evaporation onto a bi-layer resist stack of MMA/PMMA (550 nm/240 nm). Between the two aluminum depositions, the first layer (35 nm) was oxidized at 100 mTorr for 300 seconds to create the tunnel barrier, followed by deposition of the second aluminum layer (75 nm). This overlap defined the Josephson junctions, where qubit junctions were approximately 100 nm × 120 nm and SQUID junctions were about 1.8 μm × 0.1 μm. All depositions were carried out in a custom chamber equipped with a load-lock and computer-controlled oxidation to ensure consistent junction current densities. To electrically connect the Josephson junctions to the niobium wiring, an aluminum patch layer was e-beam evaporated in the same chamber and then lifted off. Before this final aluminum deposition, an ion mill cleaning step (beam = 300 V, accelerator = 950 V, filament = 3.47 A) for 30 seconds was performed to ensure a robust, superconducting interface between the various metal layers.

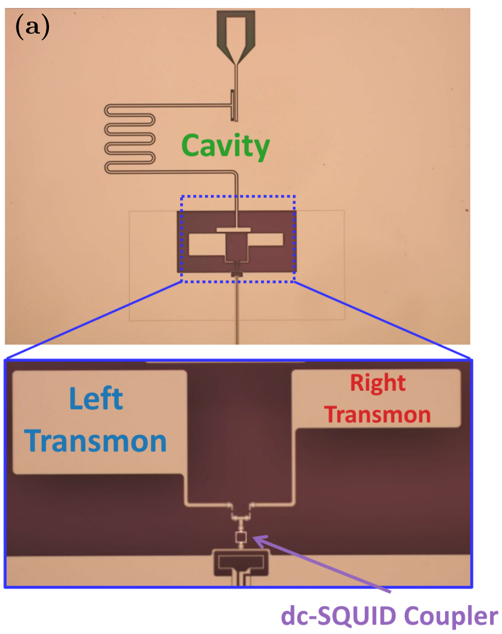

Figure 5.1: A flux and parametrically tunable two-qubit system. (a) Optical micrograph of the two-qubit system. (b) Circuit diagram of the device. The two transmons, Q1 (blue) and Q2 (red), are joined by a DC SQUID (black) and can be jointly readout through the cavity (green). The stray capacitance between the transmons (orange) gives rise to capacitive (negative linear transverse) coupling and is canceled by the inductive (positive linear transverse) coupling from the shared currents in the DC SQUID at a particular "cancellation" flux. Residual (nonlinear) inter-transmon ZZ coupling can be further suppressed to near zero by parametrically modulating the SQUID off-resonant from the difference frequency of the two transmons.

The dual-rail qubit is defined in the single-excitation manifold of the two-transmon computational space, where $|0_L\rangle = |10\rangle$ and $|1_L\rangle = |01\rangle$. With this encoding scheme, bit-flip errors of the underlying transmons caused by single-photon loss or excitation are converted to detectable erasure errors of the dual-rail qubit.

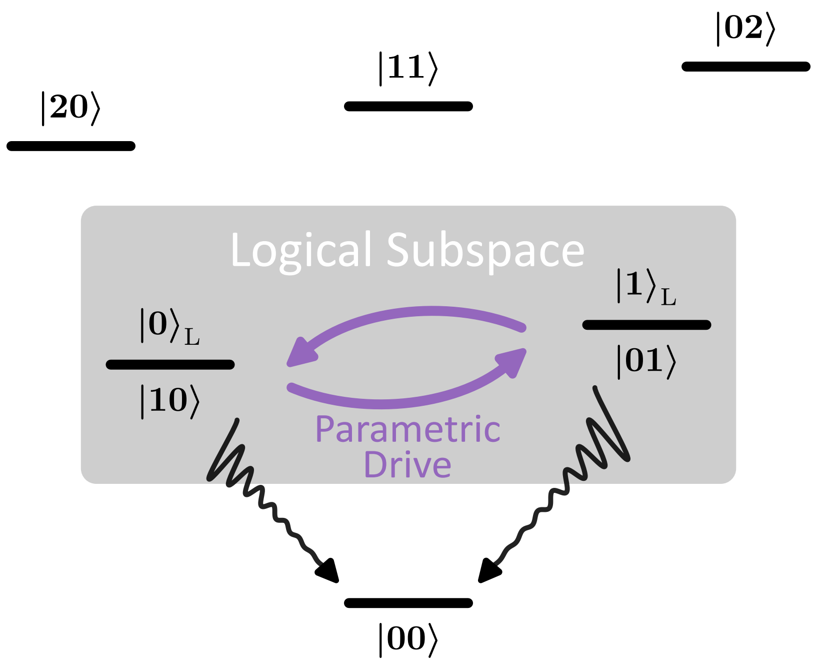

Figure 5.2: Energy levels of the two-transmon system. Logical ground and excited states are encoded in the single-excitation manifold. The dual-rail qubit transition can be driven by modulating the SQUID parametrically at the difference frequency $\omega_{|10\rangle} - \omega_{|01\rangle}$.

The design of our device provides the dual-rail qubit with additional protection against dephasing. The dual-rail qubit transition frequency ω_L is determined by the transmon frequency difference $\omega_L = \omega_{|01\rangle} - \omega_{|10\rangle}$. As can be seen from Fig. (5.3), even though the transmons are susceptible to flux noise when a nonzero static flux bias is applied to the SQUID, there exists a sweet spot at $\phi_s = \Phi_s/\Phi_0 \approx 0.39$ where $\mathrm{d}\omega_1/\mathrm{d}\Phi \approx \mathrm{d}\omega_2/\mathrm{d}\Phi$. At this sweet spot, the first derivative of the dual-rail qubit frequency $\mathrm{d}\omega_L/\mathrm{d}\Phi$ approaches zero, which means that the dual-rail qubit is insensitive to flux noise up to first order. The transmon frequencies and coherence times at this sweet spot are shown in table 5.1. Another major source of dephasing, cavity photon noise, can be mitigated as well. Since both transmons are dispersively coupled to the common readout cavity, thermal photons within the cavity will dephase the transmons simultaneously at the rate [138]

$$\Gamma_i = \frac{8\bar{n}\kappa\chi_i^2}{\kappa^2 + 4\chi_i^2}, \tag{5.2.1}$$

where $2\chi_1$ ($2\chi_2$) is the dispersive shift of Q1 (Q2), $\bar{n}$ is the average number of intra-cavity photons and κ is the cavity decay rate. The dephasing rate of the dual-rail qubit is expected to depend on the difference of the dispersive shifts, $\Delta\chi = \chi_2 - \chi_1$, such that

$$\Gamma_L = \frac{8\bar{n}\kappa\Delta\chi^2}{\kappa^2 + 4\Delta\chi^2}. \tag{5.2.2}$$

In an ideal case where $\chi_1 = \chi_2$, the dual-rail qubit will not be dephased by intra-cavity photons at all. We note that a device geometry similar to ours is proposed in Ref. [132] where protection against measurement and thermal cavity photons is also discussed at length. With our current device, we achieved $\Delta\chi = 0.093(14)$ MHz which is two orders of magnitude smaller than χ_1 and χ_2.

	Transmon 1	Transmon 2
f(GHz)	5.069	5.533
T_1(μs)	18.2(6)	9.9(2)
T_2^*(μs)	2.45(9)	2.35(9)

Table 5.1: Frequencies and coherence times of the transmons at the flux sweep spot.

To readout the dual-rail qubit, we carry out a parity readout at the end of dual-rail qubit operations. The frequency of the readout drive is chosen such that the zero-, single- and double-excitation states of the two-transmon system can be resolved. To calibrate the readout drive, we first measure the cavity spectrum after initializing the transmons in different states. The cavity spectroscopic curves corresponding to four initial states are shown in Fig. (5.4(a)). The optimal readout frequency $\omega_{\mathrm{RO}}/2\pi = 8.7148$ GHz is close to the cavity frequency when the transmons are in $|10\rangle$ or $|01\rangle$ state. Integrated signals of single-shot measurement outcomes fall into one of three Gaussian distributions in the IQ plane depending on the number of excitations (Fig. (5.4(b))). To resolve the dual-rail qubit states which are both single-excitation states, we apply a π pulse to Q1 before readout to map $|0_L\rangle$ and $|1_L\rangle$ to $|00\rangle$ and $|11\rangle$ respectively, which are well separated in the

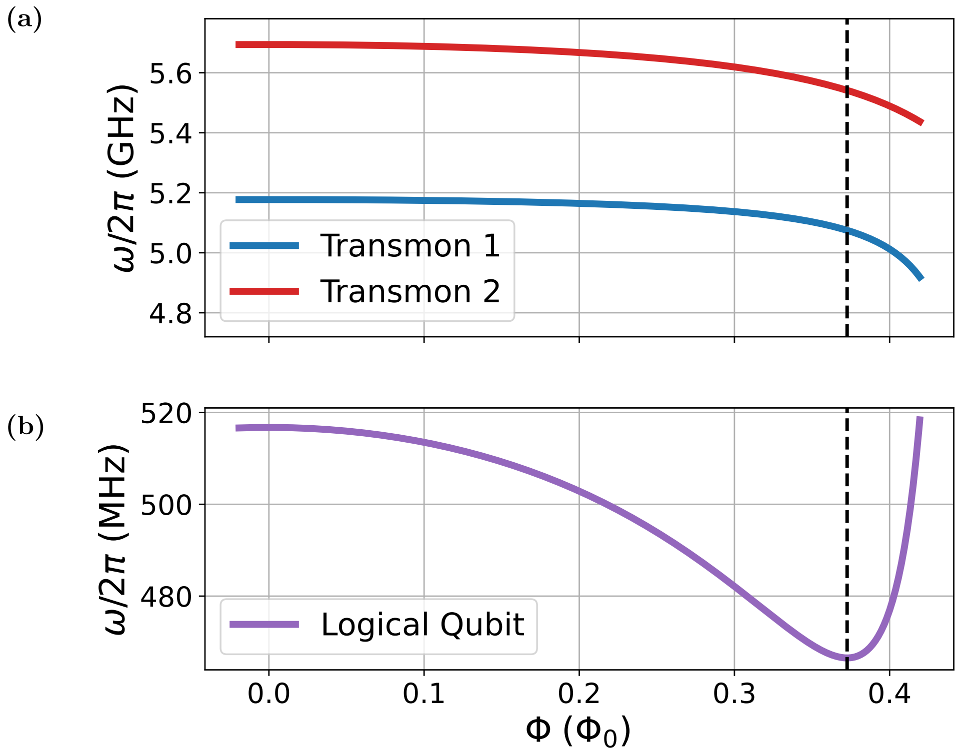

Figure 5.3: Frequency modulation curves of (a) the transmons, and (b) the dual-rail logical qubit. The dashed line is where we operate the logical qubit to gain protection against flux noise.

IQ plane for classification. The π pulse also maps the shots where the system is not in the dual-rail space anymore by the time of final readout (i.e. erasure errors have happened) to the distribution corresponding to single-excitation states. Then we can assign the number of shots in each bin to $|0_L\rangle$, $|1_L\rangle$ and erasure respectively. By leaving out the erasure shots, we can postselect against such erasure errors. The logical outcome populations are defined as $P_{1_L(0_L)} = N_{1_L(0_L)}/(N_{1_L} + N_{0_L})$ where N is the number of shots of the assigned logical state.

Single-qubit gates within the dual-rail space is implemented with a beamsplitter interaction induced by modulating the SQUID parametrically with a microwave drive at frequency $\omega_L/2\pi = (\omega_{|10\rangle} - \omega_{|01\rangle}) = 464.43\,\text{MHz}$. The phase of this parametric drive (PD) defines the rotating axis. The waveform of the PD is directly synthesized with a high-speed AWG at room temperature. This gives us a great flexibility to implement arbitrary single-qubit gates with high fidelity. We then use

(a)

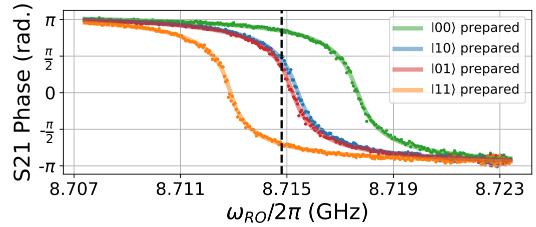

(b)

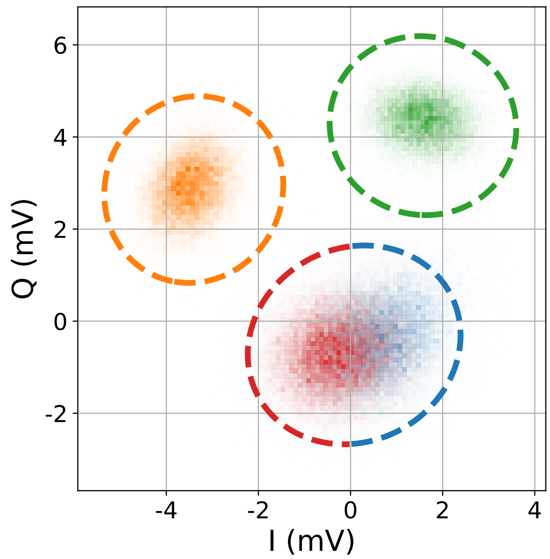

Figure 5.4: (a) Cavity spectrum of the two-transmon system initialized in different states. The dashed line at 8.7148 GHz is the optimal frequency for the final readout. (b) Histogram of single-shot measurement outcomes in the IQ plane. States with zero-excitation ($|00\rangle$ in green), single-excitation ($|10\rangle$ in blue and $|01\rangle$ in red) and double-excitation ($|11\rangle$ in orange) each form a Gaussian distribution.

dual-rail qubit Rabi oscillations to tune up single-qubit π and $\pi/2$ gates. An example pulse diagram of one such experiment is shown in Fig. (5.5(a)). By sweeping the frequency of the parametric drive, we can observe a "Chevron"-like interference pattern (Fig. (5.5(b))) that allows us to determine ω_L more accurately at the center of this symmetric pattern. The single-qubit gates in this work are calibrated to be 30 ns long while faster gates are feasible by increasing the amplitude of the PD. We then perform Clifford randomized benchmarking [139] to characterize gate fidelity of the single-qubit gates. We measure an error-per-Clifford of 0.0053(5) shown in Fig. (5.5(d)).

A major source of logical single-qubit errors is bit-flip error within the dual-rail space caused by double-photon events, where the two-qubit state leaves and then re-enters the dual-rail subspace via a combination of one relaxation event and one thermal excitation event, in either order. This erasure error can decohere the dual-rail qubit as a bit flip, if it re-enters the other logical state or as a phase flip if it re-enters the same logical state. Postselection using the final readout result at the end of the logical operation is not sufficient to eliminate these errors. To migitate such errors, we can perform continuous mid-circuit erasure detection during the logical operation so that the occurrence of an erasure event can be detected, and thus excluded, before a second reentry event happens.

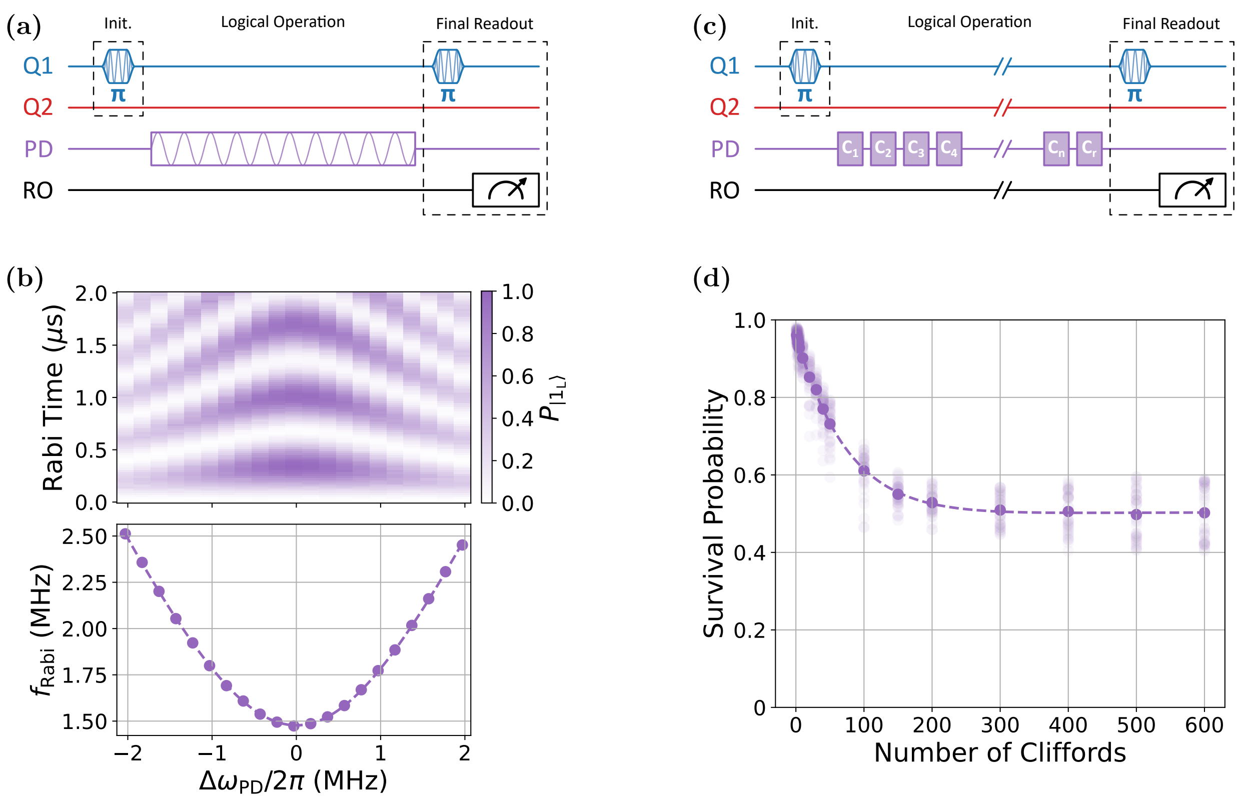

Figure 5.5: (a) Pulse diagram of a dual-rail qubit Rabi oscillation experiment. After preparing $|0_L\rangle$ with a 50 ns microwave pulse on Q1, transition $|0_L\rangle \leftrightarrow |1_L\rangle$ is driven by the parametric drive. The parametric drive frequency is swept to observe the "Chevron"-like interference pattern in (b). (c) Pulse diagram of a Clifford randomized benchmarking experiment. Clifford gates are applied to the dual-rail qubit followed by a final readout. The randomized benchmarking data is shown in (d). At each Clifford depth we generate 40 random sequences, the outcomes of which are plotted in light purple. The average survival probability is fitted to an exponential decay.

5.3 Mid-circuit Erasure Detection

Double-photon errors caused by transmon heating limit the coherence improvement we can achieve through erasure detection [137](e.g., if there were no heating events, then all decay events would occur only once and could be detected at any time as an erasure). We leverage the common readout cavity in our device to carry out continuous erasure detection during logical operations to mitigate the impact of these errors. As previously discussed, we engineer the couplings between the cavity and both transmons to minimize dephasing induced by intra-cavity photons. This allows us to probe the readout cavity during logical operations, while minimizing excess logical qubit phase errors from photon shot noise in the readout cavity.

In the experimental protocol shown in Fig. (5.6(a)), we turn on the mid-circuit detection (MCD) tone after dual-rail qubit state initialization and start acquiring the digitized signal which will be divided into segments with a 560 ns integration window. Due to the non-zero residual $\Delta\chi$, we have to blue-shift the MCD tone by $\sim 2\,\text{MHz}$ from ω_{RO} to avoid significant dephasing of the logical qubit state. As a result, the mid-circuit detection is only sensitive to energy decay events to the two-qubit state $|00\rangle$ and not thermal excitation events to the $|11\rangle$ state. These are the majority of erasure events that occur during logical operations. These results are shown in Fig. (5.6(b)). A linear boundary can be drawn between the two distributions that allows us to distinguish if a decay erasure event has happened or not with a readout fidelity for erasure detection of 95.21 %. The MCD tone is turned off for 560 ns before the final readout in order to allow the readout cavity to fully relax before being driven at ω_{RO}.

By monitoring the MCD signal in time, we can identify decay erasures during a single shot and then choose to exclude this data in postselection. Fig. (5.7) shows an example dataset of 50 measurement traces detected over the course of $t = 44.8\,\mu\text{s}$. With the information extracted with MCD, we can mark the traces where the logical qubit appears to remain in the logical subspace during operations and only calculate logical qubit statistics based on the final readout outcomes of those data.

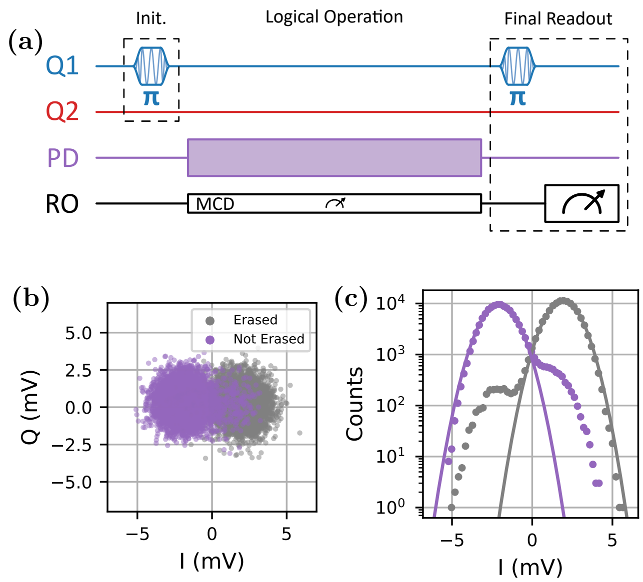

Figure 5.6: (a) Pulse diagram of carrying out the MCD during the logical operation. The acquired MCD signal can be divided into shorter segments each containing 560 ns of erasure detection information for being within the logical subspace or in state $|00\rangle$ (here the shift of the MCD cavity readout frequency prevents detection of $|11\rangle$ events). (b) Integrated signal of the MCD on the IQ plane. Each point corresponds to a 560 ns segment. (c) Experimentally measured histogram of the integrated MCD quadrature signal.

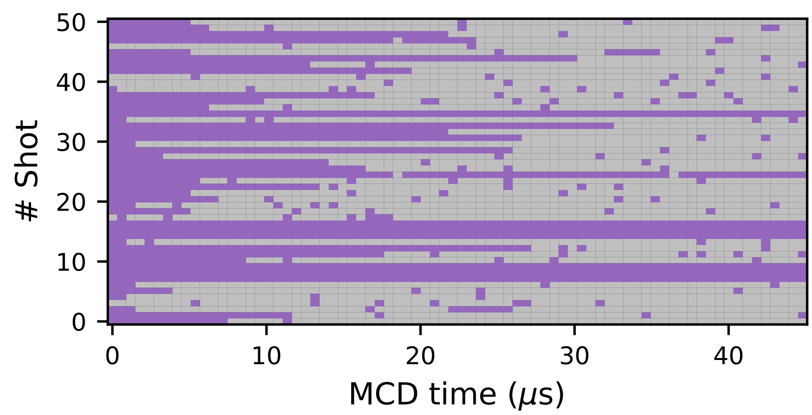

Figure 5.7: MCD signal of 50 measurement runs from $t = 0$ to $t = 44.8\,\mu$s. Each horizontal line represents a single-shot measurement run evolving in time. Following one shot from left to right, change in color indicates leaving or entering the logical space. Note that the time duration of each pixel is much shorter than the transmon coherence times, so we can view the isolated purple pixel events as most likely due to classification infidelity. The single-shots free from decay erasure events are those that remain solid purple throughout the entire duration of the MCD.

We measure the logical qubit bit-flip rate first without MCD where we prepare either $|0_L\rangle$ or $|1_L\rangle$ and readout the final state after a varying length of delay. An exponential increase in the erasure outcomes can be observed in Fig. (5.8) as expected. At longer delay times, this large fraction of erasure counts intervenes with the logical state outcomes due to error in assigning the counts. Results of two simulation are also shown in Fig. (5.8) as solid and dash lines. For the solid lines, we modeled the full system with the Lindbladian master equation

$$\dot{\rho} = -i[\hat{\mathcal{H}}, \rho] + \Gamma_{\downarrow}^{1}\mathcal{D}[\hat{\sigma}^{-} \otimes I]\rho + \Gamma_{\downarrow}^{2}\mathcal{D}[I \otimes \hat{\sigma}^{-}]\rho + \Gamma_{\uparrow}^{1}\mathcal{D}[\hat{\sigma}^{+} \otimes I]\rho + \Gamma_{\uparrow}^{2}\mathcal{D}[I \otimes \hat{\sigma}^{+}]\rho, \tag{5.3.1}$$

where $\Gamma_{\downarrow}^{1}$ and $\Gamma_{\downarrow}^{2}$ are relaxation rates of the transmons shown in table 5.1 and the thermal excitation rates $\Gamma_{\uparrow}^{1(2)} = \Gamma_{\downarrow}^{1(2)} \times \exp(-\hbar\omega_{1(2)}/k_B T)$ with the effective temperature of qubits independently measured to be 45 mK. Logical state assigning errors are also taken into account in the simulation by postprocessing the simulation outcome with the readout infidelities measured independently. For the dash line we remove double-photon errors by setting the transmon-heating rates to zero. The simulations indicate that both assigning error and double-photon error contribute to logical qubit bit-flip in our system.

We then turn on the mid-circuit detection during the delay to check for erasures only seen during the final outcome in the measurements described above. We again prepare either $|0_L\rangle$ or $|1_L\rangle$ before the MCD tone and calculate P_{0_L} or P_{1_L} based on only the outcomes that survive the entire MCD period during the delay. The relaxation curve in Fig. (5.9(b)) appears to take a non-exponential form. This is possibly caused by the fact that the MCD is only sensitive to erasures which bring the logical qubit to $|00\rangle$. We are not able to check and correct erasures caused by thermal excitations with MCD in the current setup. Another possible cause of the non-exponential form is that assigning error accounts for different weights at different delay times. At longer delay times, assigning error plays a critical role since the number of surviving shots becomes much smaller compared to the erasure outcomes. If fitted to a linear model $\Delta P = 1 - t/T_1$, data shown in Fig. (5.9(b)) yields a logical qubit $T_1 = 91(3)\,\mu$s which is longer than the average T_1 of both transmons ($14\,\mu$s) by a factor of 6.5.

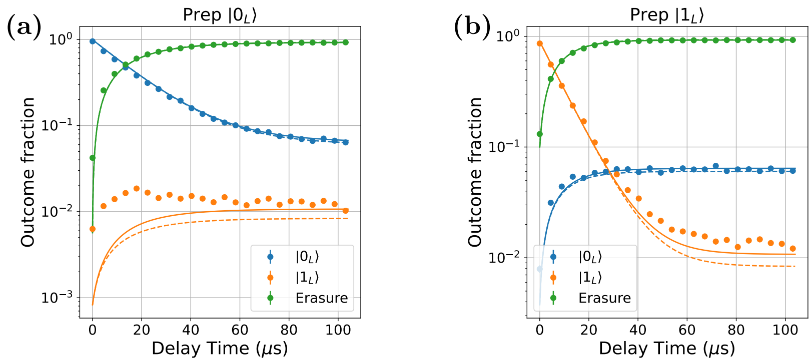

Figure 5.8: Dual-rail bit-flip error measurement. The physical state outcomes, assigned based on measurement, are plotted as a function of delay for the dual-rail qubit prepared in (a) $|0_L\rangle$ and (b) $|1_L\rangle$. The plots display the fractions corresponding to three possible outcomes, with each state preparation repeated 20 000 times. The solid line represents a simulation that uses the experimentally measured parameters including T_1 and effective temperature of the transmons, while the dashed line shows a simulation with double-photon errors removed by setting the transmon-heating rates to zero. The close match between the solid and dashed lines indicates that transmon heating is not the primary source of error, and the strong agreement between both simulation curves and the experimental data confirms our overall understanding of the error mechanisms at play. All error bars represent $\pm 1\sigma$ standard error.

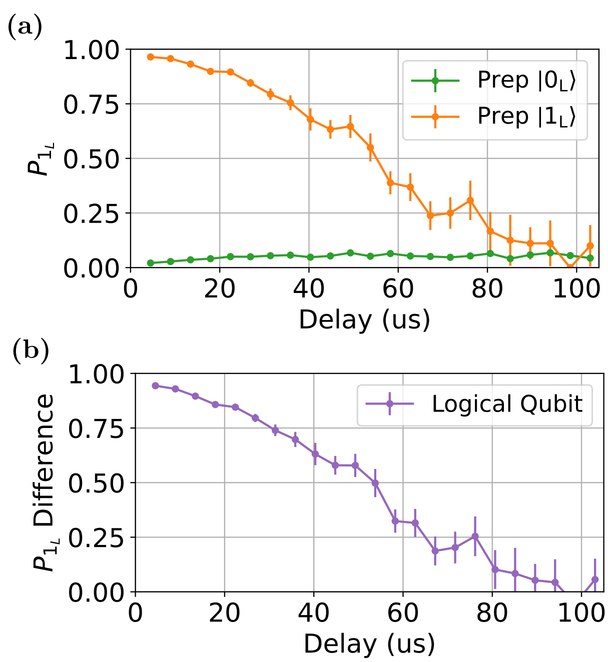

Figure 5.9: (a) $|1_L\rangle$ population as a function of delay time when preparing either $|0_L\rangle$ or $|1_L\rangle$. Each state preparation repeated 80 000 times with a small fraction surviving postselection.. (b) The difference between the two curves in (a) is used to define the relaxation time of the logical qubit.

We can also perform a logical Ramsey experiment with MCD as shown in Fig. (5.10). We expect the measured $T_2^* = 11(2)\,\mu$s to be largely limited by the residual $\Delta\chi$ and photons in the readout cavity when we have the mid-circuit detection tone on. Yet we still observe a factor of 4.7 improvement compared to the transmons' $\bar{T}_2^* = 2.4\,\mu$s.

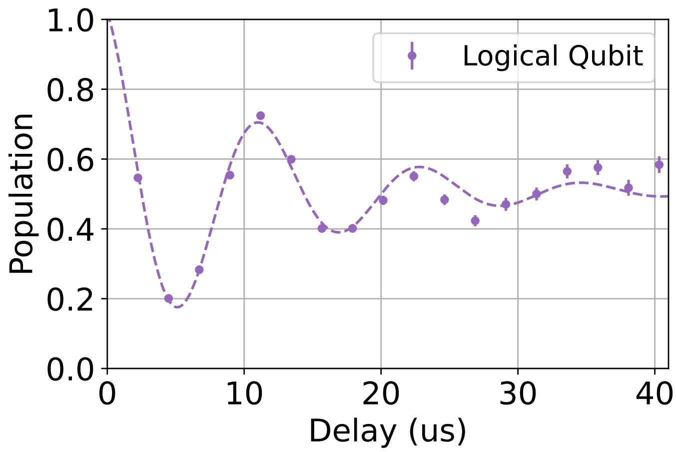

Figure 5.10: Ramsey T_2^* fringe of the dual-rail qubit with MCD.

5.4 Summary

In this chapter, we presented an experimental demonstration of a superconducting erasure logical qubit encoded in a dual-rail two-qubit subspace using two parametrically coupled transmons. By encoding the logical states in the single-excitation manifold–where $|0_L\rangle = |10\rangle$ and $|1_L\rangle = |01\rangle$–our approach converts common single-photon loss errors into detectable erasure events. This conversion, in conjunction with tailored device design and parameter engineering, leads to a significant suppression of both dephasing and bit-flip errors. The device consists of two transmons coupled via a two-junction SQUID and jointly read out through a common cavity. The SQUID not only enables parametric modulation for qubit control but also allows tuning of the transmon frequencies to a flux sweet spot, minimizing first-order sensitivity to flux noise. Moreover, by engineering the dispersive shifts ($\chi_1 \approx \chi_2$), the dual-rail qubit becomes largely immune to dephasing from cavity photon noise, as the dephasing rate depends on their difference $\Delta\chi$.

Single-qubit gates are implemented via a beamsplitter interaction induced by a parametric drive, with gate durations of around 30 ns. High-fidelity operations are confirmed through randomized benchmarking, which yielded an error-per-Clifford of approximately 0.0053. Additionally, the dual-rail encoding offers inherent protection, as evidenced by a measured logical relaxation time (T_1) of about 91 μs–roughly 6.5 times longer than the individual transmon T_1 times–and an improvement in Ramsey T_2^* compared to the underlying transmons.

A key innovation in our work is the implementation of continuous mid-circuit erasure detection. By probing the readout cavity with a readout tone shifted to higher frequency than the final readout during logical operations, we can effectively detect when the qubit leaves the computational subspace (specifically when the transmons decay to $|00\rangle$). This real-time monitoring enables postselection of valid logical qubit operations and helps mitigate errors due to double-photon events arising from transmon heating.

Overall, our experimental results validate the dual-rail qubit architecture as a promising route toward error mitigation by converting energy decay error events to logical qubit erasures. The combination of erasure conversion and mid-circuit detection not only extends the coherence of the logical qubit beyond that of the constituent transmons but also offers a possible path to reduce the overhead in coping with decay errors so that full error correction schemes can be implemented more effectively for fault-tolerant quantum computing.

Chapter 6

Experiment: Merged-element Transmon

This chapter presents a comprehensive investigation into merged-element transmon (MET) architectures, aimed at overcoming the scalability and loss challenges inherent to traditional superconducting qubits. In the first study, we introduce the "MET" concept by replacing the large external shunt capacitor with the intrinsic capacitance of a Josephson junction. This approach achieves nearly a 100-fold reduction in device footprint while demonstrating robust qubit operations through state-dependent resonator shifts and multi-photon transitions. A detailed participation-ratio analysis identifies the amorphous-Si tunnel barrier as the primary loss channel, setting the stage for the necessity of low-loss barrier such as crystalline materials with fewer defects.

Building on this foundation, the second work proposes the FinMET device–a MET based on silicon fins. By exploiting the anisotropic etching properties of Si substrates, FinMET enables the formation of atomically flat, high-aspect-ratio tunnel barriers with an epitaxial capacitor. This architecture promises a significant reduction in dielectric losses and two-level system defects, paving the way for scalable fabrication using mature silicon processing technologies.

In the third contribution, we demonstrate the performance of superconducting parallel plate capacitors constructed from crystalline Si fins. Integrated into lumped element resonators and transmon circuits, these capacitors exhibit state-of-the-art internal quality factors and qubit relaxation times, underscoring the viability of Si-fin technology for achieving compact, low-loss superconducting components.

Collectively, these studies chart a promising route toward high-density, high-coherence quantum circuits by merging innovative device architectures with advanced materials engineering.

The content of this chapter is based on the following work:

- Ruichen Zhao et al. "Merged-Element Transmon". In: **Physical Review Applied** 14.6 (Dec. 2020), p. 064006. DOI: 10.1103/PhysRevApplied.14.064006
- Aranya Goswami et al. "Towards Merged-Element Transmons Using Silicon Fins: The FinMET". in: **Applied Physics Letters** 121.6 (Aug. 2022), p. 064001. ISSN: 0003-6951. DOI: 10.1063/5.0104950
- Anthony P. McFadden et al. "Fabrication and Characterization of Low-Loss Al/Si/Al Parallel Plate Capacitors for Superconducting Quantum Information Applications". In: **npj Quantum Information** 11.1 (Jan. 2025), pp. 1–6. ISSN: 2056-6387. DOI: 10.1038/s41534-025-00967-5

6.1 Introduction

The invention of the transmon qubit has spurred rapid progress in quantum-information research over the past decade, enabling landmark demonstrations such as mid-flight detection and reversal of quantum jumps [141] and the pursuit of quantum supremacy [31]. At the heart of the transmon architecture lies a Josephson junction (JJ) providing a nonlinear inductance (L_J) shunted by a capacitor (C) that defines the charging energy ($E_C = e^2/(2C)$) and the Josephson energy ($E_J = I_c\Phi_0/(2\pi)$). By engineering the ratio E_J/E_C, transmons can suppress charge dispersion while maintaining sufficient anharmonicity, a balance that renders them relatively robust against charge noise [28]. Nonetheless, conventional transmon designs face significant challenges, notably due to energy relaxation arising from parasitic two-level systems (TLSs) at surfaces and interfaces [87] and the inherent limitations in scaling imposed by large planar shunt capacitors.

A common thread in the works presented in this chapter is the exploration of merged-element transmon (MET) architectures as a pathway to overcome these challenges. By integrating the JJ and its shunting capacitor into a single element—constructed from a superconductor–tunnel-barrier–superconductor trilayer–the MET approach offers several advantages over conventional designs. First, it dramatically reduces the device footprint (by factors ranging from 10^2 to 10^4), thereby alleviating issues related to unwanted radiation, interqubit coupling, and stray field interactions that can arise in densely integrated systems. Second, the merged configuration provides a natural cancellation between the capacitive and inductive contributions to the qubit frequency, leading to enhanced robustness against lithographic variations and improved frequency precision. Third, by enabling the use of low-barrier-height materials for the tunnel barrier, the MET architecture permits the fabrication of thicker barriers with reduced sensitivity to atomic-scale thickness variations and defect-induced TLS losses.

An innovative extension of the MET concept is embodied in the FinMET device, which leverages silicon fin technology to further enhance scalability and device performance [142, 143]. By exploiting the anisotropic wet etching of Si(110) substrates, atomically flat Si(111) sidewalls are achieved, which serve both as high-aspect-ratio tunnel barriers and as low-loss parallel-plate capacitor (PPC) elements. These PPCs, with their compact form factor and confined electric field energy, may offer substantial improvements in coherence times when integrated into superconducting circuits. The FinMET design not only facilitates tighter control over barrier thickness and junction uniformity but also minimizes participation of lossy interfaces, thereby addressing key limitations encountered in conventional Al/AlOx/Al junctions and planar capacitor geometries.

Collectively, these studies converge on the common objective of enhancing superconducting qubit performance through innovative materials engineering and device architecture. By merging the traditionally separate roles of the JJ and shunt capacitor, and by employing advanced fabrication techniques such as epitaxial growth and anisotropic silicon etching, the merged-element and FinMET approaches promise to reduce device dimensions, mitigate deleterious TLS losses, and ultimately enable large-scale, high-coherence quantum circuits. This chapter synthesizes these advancements, laying the groundwork for next-generation quantum information processors that combine scalability with robust quantum coherence.

6.2 Nb/a-Si/Nb Trilayer MET

We first present a proof-of-principle demonstration of a MET that integrates the shunt capacitor and Josephson junction into a single device constructed from a sputtered niobium–amorphous Si–niobium (Nb/a-Si/Nb) trilayer [144]. The device fabrication was carried out by Dr. Ruichen Zhao at NIST Boulder Microfabrication Facility and begins with the deposition of the Nb/a-Si/Nb trilayer onto a high-resistivity intrinsic silicon substrate that has been pre-treated with hydrofluoric acid to remove native oxides and contaminants. The trilayer is patterned using optical lithography followed by a fluorine-based dry etch, forming the device structure with an barrier thickness of approximately 9 nm. Two interdigitated capacitors, designed to couple the MET to the surrounding circuitry, are realized in the same process. A Nb air bridge, isolated by a SiO_x spacer, is subsequently deposited and patterned to connect the top electrode to the interdigitated capacitors; a final dip in hydrofluoric acid removes the SiO_x, ensuring a clean metal interface and minimizing parasitic dielectric contributions. Fig. (6.1) shows a scanning electron micrograph and an illustrative picture of the cross section of the device.

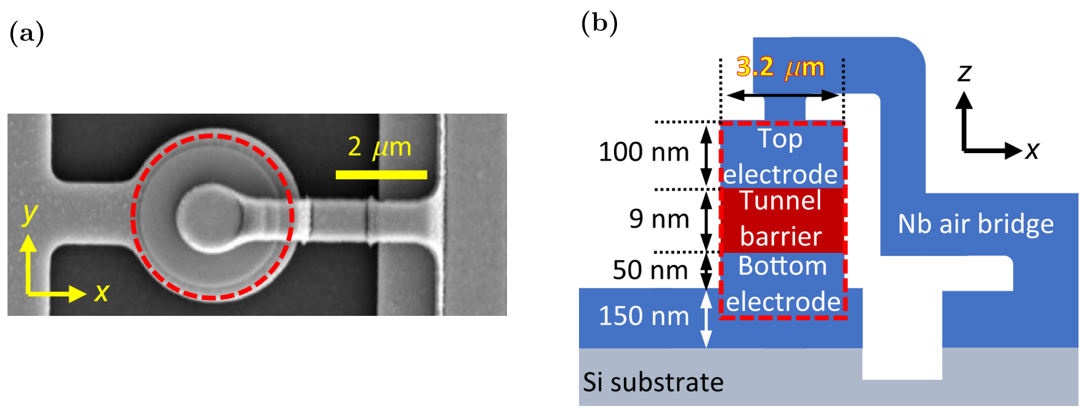

Figure 6.1: (a) Scanning electron micrograph and (b) illustrative cross-section diagram of the Nb/a-Si/Nb trilayer MET. Figure adapted from [140].

The microchip is mounted in a cryogen-free dilution refrigerator operating at temperatures around 10 mK. Microwave tones are introduced through heavily attenuated input lines to minimize thermal noise, and a vector network analyzer (VNA) is used to probe the system. In this configuration, a half-wavelength readout resonator is capacitively coupled to the MET, enabling dispersive readout of the qubit state. The resonator, with a bare frequency of approximately 6.876 GHz, exhibits a qubit-state-dependent frequency shift observable in the transmission amplitude $|S_{21}|$. By adjusting the probe power, the system transitions from a low-power regime—where the dressed resonator frequency is apparent—to regimes dominated by bifurcation effects and finally to one where the bare resonator frequency is recovered as shown in Fig. (6.2), thereby confirming the dispersive coupling between the qubit and the resonator.

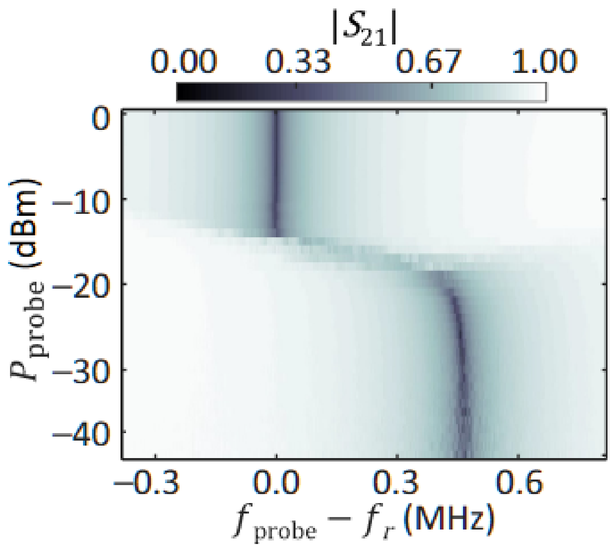

Figure 6.2: Transmission amplitude $|S_{21}|$ of the readout resonator plotted as a function of frequency and power of the probe tone. For clarity, the vertical axis has been offset by the bare readout resonator frequency $f_r = 6.876\,331$ GHz. Figure adapted from [140].

Two-tone spectroscopy is used to characterize the energy-level structure of the MET, which behaves as a weakly anharmonic oscillator. A pump tone is swept in frequency while a low-power probe tone remains fixed near the dressed resonator frequency corresponding to the qubit ground state. The experimental data shown in Fig. (6.3) reveal distinct peaks associated with single-photon and multiphoton transitions between the energy levels of the MET. From these transitions, the anharmonicity is extracted as $\alpha = 2f_{01} - f02$. Although the device was designed for a qubit frequency of 5 GHz and an anharmonicity of 260 MHz, the measured values are 4.475 GHz and 170 MHz, respectively–deviations primarily attributed to uncertainties in the a-Si tunnel barrier thickness (approximately 0.5 nm) and in the effective relative permittivity of the a-Si layer, which was determined to be around 17.5 rather than the assumed 11.9.

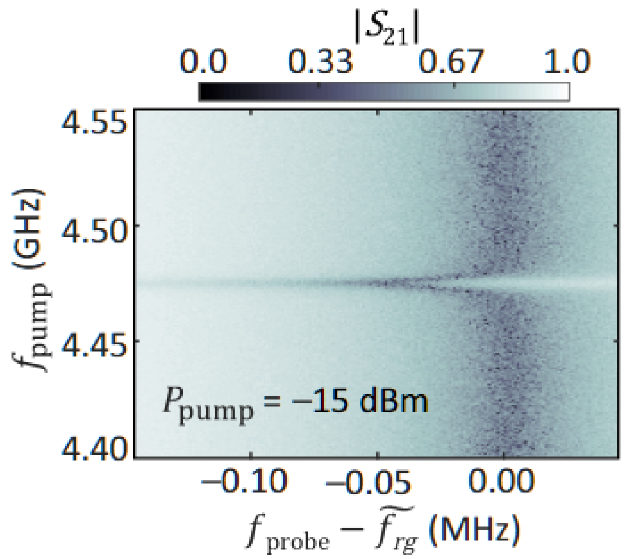

Figure 6.3: Transmission amplitude $|S_{21}|$ of the readout resonator plotted as a function of probe-tone frequency (f_{probe}) and pump-tone frequency (f_{pump}). The probe-tone power is set at -40 dBm to maintain dispersive coupling between the MET and the resonator. The change in the resonator frequency around $f_{\mathrm{pump}} \approx 4.475\,\mathrm{GHz}$ represents the MET qubit-state transition. The horizontal axis is offset by the dressed resonator frequency for the qubit ground state $\widetilde{f_{rg}} = 6.876\,796\,\mathrm{GHz}$. Figure adapted from [140].

Finite-element simulations play a critical role in understanding the electric field distribution within the MET and in quantifying the contribution of different regions to the overall device loss. In these simulations, a two-dimensional model capturing the cross-sectional geometry of the MET is constructed. The model includes the a-Si tunnel barrier, the interfaces between the barrier and the metal electrodes, and adjacent regions such as the metal–vacuum and substrate interfaces. Due to the high aspect ratio between the junction radius and the thickness of the various interface layers, a finely meshed grid is employed—particularly near the thin dielectric and interface regions to ensure accurate integration of the electric field energy.

From the simulated electric field profiles, the participation ratio (PR) for each region is computed. Defined as the fraction of the total electric field energy stored in a given region ($p_n = U_n/U_{\mathrm{total}}$), the PR provides a quantitative measure of the contribution of each region to the device's

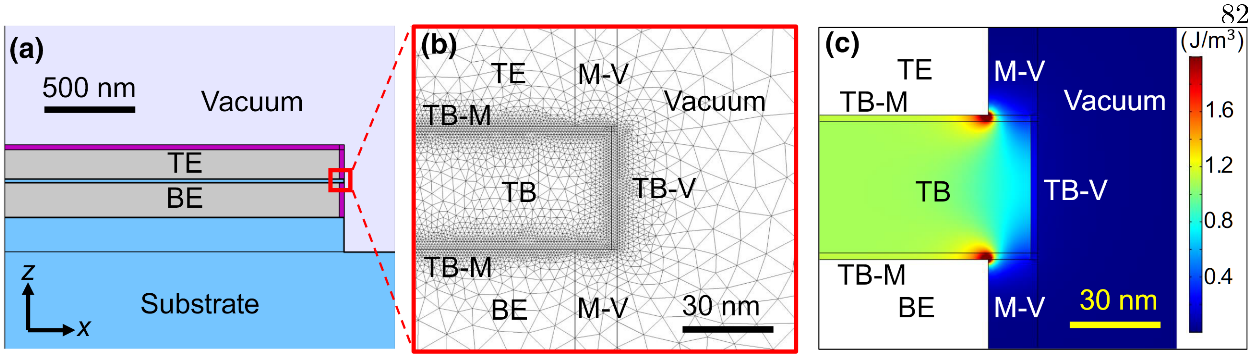

Figure 6.4: (a) Cross-section images of a MET used in the finite-element simulation. The labels attached to each region illustrate the device partition used in the TLS-loss analysis. (b),(c) Enlargement of (b) the mesh grid and (c) the electric field energy profile near the tunnel-barrier (TB) interfaces. BE, bottom electrode; M, metal; TE, top electrode; V, vacuum. Figure adapted from [140].

overall dielectric loss. By assigning literature-based loss tangents to each region, we estimate the qubit lifetime (T_1) due to dielectric losses as shown in table 6.1. The analysis reveals that the dominant loss mechanism arises from the dielectric loss in the a-Si tunnel barrier and its associated interfaces, with the PR model predicting a T_1 on the order of 17 ns.

Moreover, the simulation indicates that by replacing the amorphous silicon barrier with a high-quality crystalline material, and by optimizing the junction geometry–for example, by increasing the tunnel barrier thickness and the junction radius–the participation of lossy interfaces, particularly at the tunnel barrier–vacuum and tunnel barrier–metal boundaries, can be significantly reduced. Such modifications could potentially extend the qubit lifetime to tens or even over a hundred microseconds as shown in Fig. (6.5) while still maintaining a substantially reduced device footprint relative to conventional transmons.

These finite-element simulations and participation-ratio analyses clearly demonstrate that the amorphous silicon tunnel barrier, along with its associated interfaces, is a major contributor to dielectric loss, ultimately limiting the qubit lifetime. The predicted T_1 of approximately 17 ns underscores the need for improved material quality in the tunnel barrier region. These findings suggest that replacing the lossy amorphous silicon with a high-quality crystalline silicon barrier could substantially reduce dielectric losses. In the following section, we shift our focus to devices

Region	Material	ϵ	d (nm)	p_n	$\tan\delta$	Reference	T_1 (μs)
Tunnel barrier	a-Si	11.9	9	7×10^{-1}	5.00×10^{-4}	O'Connell et al. [145]	9.08×10^{-2}
Tunnel-barrier-metal interface	a-Si/Nb	11.4	2	2.94×10^{-1}	5.00×10^{-3}	$10 \tan\delta_{\mathrm{TB}}$	2.17×10^{-2}
Tunnel-barrier-vacuum interface	a-Si/SiO$_x$	4.0	2	8.03×10^{-5}	5.00×10^{-1}	$1000 \tan\delta_{\mathrm{TB}}$	7.93×10^{-1}
Metal-vacuum interface	Nb_2O_5	10.0	15	2.66×10^{-3}	2.20×10^{-4}	Kaiser et al. [146]	5.45×10^{1}
Substrate-vacuum interface	SiO$_x$	4.0	2	5.55×10^{-7}	1.70×10^{-3}	Woods et al. [147]	3.37×10^{4}
Metal-substrate interface	Nb/Si	11.4	2	5.73×10^{-7}	4.80×10^{-4}	Woods et al. [147]	1.16×10^{5}
Substrate	Si	11.9	10000	1.28×10^{-4}	2.60×10^{-7}	Woods et al. [147]	9.56×10^{5}

Table 6.1: Parameters for a-Si MET TLS-loss analysis: material, relative permittivity (ϵ), layer thickness (d), simulated participation ratio (p_n), TLS loss tangent ($\tan\delta$) from the literature, $\tan\delta$ reference, and T_1 for each MET region. To take into account the interface defects between the electrode metal and the barrier, we assume $\tan\delta_{\text{TB-M}}$ is 10 times $\tan\delta_{\mathrm{TB}}$. Similarly, considering the exposure of the tunnel-barrier–vacuum interface to harsh clean-room processes, $\tan\delta_{\text{TB-V}}$ is set to be 1000 times $\tan\delta_{\mathrm{TB}}$. The vacuum region is lossless and, therefore, is omitted in this analysis.

employing crystalline silicon as the barrier layer, exploring how this alternative material and the corresponding fabrication strategies may further enhance qubit coherence while preserving the benefits of a reduced device footprint.

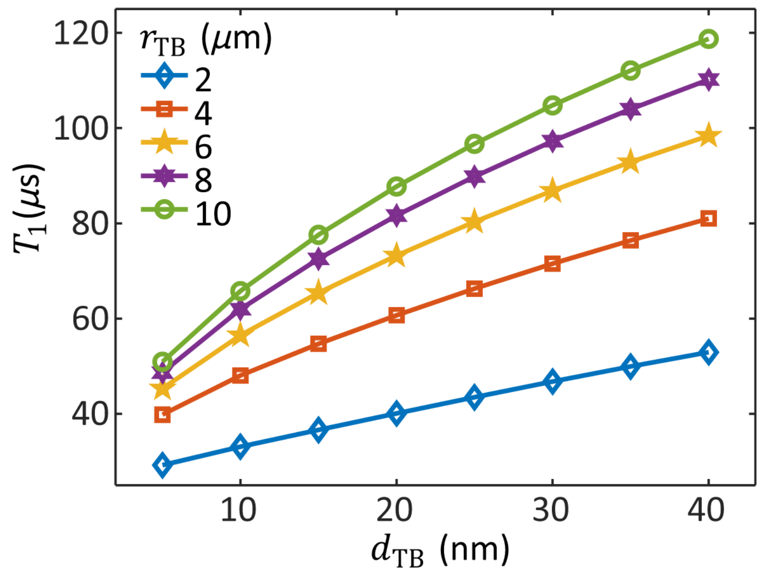

Figure 6.5: Simulated T_1 of a MET with a crystalline tunnel barrier and interfaces plotted as a function of barrier thickness d_{TB} and junction radius r_{TB}. For this analysis, we use $\tan\delta_{\mathrm{TB}}$ of 1×10^{-7}, which is comparable to $\tan\delta$ of bulk crystalline silicon [147]. The same scaling factor in table 6.1 is used to derive $\tan\delta$ of tunnel-barrier–metal ($10\tan\delta_{\mathrm{TB}}$) and tunnel barrier–vacuum ($1000\tan\delta_{\mathrm{TB}}$) interfaces. The loss tangents of all other interfaces and bulk materials are identical to the values presented in table 6.1. Figure adapted from [140].

6.3 Towards merged-element transmons using silicon fins

Motivated by the need to further scale superconducting qubit technology and to mitigate losses associated with conventional amorphous tunnel barriers, we investigate a FinMET design that leverages silicon fin technology to create merged-element transmons as shown in Fig. (6.6). This section describes the fabrication of high-aspect-ratio silicon fins, the self-aligned metallization process to form fin capacitors, and the integration of these capacitors into lumped-element resonator circuits for microwave characterization.

The FinMET devices are fabricated by Dr. Aranya Goswami and Dr. Anthony McFadden on intrinsic Si(110) substrates using an anisotropic wet etch process that exploits the crystallographic orientation to yield atomically flat Si(111) sidewalls. A silicon nitride (SiN_x) hard mask is deposited by low-pressure chemical vapor deposition and patterned via electron beam lithography followed by $\mathrm{CF_4/O_2}$ plasma etching. Prior to the wet etch, a short plasma cleaning removes the top damaged layer, ensuring uniformity in the subsequent 45% potassium hydroxide (KOH) etch at 87 °C. Fin structures with varied mask widths (ranging from 100 nm to 1 μm) are produced, with typical undercutting of 50 nm to 80 nm. The minimum reliably fabricated fin width is approximately 80 nm, with fins exhibiting lengths up to 100 μm and heights around 3 μm.

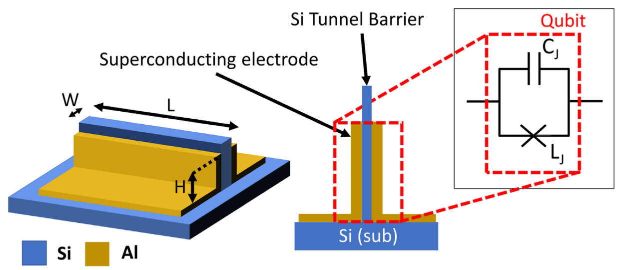

Figure 6.6: The proposed schematic of a fin merged-element transmon (FinMET). Figure adapted from [73].

Following fin formation, the fin sidewalls–composed of well-defined, smooth Si(111) surfaces–serve as the tunnel barrier. In the present work, the fins are initially fabricated too thick for tunneling; however, they are integrated as capacitive elements. Fin metallization is achieved by first cleaning the exposed Si surfaces with a buffered HF etch and a high-temperature anneal, which is critical for obtaining pristine interfaces. Superconducting aluminum (Al) is then deposited using a shadow-evaporation technique in a molecular beam epitaxy chamber. In the self-aligned process employed here, the retention of the SiN_x hard mask creates an overhang that yields a break in the metal layer at the fin top, thus naturally defining the fin capacitor without additional etching steps. Optical lithography is subsequently used to pattern the contact pads and the rest of the circuitry, enabling standard interconnectivity with the rest of the circuit.

To evaluate the electrical performance of the fin capacitors, we integrate them into lumped-element (LE) resonator circuits. These resonators are designed using a meander inductor and interdigitated capacitors (IDCs) into which the fin capacitors are incrementally added. By systematically varying the number of fins inserted between the IDC fingers, we are able to separate the resonant frequencies of the LE resonators and determine the incremental capacitance contribution

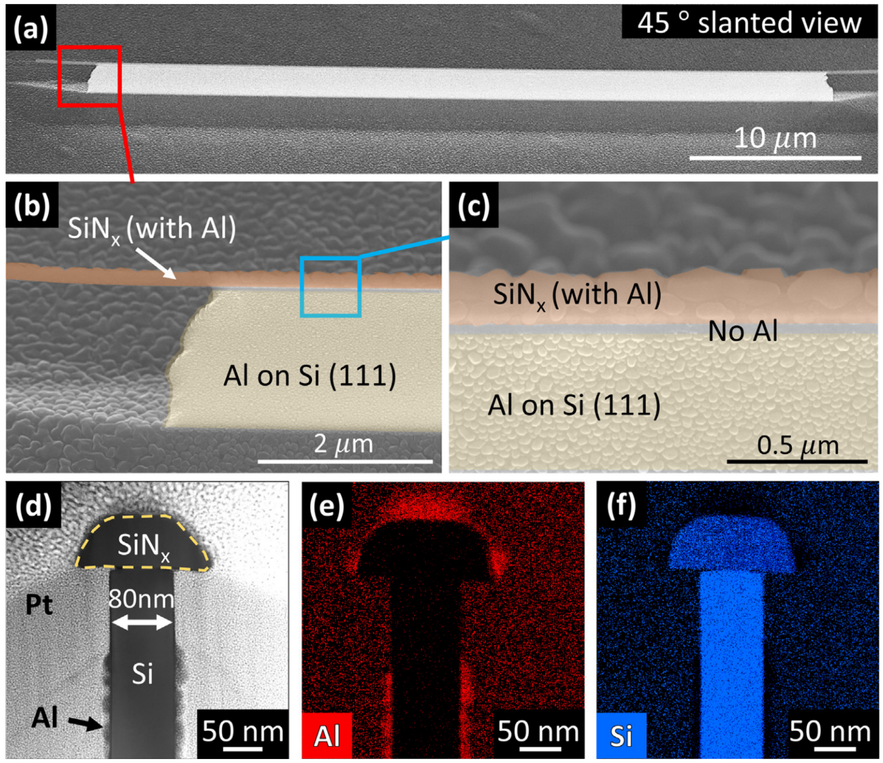

Figure 6.7: Metalized fin structure illustrating the self-aligned process and growth of Al on the Si(111) surfaces with a SiN_x hard mask. (a) Side view of the fin, (b) shows zoomed in area of (a) with the SiN_x hard mask on top of the fin, extending out to the left, and (c) shows a zoomed in area of (b) with the area where Al is shadowed.(d) High angle dark field scanning transmission electron microscopy image of a fin cross section with a SiN_x hard mask and shadow deposited Al. (e) and (f) Energy-dispersive x-ray scans highlighting the Al and Si areas, respectively. Figure adapted from [73].

of each fin. Microwave measurements are conducted on diced die packaged and cooled to 35 mK in a dilution refrigerator.

The resonant frequency of each LE resonator is found to decrease linearly with an increasing number of fins. Fig. (6.9) displays the measured resonant frequency versus the number of fins and the corresponding capacitance ratio (C_n/C_0) obtained from the resonators, where C_n is the capacitance with n fins and C_0 is the capacitance without fins. I performed finite-element simulations using COMSOL Electrostatics (Fig. (6.8)) and achieved great agreement between the simulation result and the experimental data. From these simulations, fin dimensions are extracted by fitting the measured capacitance values. For instance, nominally 400 nm and 300 nm thick fins yield ex-

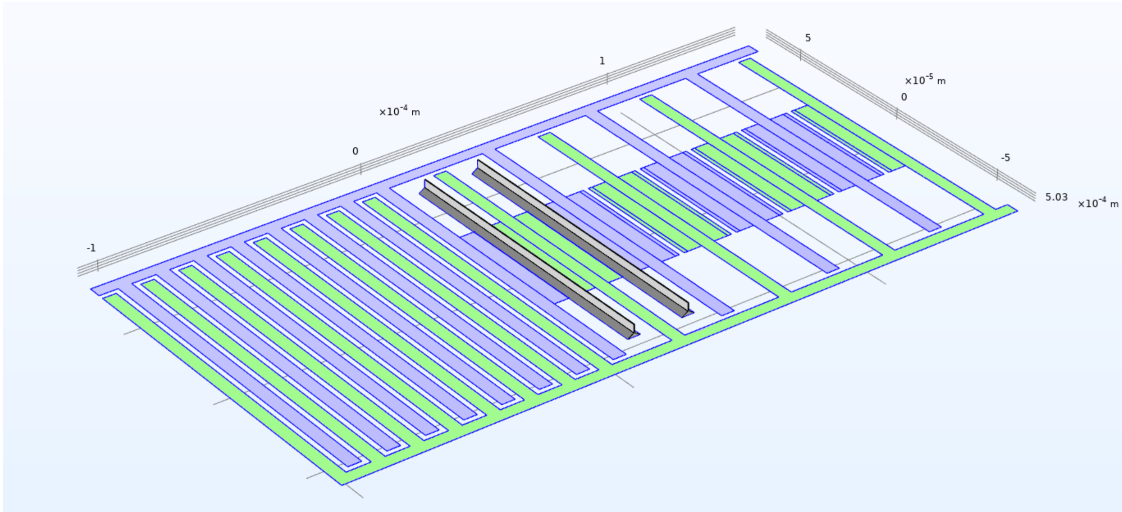

Figure 6.8: The geometry simulated with COMSOL Electrostatics to extract the capacitance of the fin parallel-plate capacitors. The IDC is formed by the two electrodes colored as blue and green respectively and is kept unchanged while adding fins (gray) to the slots.

tracted thicknesses of approximately 319 nm and 219 nm, respectively, with the capacitance per unit length determined to be $\sim 1.3\,\mathrm{fF}/\mu\mathrm{m}$ and $\sim 1.8\,\mathrm{fF}/\mu\mathrm{m}$. These values closely match estimates based on a parallel-plate capacitor model.

Additionally, the internal quality factors (Q_i) of the resonators are characterized, with one-fin and six-fin resonators exhibiting Q_i values of 8.4×10^4 and 1.8×10^5, respectively. Based on simulations of the combined IDC-fin capacitors, the single-fin loss is estimated to be on the order of 3×10^{-7}, indicating that the use of Si fins may provide a significant improvement over traditional thin-film capacitor implementations.

Future steps towards realizing FinMET devices for qubit applications are underway. To achieve tunneling through the silicon fins, the fin thickness must be reduced to approximately 5 nm to 10 nm. This extreme aspect ratio requires further refinement of the etching process, which may involve additional wet etches or digital etching methods (e.g., room-temperature O_2 plasma oxidation followed by HF etching, or atomic layer etching using a combination of O_2, HF, and $Al(CH_3)_3$). An alternative process flow using photolithography to form SiN_x masks on step edges has been proposed to enhance wafer-scale fabrication reliability [148].

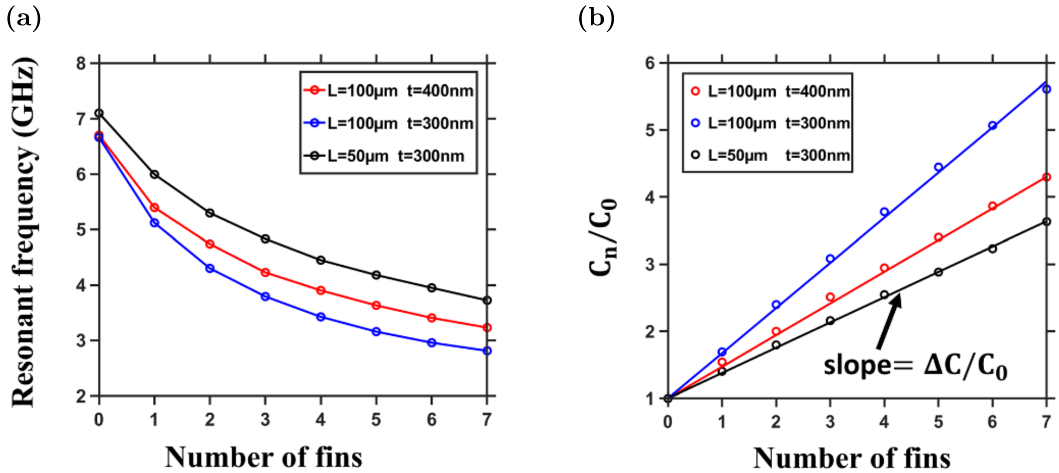

Figure 6.9: (a) Measured resonant frequency vs the number of fins in each interdigitated capacitor. (b) Capacitance ratio vs the number of fins (circles) along with fits (straight lines) from COMSOL simulations. Fits in (b) are for 219 nm and 319 nm thicknesses for nominally 300 nm and 400 nm thick fins, respectively. Figure adapted from [73].

In summary, this work demonstrates the fabrication and microwave characterization of low-loss, fin-based capacitors integrated into superconducting resonator circuits. The results establish the feasibility of using silicon fin to form self-aligned, compact superconductor/Si/superconductor trilayer structures, paving the way for the development of FinMET devices. Future efforts will focus on thinning the silicon fins into the tunneling regime, thereby enabling the realization of scalable FinMET qubits with reduced footprints and enhanced coherence.

6.4 Fabrication and Characterization of Low-Loss Al/Si/Al Parallel Plate Capacitors

Following the previous work, this section presents a detailed account of the fabrication and characterization of parallel plate capacitors constructed from aluminum-contacted, crystalline silicon fins. This work focuses on integrating these capacitors into lumped element resonators and transmon qubits to make more compact transmon capacitors that are 100 times smaller than typical planar capacitors while achieving state-of-the-art microwave performance.

The device fabrication was performed by Dr. Aranya Goswami, Dr. Anthony McFadden and Teun van Schijndel. The process begins with intrinsic Si(110) substrates, which are cleaned and then coated with a 100 nm low-stress silicon nitride (SiN_x) layer deposited via LPCVD. The SiN_x acts as a hard mask and is patterned using electron beam lithography and subsequent dry etching. Critical to the process is the alignment of the fin patterns with the major flat of the Si(110) wafer, ensuring that the etching exposes high-quality Si(111) sidewalls. The anisotropic wet etch is performed in a 45% KOH solution at 87 °C for 2 minutes, resulting in fin structures with a parallel-plate region approximately 2.2 μm tall and a tapered base that enhances mechanical stability. The fins exhibit uniform thicknesses near 220 nm in the capacitor region, which is essential for achieving the desired capacitance characteristics.

After fin formation, the native oxide is removed using a buffered oxide etch (BOE), followed by a DI water rinse, and the wafer is immediately loaded into a high-vacuum chamber for metallization. Aluminum is deposited in two 50 nm thick layers at $\pm 25°$ angles relative to the wafer normal, ensuring conformal coating of the fin sidewalls. The undercut created by the SiN_x mask naturally forms a self-aligned break in the metallization near the fin tops, thereby defining the capacitor electrodes without additional patterning steps. Post-deposition, the aluminum is patterned using optical lithography and wet etching with an acid-based etchant to define the capacitor geometry. For integration into complete circuits, Josephson junctions are fabricated using a standard EBL/Dolan bridge process, with particular care taken to calibrate junction dimensions in proximity to the fin capacitors.

The design incorporates these fin capacitors into both lumped element resonators and transmon circuits. The lumped element resonator chip comprises eight resonators inductively coupled to a central feedline in a hanger configuration. Each resonator is formed by shunting a meander inductor with a section of the fin capacitor, where approximately 81% to 84% of the total capacitance originates from the fin capacitor itself. The resonant frequency is tuned by lithographically adjusting the metalized length along the fins, and I employed 3D full-wave electromagnetic simulations to corroborate the experimental capacitance values. Finite-element analysis using COMSOL Electrostatics yields a capacitance per unit length of approximately 2.1 fF/μm, which is in reasonable agreement with a parallel plate approximation based on the measured fin dimensions.

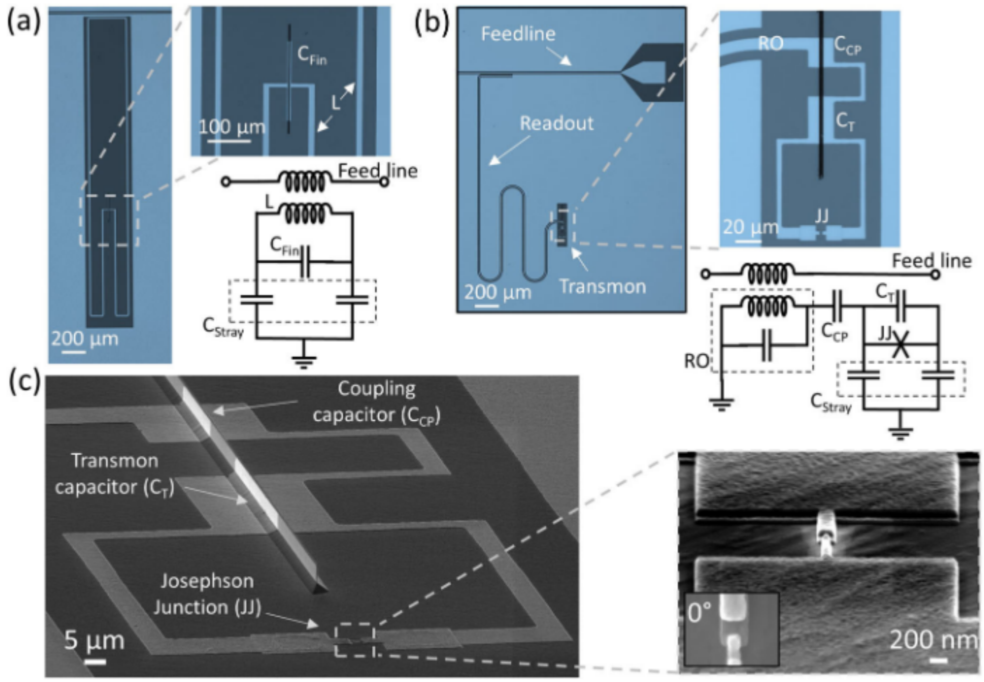

Figure 6.10: Device schematics and micrographs. (a), (b) Optical micrographs and corresponding circuit schematics for Si-fin lumped element resonators and transmons respectively. The functional components of the fin transmon are indicated and illustrate the capacitive coupling of the fin transmon to the readout resonator (RO). (c) Scanning electron micrograph of a Si-fin transmon. The insets show the Josephson junction region in higher magnification.

Microwave measurements are conducted in a dilution refrigerator at a base temperature of 35 mK. Lumped element resonators are characterized via vector network analyzer (VNA) measurements of the S_{21} transmission parameter. The resonators exhibit a low-power internal quality factor (Q_i) exceeding 700 k, with the resonant frequency showing a linear dependence on the metallized length of the fin capacitor. In addition, transmon qubits incorporating these Si-fin capacitors are evaluated. The transmon devices, fabricated on a separate chip, demonstrate anharmonicities near 300 MHz and qubit-readout coupling constants on the order of 100 MHz. Time-domain measurements yield qubit T_1 times in the range of 11 μs to 26 μs and quality factors between 350 k and 750 k. Notably, the measured T_1 times are comparable to or slightly exceed the estimated Purcell limits, underscoring the low intrinsic loss of the fin capacitor design.

The successful integration of the silicon fin capacitors into both resonator and qubit archi-

(a)

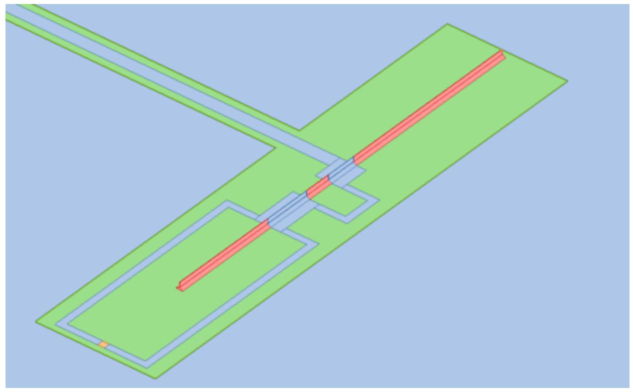

(b)

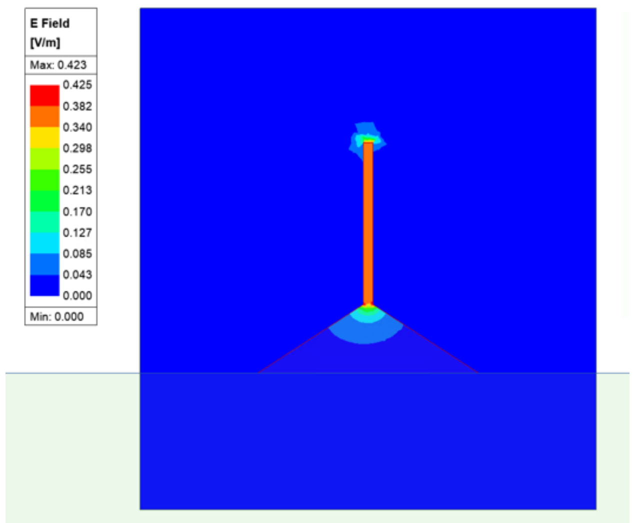

Figure 6.11: Full EM simulation of the fin transmon device. (a) Schematic of the device model simulated with Ansys HFSS. Two sections of the fin are used to form capacitors, one as the transmon shunt capacitor while the other as the coupling capacitor to the readout resonator. (b) Cross section of the fin shows that electric field is highly confined within the silicon fin. This sheds light on the potentiality of improving transmon coherence with higher quality crystallin silicon.

tectures demonstrates that the parallel plate geometry, realized through anisotropic etching and self-aligned aluminum deposition, is a promising approach for achieving compact, low-loss capacitors in superconducting quantum circuits. The fabrication process leverages standard techniques yet results in a significant reduction in footprint compared to traditional designs, while maintaining high performance. This work establishes a scalable platform that addresses the dual challenges of device miniaturization and loss mitigation, providing a strong foundation for future advancements in superconducting qubit technology.

6.5 Summary

Collectively, these three studies represent a systematic progression toward realizing the merged-element transmon with scalable, high-coherence superconducting circuits. Zhao et al. [140] explored the concept by integrating the Josephson junction and shunt capacitor into a single Nb/a-Si/Nb trilayer device, thereby dramatically reducing the qubit footprint. Building on this foundation, Goswami et al. [73] introduced the FinMET approach, exploiting silicon fin technology to form high-aspect-ratio, self-aligned fin capacitors with atomically flat Si(111) sidewalls. This innovation offers enhanced control over barrier thickness and capacitance, which are critical for improved qubit performance. Finally, McFadden et al. [59] advanced the field by demonstrating low-loss Al/Si/Al parallel plate capacitors fabricated from crystalline silicon fins. This work highlights that the careful engineering of fin-based capacitors leads to resonators and transmon qubits with quality factors and coherence times on par with or exceeding state-of-the-art devices.

Together, these works form a cohesive strategy for overcoming traditional limitations in superconducting qubit architectures. By progressively refining materials, device geometries, and fabrication processes–from amorphous to crystalline barrier materials and from planar to three-dimensional fin-based structures–this body of research lays the groundwork for next-generation quantum processors that can achieve both high integration density and enhanced coherence.

Chapter 7

Conclusion

This thesis has explored the frontiers of circuit-QED with an emphasis on pushing the experimental boundaries necessary for scalable quantum computing.

Experimentally, the work has been structured around three major thrusts. First, we demonstrated the feasibility of implementing a universal gate set with strongly ZZ coupled transmons, using both unconditional single-qubit rotations and numerically derived two-qubit operations. This result highlights the potential to precisely control qubit interactions even in the presence of strong parasitic couplings. Second, the investigation into dual-rail logical qubit encoding via parametrically coupled transmons offers a promising route toward hardware-efficient quantum error correction. Our results indicate that mid-circuit detection of erasure-type error events can serve as a tool to further prolong coherence times. Finally, by introducing the concept of the merged-element transmon–wherein the Josephson junction and shunt capacitor are integrated into a single trilayer device–we have shown a pathway to reduce the qubit footprint, a vital step toward next-generation quantum processors. Taken together, these studies not only reinforce the viability of superconducting circuits as a platform for quantum computing but also provide critical insights into the interplay between device design, coherence, and control.

Looking forward, several avenues for further research emerge. First, realizing and understanding two-qubit operations between two dual-rail logical qubits remain paramount for bringing the platform closer towards scaling and applications. Second, the scalability of superconducting qubit devices will benefit from further innovations in creating tunneling silicon fin structures, that is several orders of magnitude smaller than state of the art conventional transmons.

In conclusion, the work presented in this thesis contributes to the growing body of knowledge required to transition quantum computing from a laboratory curiosity to a practical technology. By addressing both theoretical and experimental challenges, we have taken meaningful steps toward the realization of large-scale, fault-tolerant quantum processors.

References

[1] J. Bardeen. "The Transistor, A Semi-Conductor Triode". In: **Physical Review** 74.2 (1948), pp. 230–231. DOI: 10.1103/PhysRev.74.230 (Cited on page 1).

[2] Gordon E. Moore. "Cramming More Components onto Integrated Circuits, Reprinted from Electronics, Volume 38, Number 8, April 19, 1965, Pp.114 Ff." In: **IEEE Solid-State Circuits Society Newsletter** 11.3 (Sept. 2006), pp. 33–35. ISSN: 1098-4232. DOI: 10.1109/N-SSC.2006.4785860 (Cited on page 1).

[3] James D. Meindl, Qiang Chen, and Jeffrey A. Davis. "Limits on Silicon Nanoelectronics for Terascale Integration". In: **Science** 293.5537 (Sept. 2001), pp. 2044–2049. DOI: 10.1126/science.293.5537.2044 (Cited on page 1).

[4] Supriyo Datta. **Quantum Transport: Atom to Transistor**. Cambridge University Press, June 2005. ISBN: 978-0-521-63145-7 (Cited on page 1).

[5] Mark Bohr. "A 30 Year Retrospective on Dennard's MOSFET Scaling Paper". In: **IEEE Solid-State Circuits Society Newsletter** 12.1 (2007), pp. 11–13. ISSN: 1098-4232. DOI: 10.1109/N-SSC.2007.4785534 (Cited on page 1).

[6] M. Mitchell Waldrop. "The Chips Are down for Moore's Law". In: **Nature News** 530.7589 (Feb. 2016), p. 144. DOI: 10.1038/530144a (Cited on page 1).

[7] Michael A. Nielsen and Isaac L. Chuang. **Quantum Computation and Quantum Information: 10th Anniversary Edition**. Cambridge University Press, Dec. 2010. ISBN: 978-1-139-49548-6 (Cited on page 2).

[8] Albert Abraham Michelson. **Light Waves and Their Uses**. Chicago : The University of Chicago Press, 1903 (Cited on page 2).

[9] Paul Ehrenfest. “Welche Züge Der Lichtquantenhypothese Spielen in Der Theorie Der Wärmestrahlung Eine Wesentliche Rolle?” In: **Annalen der Physik** 341.11 (1911), pp. 91–118. ISSN: 1521-3889. DOI: 10.1002/andp.19113411106 (Cited on page 2).

[10] Max Planck. “Ueber Das Gesetz Der Energieverteilung Im Normalspectrum”. In: **Annalen der Physik** 309.3 (1901), pp. 553–563. ISSN: 1521-3889. DOI: 10.1002/andp.19013090310 (Cited on page 2).

[11] Max Planck. “Ueber Irreversible Strahlungsvorgänge”. In: **Annalen der Physik** 311.12 (Jan. 1901), pp. 818–831. ISSN: 0003-3804, 1521-3889. DOI: 10.1002/andp.19013111210 (Cited on page 2).

[12] W. Heisenberg. “Über quantentheoretische Umdeutung kinematischer und mechanischer Beziehungen.” In: **Zeitschrift für Physik** 33.1 (Dec. 1925), pp. 879–893. ISSN: 0044-3328. DOI: 10.1007/BF01328377 (Cited on page 2).

[13] E. Schrödinger. “An Undulatory Theory of the Mechanics of Atoms and Molecules”. In: **Physical Review** 28.6 (1926), pp. 1049–1070. DOI: 10.1103/PhysRev.28.1049 (Cited on page 2).

[14] Anton Zeilinger. “A Foundational Principle for Quantum Mechanics”. In: **Foundations of Physics** 29.4 (Apr. 1999), pp. 631–643. ISSN: 1572-9516. DOI: 10.1023/A:1018820410908 (Cited on page 2).

[15] J. S. Bell. “On the Einstein Podolsky Rosen Paradox”. In: **Physics Physique Fizika** 1.3 (Nov. 1964), pp. 195–200. DOI: 10.1103/PhysicsPhysiqueFizika.1.195 (Cited on page 2).

[16] Alain Aspect, Philippe Grangier, and Gérard Roger. “Experimental Realization of Einstein-Podolsky-Rosen-Bohm Gedankenexperiment: A New Violation of Bell’s Inequalities”. In:

Physical Review Letters 49.2 (July 1982), pp. 91–94. doi: 10.1103/PhysRevLett.49.91 (Cited on page 2).

[17] Richard P. Feynman. “Simulating Physics with Computers”. In: **International Journal of Theoretical Physics** 21.6 (June 1982), pp. 467–488. issn: 1572-9575. doi: 10.1007/BF02650179 (Cited on page 2).

[18] P.W. Shor. “Algorithms for Quantum Computation: Discrete Logarithms and Factoring”. In: **Proceedings 35th Annual Symposium on Foundations of Computer Science**. Nov. 1994, pp. 124–134. doi: 10.1109/SFCS.1994.365700 (Cited on page 2).

[19] R. L. Rivest, A. Shamir, and L. Adleman. “A Method for Obtaining Digital Signatures and Public-Key Cryptosystems”. In: **Commun. ACM** 21.2 (Feb. 1978), pp. 120–126. issn: 0001-0782. doi: 10.1145/359340.359342 (Cited on page 2).

[20] T. D. Ladd et al. “Quantum Computers”. In: **Nature** 464.7285 (Mar. 2010), pp. 45–53. issn: 1476-4687. doi: 10.1038/nature08812 (Cited on page 2).

[21] D.j. Wineland et al. “Experimental Primer on the Trapped Ion Quantum Computer”. In: **Fortschritte der Physik** 46.4-5 (1998), pp. 363–390. issn: 1521-3978. doi: 10.1002/(SICI)1521-3978(199806)46:4/5<363::AID-PROP363>3.0.CO;2-4 (Cited on page 2).

[22] Rainer Blatt and David Wineland. “Entangled States of Trapped Atomic Ions”. In: **Nature** 453.7198 (June 2008), pp. 1008–1015. issn: 1476-4687. doi: 10.1038/nature07125 (Cited on page 3).

[23] Jeremy L. O’Brien. “Optical Quantum Computing”. In: **Science** 318.5856 (Dec. 2007), pp. 1567–1570. doi: 10.1126/science.1142892 (Cited on page 3).

[24] E. Knill, R. Laflamme, and G. J. Milburn. “A Scheme for Efficient Quantum Computation with Linear Optics”. In: **Nature** 409.6816 (Jan. 2001), pp. 46–52. issn: 1476-4687. doi: 10.1038/35051009 (Cited on page 3).

[25] Daniel Loss and David P. DiVincenzo. "Quantum Computation with Quantum Dots". In: **Physical Review A** 57.1 (Jan. 1998), pp. 120–126. DOI: 10.1103/PhysRevA.57.120 (Cited on page 3).

[26] David D. Awschalom et al. "Quantum Spintronics: Engineering and Manipulating Atom-Like Spins in Semiconductors". In: **Science** 339.6124 (Mar. 2013), pp. 1174–1179. DOI: 10.1126/science.1231364 (Cited on page 3).

[27] John Clarke and Frank K. Wilhelm. "Superconducting Quantum Bits". In: **Nature** 453.7198 (June 2008), pp. 1031–1042. ISSN: 1476-4687. DOI: 10.1038/nature07128 (Cited on page 3).

[28] Jens Koch et al. "Charge-Insensitive Qubit Design Derived from the Cooper Pair Box". In: **Physical Review A** 76.4 (Oct. 2007), p. 042319. DOI: 10.1103/PhysRevA.76.042319 (Cited on pages 3, 6, 26–30, 32, 47, 77).

[29] Morten Kjaergaard et al. "Superconducting Qubits: Current State of Play". In: **Annual Review of Condensed Matter Physics** 11.Volume 11, 2020 (Mar. 2020), pp. 369–395. ISSN: 1947-5454, 1947-5462. DOI: 10.1146/annurev-conmatphys-031119-050605 (Cited on pages 3, 27, 45).

[30] John Preskill. "Quantum Computing in the NISQ Era and Beyond". In: **Quantum** 2 (Aug. 2018), p. 79. DOI: 10.22331/q-2018-08-06-79 (Cited on pages 3, 62).

[31] Frank Arute et al. "Quantum Supremacy Using a Programmable Superconducting Processor". In: **Nature** 574.7779 (Oct. 2019), pp. 505–510. ISSN: 1476-4687. DOI: 10.1038/s41586-019-1666-5 (Cited on pages 3, 45, 77).

[32] Jacob Biamonte et al. "Quantum Machine Learning". In: **Nature** 549.7671 (Sept. 2017), pp. 195–202. ISSN: 1476-4687. DOI: 10.1038/nature23474 (Cited on page 3).

[33] Alberto Peruzzo et al. "A Variational Eigenvalue Solver on a Photonic Quantum Processor". In: **Nature Communications** 5.1 (July 2014), p. 4213. ISSN: 2041-1723. DOI: 10.1038/ncomms5213 (Cited on page 3).

[34] Edward Farhi, Jeffrey Goldstone, and Sam Gutmann. **A Quantum Approximate Optimization Algorithm Applied to a Bounded Occurrence Constraint Problem**. June 2015. DOI: 10.48550/arXiv.1412.6062. arXiv: 1412.6062 (Cited on page 3).

[35] David P. DiVincenzo. "The Physical Implementation of Quantum Computation". In: **Fortschritte der Physik** 48.9-11 (2000), pp. 771–783. ISSN: 1521-3978. DOI: 10.1002/1521-3978(200009)48:9/11<771::AID-PROP771>3.0.CO;2-E (Cited on page 4).

[36] Peter W. Shor. "Scheme for Reducing Decoherence in Quantum Computer Memory". In: **Physical Review A** 52.4 (Oct. 1995), R2493–R2496. DOI: 10.1103/PhysRevA.52.R2493 (Cited on page 4).

[37] A. M. Steane. "Error Correcting Codes in Quantum Theory". In: **Physical Review Letters** 77.5 (July 1996), pp. 793–797. DOI: 10.1103/PhysRevLett.77.793 (Cited on page 4).

[38] Barbara M. Terhal. "Quantum Error Correction for Quantum Memories". In: **Reviews of Modern Physics** 87.2 (Apr. 2015), pp. 307–346. DOI: 10.1103/RevModPhys.87.307 (Cited on pages 4, 62).

[39] M. H. Devoret and R. J. Schoelkopf. "Superconducting Circuits for Quantum Information: An Outlook". In: **Science** 339.6124 (Mar. 2013), pp. 1169–1174. DOI: 10.1126/science.1231930 (Cited on pages 4, 6, 45).

[40] A. Wallraff et al. "Strong Coupling of a Single Photon to a Superconducting Qubit Using Circuit Quantum Electrodynamics". In: **Nature** 431.7005 (Sept. 2004), pp. 162–167. ISSN: 1476-4687. DOI: 10.1038/nature02851 (Cited on page 6).

[41] Alexandre Blais et al. "Cavity Quantum Electrodynamics for Superconducting Electrical Circuits: An Architecture for Quantum Computation". In: **Physical Review A** 69.6 (June 2004), p. 062320. DOI: 10.1103/PhysRevA.69.062320 (Cited on pages 6, 32).

[42] Serge Haroche and Jean-Michel Raimond. **Exploring the Quantum: Atoms, Cavities, and Photons**. OUP Oxford, Apr. 2013. ISBN: 978-0-19-968031-3 (Cited on pages 6, 12).

[43] Y. Nakamura, Yu A. Pashkin, and J. S. Tsai. "Coherent Control of Macroscopic Quantum States in a Single-Cooper-pair Box". In: **Nature** 398.6730 (Apr. 1999), pp. 786–788. ISSN: 1476-4687. DOI: 10.1038/19718 (Cited on pages 6, 27, 29).

[44] V. Bouchiat et al. "Quantum Coherence with a Single Cooper Pair". In: **Physica Scripta** 1998.T76 (Jan. 1998), p. 165. ISSN: 1402-4896. DOI: 10.1238/Physica.Topical.076a00165 (Cited on pages 6, 27).

[45] A. A. Houck et al. "Controlling the Spontaneous Emission of a Superconducting Transmon Qubit". In: **Physical Review Letters** 101.8 (Aug. 2008), p. 080502. DOI: 10.1103/PhysRevLett.101.080502 (Cited on page 6).

[46] Matthew Reagor et al. "Quantum Memory with Millisecond Coherence in Circuit QED". In: **Physical Review B** 94.1 (July 2016), p. 014506. DOI: 10.1103/PhysRevB.94.014506 (Cited on page 7).

[47] A. Grimm et al. "Stabilization and Operation of a Kerr-cat Qubit". In: **Nature** 584.7820 (Aug. 2020), pp. 205–209. ISSN: 1476-4687. DOI: 10.1038/s41586-020-2587-z (Cited on pages 7, 62).

[48] R. K. Naik et al. "Random Access Quantum Information Processors Using Multimode Circuit Quantum Electrodynamics". In: **Nature Communications** 8.1 (Dec. 2017), p. 1904. ISSN: 2041-1723. DOI: 10.1038/s41467-017-02046-6 (Cited on page 7).

[49] M. D. Reed et al. "High-Fidelity Readout in Circuit Quantum Electrodynamics Using the Jaynes-Cummings Nonlinearity". In: **Physical Review Letters** 105.17 (Oct. 2010), p. 173601. DOI: 10.1103/PhysRevLett.105.173601 (Cited on page 7).

[50] Evan Jeffrey et al. "Fast Accurate State Measurement with Superconducting Qubits". In: **Physical Review Letters** 112.19 (May 2014), p. 190504. DOI: 10.1103/PhysRevLett.112.190504 (Cited on page 7).

[51] M. D. Reed et al. “Fast Reset and Suppressing Spontaneous Emission of a Superconducting Qubit”. In: **Applied Physics Letters** 96.20 (May 2010), p. 203110. ISSN: 0003-6951. DOI: 10.1063/1.3435463 (Cited on page 7).

[52] Nicholas T. Bronn et al. “Broadband Filters for Abatement of Spontaneous Emission in Circuit Quantum Electrodynamics”. In: **Applied Physics Letters** 107.17 (Oct. 2015), p. 172601. ISSN: 0003-6951. DOI: 10.1063/1.4934867 (Cited on page 7).

[53] Chad Rigetti and Michel Devoret. “Fully Microwave-Tunable Universal Gates in Superconducting Qubits with Linear Couplings and Fixed Transition Frequencies”. In: **Physical Review B** 81.13 (Apr. 2010), p. 134507. DOI: 10.1103/PhysRevB.81.134507 (Cited on page 7).

[54] Jerry M. Chow et al. “Simple All-Microwave Entangling Gate for Fixed-Frequency Superconducting Qubits”. In: **Physical Review Letters** 107.8 (Aug. 2011), p. 080502. DOI: 10.1103/PhysRevLett.107.080502 (Cited on page 7).

[55] Alexandre Blais et al. “Circuit Quantum Electrodynamics”. In: **Reviews of Modern Physics** 93.2 (May 2021), p. 025005. DOI: 10.1103/RevModPhys.93.025005 (Cited on pages 7, 32).

[56] Michel H. Devoret. “Quantum Fluctuations in Electrical Circuits.” In: **Fluctuations Quantiques: Les Houches, Session LXIII, 27 Juin-28 Juillet 1995 = Quantum Fluctuations**. Amsterdam: Elsevier, 1997, pp. 351–386. ISBN: 978-0-444-82593-3 (Cited on pages 8, 24).

[57] Steven M. Girvin. **Circuit QED: Superconducting Qubits Coupled to Microwave Photons**. Oxford University Press, June 2014. ISBN: 978-0-19-968118-1. DOI: 10.1093/acprof:oso/9780199681181.003.0003 (Cited on pages 8, 22, 24).

[58] Leon N. Cooper. “Bound Electron Pairs in a Degenerate Fermi Gas”. In: **Physical Review** 104.4 (Nov. 1956), pp. 1189–1190. DOI: 10.1103/PhysRev.104.1189 (Cited on page 10).

[59] Anthony P. McFadden et al. "Fabrication and Characterization of Low-Loss Al/Si/Al Parallel Plate Capacitors for Superconducting Quantum Information Applications". In: **npj Quantum Information** 11.1 (Jan. 2025), pp. 1–6. ISSN: 2056-6387. DOI: 10.1038/s41534-025-00967-5 (Cited on pages 12, 23, 77, 92).

[60] D. F. Walls and G. J. Milburn. **Quantum Optics**. Springer Berlin Heidelberg, July 2012. ISBN: 978-3-642-79505-3 (Cited on page 12).

[61] Wayne M. Itano et al. "Quantum Harmonic Oscillator State Synthesis and Analysis". In: **Photonics West '97**. Ed. by Mara Goff Prentiss and William D. Phillips. San Jose, CA, May 1997, pp. 43–55. DOI: 10.1117/12.273771 (Cited on page 13).

[62] N. N. Bogoljubov. "On a New Method in the Theory of Superconductivity". In: **Il Nuovo Cimento (1955-1965)** 7.6 (Mar. 1958), pp. 794–805. ISSN: 1827-6121. DOI: 10.1007/BF02745585 (Cited on page 15).

[63] David M. Pozar. **Microwave Engineering**. Wiley, 2012. ISBN: 978-0-470-63155-3 (Cited on page 16).

[64] C. W. Gardiner and M. J. Collett. "Input and Output in Damped Quantum Systems: Quantum Stochastic Differential Equations and the Master Equation". In: **Physical Review A** 31.6 (June 1985), pp. 3761–3774. DOI: 10.1103/PhysRevA.31.3761 (Cited on pages 20, 22).

[65] B. Yurke. "Input-Output Theory". In: **Quantum Squeezing**. Ed. by Peter D. Drummond and Zbigniew Ficek. Berlin, Heidelberg: Springer, 2004, pp. 53–96. ISBN: 978-3-662-09645-1. DOI: 10.1007/978-3-662-09645-1_3 (Cited on page 20).

[66] G. W. Ford, J. T. Lewis, and R. F. O'Connell. "Quantum Langevin Equation". In: **Physical Review A** 37.11 (June 1988), pp. 4419–4428. DOI: 10.1103/PhysRevA.37.4419 (Cited on page 20).

[67] L. Frunzio et al. "Fabrication and Characterization of Superconducting Circuit QED Devices for Quantum Computation". In: **IEEE Transactions on Applied Superconductivity**

15.2 (June 2005), pp. 860–863. ISSN: 1558-2515. DOI: 10.1109/TASC.2005.850084 (Cited on page 23).

[68] Alexander P. Read et al. “Precision Measurement of the Microwave Dielectric Loss of Sapphire in the Quantum Regime with Parts-per-Billion Sensitivity”. In: **Physical Review Applied** 19.3 (Mar. 2023), p. 034064. DOI: 10.1103/PhysRevApplied.19.034064 (Cited on page 23).

[69] C. Wang et al. “Surface Participation and Dielectric Loss in Superconducting Qubits”. In: **Applied Physics Letters** 107.16 (Oct. 2015), p. 162601. ISSN: 0003-6951. DOI: 10.1063/1.4934486 (Cited on page 23).

[70] Matthew James Reagor. “Superconducting Cavities for Circuit Quantum Electrodynamics”. PhD thesis. ProQuest Dissertations Publishing, 2016. ISBN: 9781369157697 (Cited on page 23).

[71] Andrew E. Oriani et al. **Niobium Coaxial Cavities with Internal Quality Factors Exceeding 1.5 Billion for Circuit Quantum Electrodynamics**. Mar. 2024. DOI: 10.48550/arXiv.2403.00286. arXiv: 2403.00286 [quant-ph] (Cited on page 23).

[72] Kevin D. Crowley et al. “Disentangling Losses in Tantalum Superconducting Circuits”. In: **Physical Review X** 13.4 (Oct. 2023), p. 041005. DOI: 10.1103/PhysRevX.13.041005 (Cited on page 23).

[73] Aranya Goswami et al. “Towards Merged-Element Transmons Using Silicon Fins: The FinMET”. In: **Applied Physics Letters** 121.6 (Aug. 2022), p. 064001. ISSN: 0003-6951. DOI: 10.1063/5.0104950 (Cited on pages 23, 77, 85, 86, 88, 92).

[74] M.P. Weides. “Barriers in Josephson Junctions: An Overview”. In: **The Oxford Handbook of Small Superconductors**. Ed. by A.V. Narlikar. Oxford University Press, Jan. 2017, pp. 432–458. ISBN: 978-0-19-873816-9. DOI: 10.1093/oxfordhb/9780198738169.013.15 (Cited on page 24).

[75] Antonio Barone and Gianfranco Paterno. **Physics and Applications of the Josephson Effect**. Wiley, May 1982. ISBN: 978-0-471-01469-0 (Cited on page 25).

[76] S.E. Rasmussen et al. "Superconducting Circuit Companion—an Introduction with Worked Examples". In: **PRX Quantum** 2.4 (Dec. 2021), p. 040204. DOI: 10.1103/PRXQuantum.2.040204 (Cited on pages 27, 35).

[77] Alexander Shnirman, Gerd Schön, and Ziv Hermon. "Quantum Manipulations of Small Josephson Junctions". In: **Physical Review Letters** 79.12 (Sept. 1997), pp. 2371–2374. DOI: 10.1103/PhysRevLett.79.2371 (Cited on page 27).

[78] E.T. Jaynes and F.W. Cummings. "Comparison of Quantum and Semiclassical Radiation Theories with Application to the Beam Maser". In: **Proceedings of the IEEE** 51.1 (Jan. 1963), pp. 89–109. ISSN: 1558-2256. DOI: 10.1109/PROC.1963.1664 (Cited on page 31).

[79] David Isaac Schuster. "Circuit Quantum Electrodynamics". PhD thesis. United States – Connecticut: Yale University, 2007. ISBN: 9780549067177 (Cited on page 31).

[80] D. I. Schuster et al. "Ac Stark Shift and Dephasing of a Superconducting Qubit Strongly Coupled to a Cavity Field". In: **Physical Review Letters** 94.12 (Mar. 2005), p. 123602. DOI: 10.1103/PhysRevLett.94.123602 (Cited on page 33).

[81] Jay Gambetta et al. "Qubit-Photon Interactions in a Cavity: Measurement-induced Dephasing and Number Splitting". In: **Physical Review A** 74.4 (Oct. 2006), p. 042318. DOI: 10.1103/PhysRevA.74.042318 (Cited on page 33).

[82] D. I. Schuster et al. "Resolving Photon Number States in a Superconducting Circuit". In: **Nature** 445.7127 (Feb. 2007), pp. 515–518. ISSN: 1476-4687. DOI: 10.1038/nature05461 (Cited on page 33).

[83] Brian Vlastakis et al. "Deterministically Encoding Quantum Information Using 100-Photon Schrödinger Cat States". In: **Science** 342.6158 (Nov. 2013), pp. 607–610. DOI: 10.1126/science.1243289 (Cited on page 33).

[84] G. Catelani et al. “Relaxation and Frequency Shifts Induced by Quasiparticles in Superconducting Qubits”. In: **Physical Review B** 84.6 (Aug. 2011), p. 064517. DOI: 10.1103/PhysRevB.84.064517 (Cited on page 34).

[85] R. W. Simmonds et al. “Decoherence in Josephson Phase Qubits from Junction Resonators”. In: **Physical Review Letters** 93.7 (Aug. 2004), p. 077003. DOI: 10.1103/PhysRevLett.93.077003 (Cited on page 34).

[86] Seongshik Oh et al. “Elimination of Two Level Fluctuators in Superconducting Quantum Bits by an Epitaxial Tunnel Barrier”. In: **Physical Review B** 74.10 (Sept. 2006), p. 100502. DOI: 10.1103/PhysRevB.74.100502 (Cited on page 34).

[87] Clemens Müller, Jared H Cole, and Jürgen Lisenfeld. “Towards Understanding Two-Level-Systems in Amorphous Solids: Insights from Quantum Circuits”. In: **Reports on Progress in Physics** 82.12 (Oct. 2019), p. 124501. ISSN: 0034-4885. DOI: 10.1088/1361-6633/ab3a7e (Cited on pages 34, 77).

[88] Alexander P. M. Place et al. “New Material Platform for Superconducting Transmon Qubits with Coherence Times Exceeding 0.3 Milliseconds”. In: **Nature Communications** 12.1 (Mar. 2021), p. 1779. ISSN: 2041-1723. DOI: 10.1038/s41467-021-22030-5 (Cited on page 34).

[89] Chenlu Wang et al. “Towards Practical Quantum Computers: Transmon Qubit with a Lifetime Approaching 0.5 Milliseconds”. In: **npj Quantum Information** 8.1 (Jan. 2022), pp. 1–6. ISSN: 2056-6387. DOI: 10.1038/s41534-021-00510-2 (Cited on page 34).

[90] Mustafa Bal et al. “Systematic Improvements in Transmon Qubit Coherence Enabled by Niobium Surface Encapsulation”. In: **npj Quantum Information** 10.1 (Apr. 2024), pp. 1–8. ISSN: 2056-6387. DOI: 10.1038/s41534-024-00840-x (Cited on page 34).

[91] David A. Rower et al. “Evolution of $1/F$ Flux Noise in Superconducting Qubits with Weak Magnetic Fields”. In: **Physical Review Letters** 130.22 (May 2023), p. 220602. DOI: 10.1103/PhysRevLett.130.220602 (Cited on page 34).

[92] Roald K. Wangsness. “Sublattice Effects in Magnetic Resonance”. In: **Physical Review** 91.5 (Sept. 1953), pp. 1085–1091. DOI: 10.1103/PhysRev.91.1085 (Cited on page 35).

[93] F. Bloch. “Generalized Theory of Relaxation”. In: **Physical Review** 105.4 (Feb. 1957), pp. 1206–1222. DOI: 10.1103/PhysRev.105.1206 (Cited on page 35).

[94] A. G. Redfield. “The Theory of Relaxation Processes”. In: **Advances in Magnetic and Optical Resonance**. Ed. by John S. Waugh. Vol. 1. Advances in Magnetic Resonance. Academic Press, Jan. 1965, pp. 1–32. DOI: 10.1016/B978-1-4832-3114-3.50007-6 (Cited on page 35).

[95] F. Motzoi et al. “Simple Pulses for Elimination of Leakage in Weakly Nonlinear Qubits”. In: **Physical Review Letters** 103.11 (Sept. 2009), p. 110501. DOI: 10.1103/PhysRevLett.103.110501 (Cited on pages 41, 45, 61).

[96] Zijun Chen et al. “Measuring and Suppressing Quantum State Leakage in a Superconducting Qubit”. In: **Physical Review Letters** 116.2 (Jan. 2016), p. 020501. DOI: 10.1103/PhysRevLett.116.020501 (Cited on page 41).

[97] David C. McKay et al. “Efficient \$Z\$ Gates for Quantum Computing”. In: **Physical Review A** 96.2 (Aug. 2017), p. 022330. DOI: 10.1103/PhysRevA.96.022330 (Cited on page 41).

[98] Junling Long et al. **A Universal Quantum Gate Set for Transmon Qubits with Strong ZZ Interactions**. Mar. 2021. DOI: 10.48550/arXiv.2103.12305. arXiv: 2103.12305 [quant-ph] (Cited on page 44).

[99] Jay M Gambetta, Jerry M Chow, and Matthias Steffen. “Building Logical Qubits in a Superconducting Quantum Computing System”. In: **npj Quantum Information** 3.1 (2017), pp. 1–7. DOI: 10.1038/s41534-016-0004-0 (Cited on page 45).

[100] P. Krantz et al. “A Quantum Engineer’s Guide to Superconducting Qubits”. In: **Applied Physics Reviews** 6.2 (June 2019), p. 021318. DOI: 10.1063/1.5089550 (Cited on page 45).

[101] R. Barends et al. "Superconducting Quantum Circuits at the Surface Code Threshold for Fault Tolerance". In: **Nature** 508.7497 (Apr. 2014), pp. 500–503. ISSN: 1476-4687. DOI: 10.1038/nature13171 (Cited on pages 45, 62).

[102] David C McKay et al. "Three-Qubit Randomized Benchmarking". In: **Physical review letters** 122.20 (2019), p. 200502. DOI: 10.1103/PhysRevLett.122.200502 (Cited on page 45).

[103] Sabrina S Hong et al. "Demonstration of a Parametrically Activated Entangling Gate Protected from Flux Noise". In: **Physical Review A** 101.1 (2020), p. 012302. DOI: 10.1103/PhysRevA.101.012302 (Cited on page 45).

[104] Andrew W Cross et al. "Validating Quantum Computers Using Randomized Model Circuits". In: **Physical Review A** 100.3 (2019), p. 032328. DOI: 10.1103/PhysRevA.100.032328 (Cited on page 45).

[105] JS Otterbach et al. "Unsupervised Machine Learning on a Hybrid Quantum Computer". In: **arXiv preprint arXiv:1712.05771** (2017). DOI: 10.48550/arXiv.1712.05771. arXiv: 1712.05771 (Cited on page 45).

[106] Sarah Sheldon et al. "Characterizing Errors on Qubit Operations via Iterative Randomized Benchmarking". In: **Physical Review A** 93.1 (2016), p. 012301. DOI: 10.1103/PhysRevA.93.012301 (Cited on page 45).

[107] Julian Kelly et al. "Optimal Quantum Control Using Randomized Benchmarking". In: **Physical review letters** 112.24 (2014), p. 240504. DOI: 10.1103/PhysRevLett.112.240504 (Cited on page 45).

[108] Google AI Quantum et al. "Demonstrating a Continuous Set of Two-Qubit Gates for Near-Term Quantum Algorithms". In: **Physical Review Letters** 125.12 (Sept. 2020), p. 120504. DOI: 10.1103/PhysRevLett.125.120504 (Cited on page 45).

[109] Morten Kjaergaard et al. **Programming a Quantum Computer with Quantum Instructions**. Dec. 2020. DOI: 10.48550/arXiv.2001.08838. arXiv: 2001.08838 [quant-ph] (Cited on page 45).

[110] S. Krinner et al. "Demonstration of an All-Microwave Controlled-Phase Gate between Far-Detuned Qubits". In: **Physical Review Applied** 14.4 (Oct. 2020), p. 044039. DOI: 10.1103/PhysRevApplied.14.044039 (Cited on page 45).

[111] Yuan Xu et al. "High-Fidelity, High-Scalability Two-Qubit Gate Scheme for Superconducting Qubits". In: **Physical Review Letters** 125.24 (Dec. 2020), p. 240503. DOI: 10.1103/PhysRevLett.125.240503 (Cited on page 45).

[112] Michele C. Collodo et al. "Implementation of Conditional Phase Gates Based on Tunable ZZ Interactions". In: **Physical Review Letters** 125.24 (Dec. 2020), p. 240502. DOI: 10.1103/PhysRevLett.125.240502 (Cited on pages 45, 52).

[113] David C McKay et al. "Universal Gate for Fixed-Frequency Qubits via a Tunable Bus". In: **Physical Review Applied** 6.6 (2016), p. 064007. DOI: 10.1103/PhysRevApplied.6.064007 (Cited on pages 45, 59).

[114] Pranav Mundada et al. "Suppression of Qubit Crosstalk in a Tunable Coupling Superconducting Circuit". In: **Physical Review Applied** 12.5 (2019), p. 054023. DOI: 10.1103/PhysRevApplied.12.054023 (Cited on page 45).

[115] X. Li et al. "Tunable Coupler for Realizing a Controlled-Phase Gate with Dynamically Decoupled Regime in a Superconducting Circuit". In: **Physical Review Applied** 14.2 (Aug. 2020), p. 024070. DOI: 10.1103/PhysRevApplied.14.024070 (Cited on page 45).

[116] Jaseung Ku et al. "Suppression of Unwanted ZZ Interactions in a Hybrid Two-Qubit System". In: **Physical Review Letters** 125.20 (Nov. 2020), p. 200504. DOI: 10.1103/PhysRevLett.125.200504 (Cited on page 45).

[117] Sophia E. Economou and Edwin Barnes. “Analytical Approach to Swift Nonleaky Entangling Gates in Superconducting Qubits”. In: **Physical Review B** 91.16 (Apr. 2015), p. 161405. DOI: 10.1103/PhysRevB.91.161405 (Cited on pages 45, 46, 52–54).

[118] Xiu-Hao Deng, Edwin Barnes, and Sophia E. Economou. “Robustness of Error-Suppressing Entangling Gates in Cavity-Coupled Transmon Qubits”. In: **Physical Review B** 96.3 (July 2017), p. 035441. DOI: 10.1103/PhysRevB.96.035441 (Cited on pages 45, 46, 52).

[119] George S. Barron et al. “Microwave-Based Arbitrary Cphase Gates for Transmon Qubits”. In: **Physical Review B** 101.5 (Feb. 2020), p. 054508. DOI: 10.1103/PhysRevB.101.054508 (Cited on pages 46, 52).

[120] X. Wu et al. “Overlap Junctions for High Coherence Superconducting Qubits”. In: **Applied Physics Letters** 111.3 (2017), p. 032602. DOI: 10.1063/1.4993937 (Cited on page 47).

[121] Junling Long. “Superconducting Quantum Circuits for Quantum Information Processing”. PhD thesis. University of Colorado Boulder, 2021. ISBN: 9798664763133 (Cited on pages 47, 48).

[122] Edwin Barnes and S Das Sarma. “Analytically Solvable Driven Time-Dependent Two-Level Quantum Systems”. In: **Physical review letters** 109.6 (2012), p. 060401. DOI: 10.1103/PhysRevLett.109.060401 (Cited on page 52).

[123] Shavindra P. Premaratne et al. “Implementation of a Generalized Controlled-NOT Gate between Fixed-Frequency Transmons”. In: **Physical Review A: Atomic, Molecular, and Optical Physics** 99.1 (Jan. 2019), p. 012317. DOI: 10.1103/PhysRevA.99.012317 (Cited on page 52).

[124] E. Knill et al. “Randomized Benchmarking of Quantum Gates”. In: **Physical Review A** 77.1 (Jan. 2008), p. 012307. DOI: 10.1103/PhysRevA.77.012307 (Cited on page 55).

[125] Jeremy L O'Brien et al. "Quantum Process Tomography of a Controlled-NOT Gate". In: **Physical review letters** 93.8 (2004), p. 080502. DOI: 10.1103/PhysRevLett.93.080502 (Cited on page 58).

[126] A Dewes et al. "Characterization of a Two-Transmon Processor with Individual Single-Shot Qubit Readout". In: **Physical review letters** 108.5 (2012), p. 057002. DOI: 10.1103/PhysRevLett.108.057002 (Cited on page 59).

[127] Phillip Kaye, Raymond Laflamme, and Michele Mosca. **An Introduction to Quantum Computing**. OUP Oxford, Nov. 2006. ISBN: 978-0-19-152461-5 (Cited on page 59).

[128] C. J. Ballance et al. "High-Fidelity Quantum Logic Gates Using Trapped-Ion Hyperfine Qubits". In: **Physical Review Letters** 117.6 (Aug. 2016), p. 060504. DOI: 10.1103/PhysRevLett.117.060504 (Cited on page 62).

[129] Juan Zurita et al. "Multipartite Entanglement Distribution in a Topological Photonic Network". In: **Quantum** 9 (Feb. 2025), p. 1625. DOI: 10.22331/q-2025-02-10-1625 (Cited on page 62).

[130] Xiao Xue et al. "Quantum Logic with Spin Qubits Crossing the Surface Code Threshold". In: **Nature** 601.7893 (Jan. 2022), pp. 343–347. ISSN: 1476-4687. DOI: 10.1038/s41586-021-04273-w (Cited on page 62).

[131] Victor V. Albert et al. "Performance and Structure of Single-Mode Bosonic Codes". In: **Physical Review A** 97.3 (Mar. 2018), p. 032346. DOI: 10.1103/PhysRevA.97.032346 (Cited on page 62).

[132] Aleksander Kubica et al. "Erasure Qubits: Overcoming the ${T}_{1}$ Limit in Superconducting Circuits". In: **Physical Review X** 13.4 (Nov. 2023), p. 041022. DOI: 10.1103/PhysRevX.13.041022 (Cited on pages 62, 66).

[133] James D. Teoh et al. “Dual-Rail Encoding with Superconducting Cavities”. In: **Proceedings of the National Academy of Sciences** 120.41 (Oct. 2023), e2221736120. DOI: 10.1073/pnas.2221736120 (Cited on page 62).

[134] Yue Wu et al. “Erasure Conversion for Fault-Tolerant Quantum Computing in Alkaline Earth Rydberg Atom Arrays”. In: **Nature Communications** 13.1 (Aug. 2022), p. 4657. ISSN: 2041-1723. DOI: 10.1038/s41467-022-32094-6 (Cited on page 63).

[135] Shuo Ma et al. “High-Fidelity Gates and Mid-Circuit Erasure Conversion in an Atomic Qubit”. In: **Nature** 622.7982 (Oct. 2023), pp. 279–284. ISSN: 1476-4687. DOI: 10.1038/s41586-023-06438-1 (Cited on page 63).

[136] Kevin S. Chou et al. “A Superconducting Dual-Rail Cavity Qubit with Erasure-Detected Logical Measurements”. In: **Nature Physics** 20.9 (Sept. 2024), pp. 1454–1460. ISSN: 1745-2481. DOI: 10.1038/s41567-024-02539-4 (Cited on page 63).

[137] H. Levine et al. “Demonstrating a Long-Coherence Dual-Rail Erasure Qubit Using Tunable Transmons”. In: **Physical Review X** 14.1 (Mar. 2024), p. 011051. DOI: 10.1103/PhysRevX.14.011051 (Cited on pages 63, 70).

[138] T. Noh et al. “Strong Parametric Dispersive Shifts in a Statically Decoupled Two-Qubit Cavity QED System”. In: **Nature Physics** 19.10 (Oct. 2023), pp. 1445–1451. ISSN: 1745-2481. DOI: 10.1038/s41567-023-02107-2 (Cited on page 66).

[139] Easwar Magesan, J. M. Gambetta, and Joseph Emerson. “Scalable and Robust Randomized Benchmarking of Quantum Processes”. In: **Physical Review Letters** 106.18 (May 2011), p. 180504. DOI: 10.1103/PhysRevLett.106.180504 (Cited on page 68).

[140] Ruichen Zhao et al. “Merged-Element Transmon”. In: **Physical Review Applied** 14.6 (Dec. 2020), p. 064006. DOI: 10.1103/PhysRevApplied.14.064006 (Cited on pages 77, 79–82, 84, 92).

[141] Z. K. Minev et al. “To Catch and Reverse a Quantum Jump Mid-Flight”. In: **Nature** 570.7760 (June 2019), pp. 200–204. ISSN: 1476-4687. DOI: 10.1038/s41586-019-1287-z (Cited on page 77).

[142] Patrick S. Finnegan et al. “High Aspect Ratio Anisotropic Silicon Etching for X-Ray Phase Contrast Imaging Grating Fabrication”. In: **Materials Science in Semiconductor Processing**. Material Processing of Optical Devices and Their Applications 92 (Mar. 2019), pp. 80–85. ISSN: 1369-8001. DOI: 10.1016/j.mssp.2018.06.013 (Cited on page 78).

[143] Mao-Lin Chen et al. “A FinFET with One Atomic Layer Channel”. In: **Nature Communications** 11.1 (Mar. 2020), p. 1205. ISSN: 2041-1723. DOI: 10.1038/s41467-020-15096-0 (Cited on page 78).

[144] David Olaya et al. “Amorphous Nb-Si Barrier Junctions for Voltage Standard and Digital Applications”. In: **IEEE Transactions on Applied Superconductivity** 19.3 (June 2009), pp. 144–148. ISSN: 1558-2515. DOI: 10.1109/TASC.2009.2018254 (Cited on page 79).

[145] Aaron D. O’Connell et al. “Microwave Dielectric Loss at Single Photon Energies and Millikelvin Temperatures”. In: **Applied Physics Letters** 92.11 (Mar. 2008), p. 112903. ISSN: 0003-6951. DOI: 10.1063/1.2898887 (Cited on page 83).

[146] Ch Kaiser et al. “Measurement of Dielectric Losses in Amorphous Thin Films at Gigahertz Frequencies Using Superconducting Resonators”. In: **Superconductor Science and Technology** 23.7 (June 2010), p. 075008. ISSN: 0953-2048. DOI: 10.1088/0953-2048/23/7/075008 (Cited on page 83).

[147] W. Woods et al. “Determining Interface Dielectric Losses in Superconducting Coplanar-Waveguide Resonators”. In: **Physical Review Applied** 12.1 (July 2019), p. 014012. DOI: 10.1103/PhysRevApplied.12.014012 (Cited on pages 83, 84).

[148] Vladimir Jovanovic, Tomislav Suligoj, and Lis Nanver. “Crystallographic Silicon-Etching for Ultra-High Aspect-Ratio FinFET”. In: **ECS Transactions** 13.1 (Oct. 2008), p. 313. ISSN: 1938-5862. DOI: 10.1149/1.2911512 (Cited on page 87).